
AMMONIA AS CARBON FREE FUEL FOR INTERNAL COMBUSTION ENGINE DRIVEN AGRICULTURAL VEHICLE (ACTIVATE)

Work package 3
Deliverable report D3.4

Report from the activities in WP3

SIMULATION AND OPTIMIZATION
OF AMMONIA-BASED COMBUSTION SYSTEM
FOR CI ENGINE

Michał Pasternak (LOGE), Michał T. Lewandowski (NTNU)
michal.pasternak@logesoft.com, michalew@ntnu.no

Work Package 3 Leader
Michał Pasternak

.....

Project Promoter
Wojciech Adamczyk

.....

Contents

1	Introduction	3
1.1	Background	3
1.2	Workflow	4
1.3	Report structure	5
2	Numerical tools	6
2.1	Introduction	6
2.2	0D engine modelling using SRM	6
2.3	LOGEfuel and tabulated chemistry	9
2.4	3D CFD Converge	11
3	Simulation tool chain development	13
3.1	Tools chain concept	13
3.2	Ammonia/biodiesel chemistry development	14
3.3	3D CFD for investigating ammonia injection	24
3.4	0D SRM for simulating engine performance parameters	37
4	Simulation results	49
4.1	3D CFD modelling of ammonia injection	49
4.2	Impact of ammonia share in the fuel for a given fuel injection strategy	68
4.3	Aspects of mixture formation in 0D and 3D models	79
4.4	Engine performance mapping	80
5	Summary	89

1 Introduction

1.1 Background

This report presents works conducted within the third work package (WP3) of the project. The findings that were presented in separate milestone and deliverable reports of WP3 during the project execution are here presented in one common report.

The overall objective of the work described in this report was the development of a methodology for simulating compression ignition (CI) engines fueled with biodiesel and ammonia both directly injected into the cylinder (ACTIVATE technology). Specifically the work focused on an application of three-dimensional fluid dynamics simulations (3D CFD), 0D stochastic reactor model (SRM), detailed chemistry and optimization algorithms as a software tool chain. The chain aimed at supporting the ACTIVATE technology development at various stages of the project. This includes simulations and optimization of engine performance parameters such as fuel consumption, efficiency and exhaust emission to support the experimental works with respect to fuel injection strategy with ammonia, investigating mixture formation and combustion in a CI engine retrofitted to the operation with a biodiesel and ammonia. Furthermore, we aimed at determination of simulation method and rules that would enable one the extrapolating of findings from this work for the application to other CI combustion engines, and hence to support their retrofitting to the use of ammonia, and potentially helping in reduction of costs and time of prototyping and preliminary investigations at early stage of the development.

To comply with the overall objective of the work package, 0D SRM and 3D CFD model are applied to the same engine experiment, investigating aspects of simulations of combustion and emissions formation (Fig. 1).

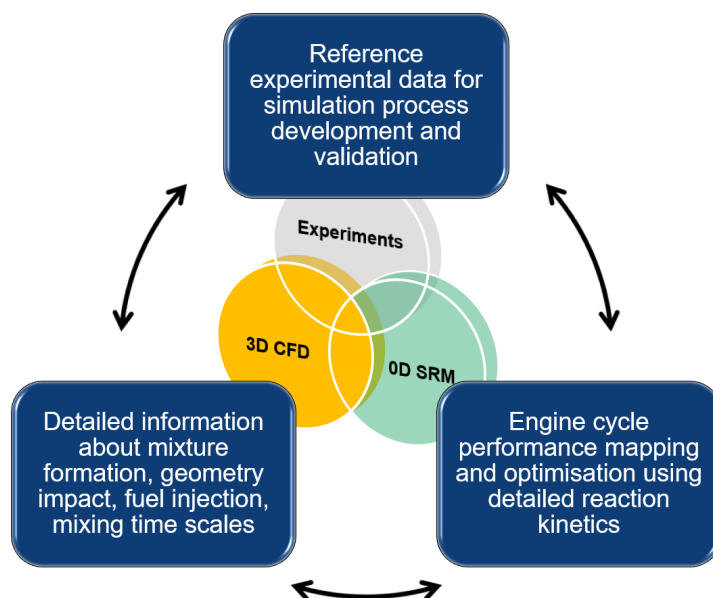


Figure 1: Overall approach to work in WP3

1.2 Workflow

The workflow combines numerical simulations and experimental works and is schematically presented in Fig. 2. Experimental data are used for numerical models development, calibration and then validation. They come from a single cylinder CI engine fueled with regular diesel fuel, biodiesel and finally biodiesel and ammonia both directly injected into the cylinder. In-cylinder pressure histories, and engine out emissions, such as nitrogen oxides (NO_x), carbon monoxide (CO), unburned and partially burned hydrocarbons (HC) and particulate matter (PM), are main outcome of experimental works.

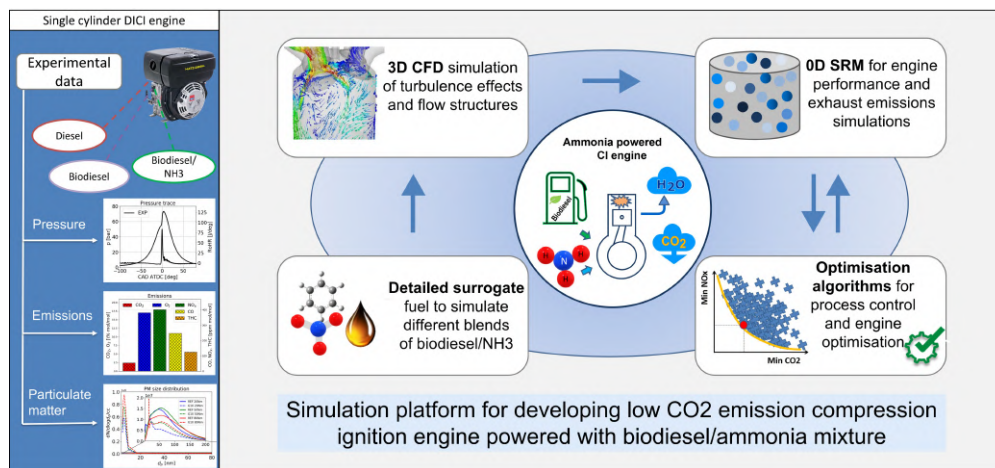


Figure 2: Simulation workflow and reference experimental data for WP3

The simulation phase of the project deals with 0D and 3D simulations of engine in-cylinder processes. The simulations employ detailed chemistry for the description of the combustion process and emissions formation, and are supported by various optimization algorithms for simulation process control and optimization.

Simulations employing the SRM aim at providing information about the in-cylinder performance and details of engine exhaust emission. Local phenomena, such as spray formation and vaporization, ignition characteristics and geometry effects, are obtained from 3D CFD. Both models are used complementarily to each other in a co-simulations and employ the same detailed reaction mechanism of ammonia/biodiesel. The reaction mechanism is used in the form of combustion progress variable (CPV) model that reduces dramatically simulation time down to a fraction of a second and without diminishing the accuracy of results.

Specifically, modeling and simulations in WP3 aim at providing information about the in-cylinder performance and exhaust emissions for a wide range of operating points with rather limited experimental available. Such simulations are considered as a virtual platform for extrapolating the findings from this work to new applications of ammonia-based fuels to CI engines.

1.3 Report structure

After a brief introductory chapter, in chapter 2 numerical 0D and 3D tools employed for engine simulations along with modeling of reaction kinetics towards developing ammonia biodiesel surrogate fuel model, used by the 0D SRM, are outlined. Aspects of modelling capabilities of 3D and 0D model along with detailed chemistry based fuel surrogate in the context of their application to an engine fuelled with ammonia and biodiesel are further discussed in chapter 3; in many aspects these applications were "first-time applications". Simulation results and findings are presented in chapter 2, 3 and 4. Major findings and details of results obtained are summarized directly at the end of each subsection. In turn chapter 5 summarizes overall main contribution of WP3 into the whole project ACTIVATE and is considered as its executive summary. The summary is followed by an information about publications derived from the works conducted in WP3.

2 Numerical tools

2.1 Introduction

The modelling and simulations employ two numerical models - the 0D SRM and 3D CFD. The use of both models is supported by various optimization algorithms that help to automate and speed-up their calibration. Furthermore, optimization algorithms are used during the application phase of the work, where various parameters study and optimisation of engine performance parameters are carried out. 3D CFD simulations are carried using software package Converge [1]. 0D simulations are based on LOGEngine platform [2] employing the SRM. 3D simulations focus on aspects of mixture formation, turbulence, mixing, combustion chamber geometry effects. In turn 0D simulations aim at providing information about emissions formation and engine performance parameters for wide range of engine operating conditions, including fueling strategies with ammonia.

2.2 0D engine modelling using SRM

The 0D modelling employs a variant for the SRM that is specifically tailored for the simulation of direct injection engines (DI). The model is a part of LOGEngine [2] simulation platform. This section presents basic information about 0D SRM to for readability of this report. We put emphasis on an overall concept of the SRM and the modelling of the mean representative mixing time. This is the key modeled parameter for the SRM that directly connects 0D and 3D modelling and simulations. The presented description of the SRM has been freely adopted from our previous works and publications [3, 4, 5, 6, 7, 8] that contain more comprehensive description of the SRM and its sub-models.

Model formulation

The SRM is a 0D model of physical and chemical processes occurring during the diesel engine cycle. It is formulated within the probability density function (PDF) approach for turbulent reacting flows that enables an exact treatment of chemical reactions. The SRM considers gas inside the cylinder as an ensemble of notional particles (Fig. 3). The particles can mix with each other and exchange heat with the cylinder walls. Each particle has a chemical composition, temperature and mass representing a point in the gas-phase. These scalars are treated as random variables and can vary within the cylinder. They determine the composition of the gas mixture and are described with probabilities using probability density function (PDF). The in-cylinder mixture is thus represented by a PDF in gas-phase space and the particles are realizations of the distributions. The solution for scalars, enthalpy and species mass fractions is obtained from the PDF transport equation. [2, 7]

Mixing time for the SRM

The mixing time history is the main input parameter for the SRM. It must be modeled because the mixing process cannot be predicted by 0D models. With respect to actual engines, mixing, time can be understood as an inverse of the frequency at which air, fuel

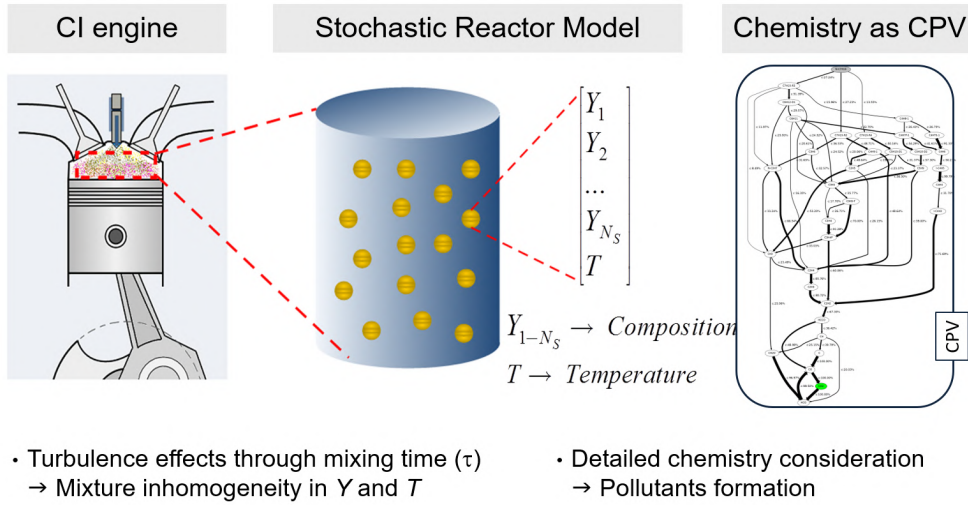


Figure 3: Concept of the SRM for the simulation of CI engines

and rest gases mix with each other. In the SRM, the mixing time describes turbulence time scales during the engine cycle. It governs the intensity of mixing between the particles that in turn influences mixture inhomogeneity in the gas phase for the scalars such as species mass fractions and temperature that have strong influence on the auto-ignition process, the local rates of heat release and pollutants formation. Hence, in some extent, it describes the local character of turbulent flow and chemistry interactions. The shorter the mixing time, the higher the intensity of the mixing operations on particles and vice versa. The modelling of the mixing time comes to the prescription of the evolution of particles in the gas-phase such that they mimic the composition change of real fluid parcels due to mixing caused by turbulence. The in-cylinder processes in diesel engines, such as flow pattern, fuel injection, mixture formation and pollutant formation, are characterized by different time and length scales. The scales change during the cycle that corresponds to the changes of mixing intensity and hence, to the changes of mixing time. Therefore, for the simulation of diesel engines, crank angle dependency of mixing time must be respected that is indicated by 3D CFD solutions (Fig. 4).

The history of mixing time can be deduced from the Favre-averaged turbulent kinetic energy and its dissipation calculated over the entire engine cycle. The result is referred to as turbulent mixing time (τ_t) - mixing time of velocity fluctuations and is calculated as $\tau_t = \tilde{k}/\tilde{\epsilon}$. With respect to SRM-based simulations, chemical reactions occur at the molecular level, where the mixing is governed by the mixing time scale of scalar fluctuations (τ_ϕ). The turbulent mixing time of velocity fluctuations (τ_t) and scalar fluctuations (τ_ϕ) are related via the mixing-time constant C_ϕ .

$$\tau_\phi = C_\phi^{-1} \tilde{k}/\tilde{\epsilon} = C_\phi^{-1} \tau_t. \quad (1)$$

In this equation, the constant C_ϕ can be interpreted as the velocity-to-composition decay time that depends on a given flow configuration. If the turbulent mixing time τ_t is known from 3D CFD calculations as an averaged history for the entire combustion chamber volume,

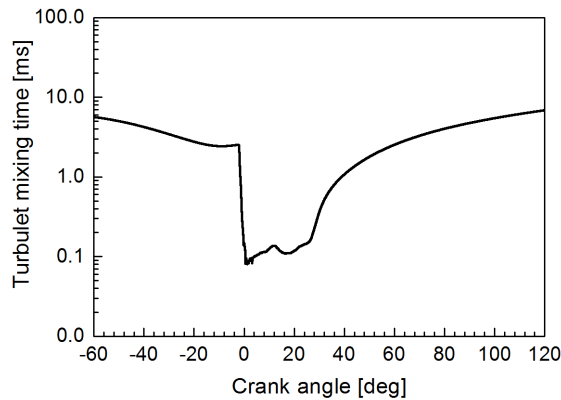


Figure 4: Example of turbulent mixing time from 3D CFD calculations of a Diesel engine.

the mixing time τ_ϕ can be determined by optimising the mixing constant C_ϕ . By optimizing the constant C_ϕ , the absolute values of mixing time τ_ϕ should approximate the mixing time effects at the molecular level. Equation 1 is the basic equation for the modelling of mixing time for the SRM. It indicates also a direct link between the 0D and the 3D simulation domains.

In the SRM version used in this work, the turbulent mixing time is determined from the $k - \epsilon$ model that was introduced in [7]. The model accounts for turbulent kinetic energy production due to inflows, swirl and squish flows, fuel injection, axial flows and gas compressibility. The turbulence dissipation is modeled in a zero-dimensional way using turbulence length scale and current turbulence level.

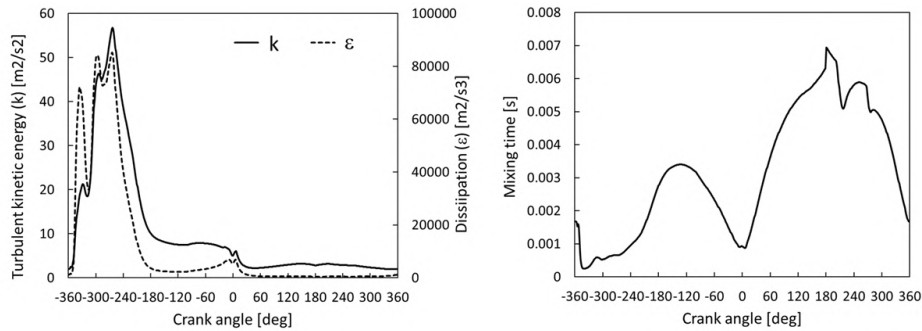


Figure 5: Exemplary histories of turbulent kinetic energy and its dissipation (left) and resulting history of the mixing time (right) [9]

2.3 LOGEfuel and tabulated chemistry

LOGEfuel [2] that is a database of reaction mechanisms representing combustion and emissions formation from different fuels. The LOGEfuel is compiled using the variable mechanism concept. The concept is summarized in Fig. 6) whereas its detailed description is found in [10].

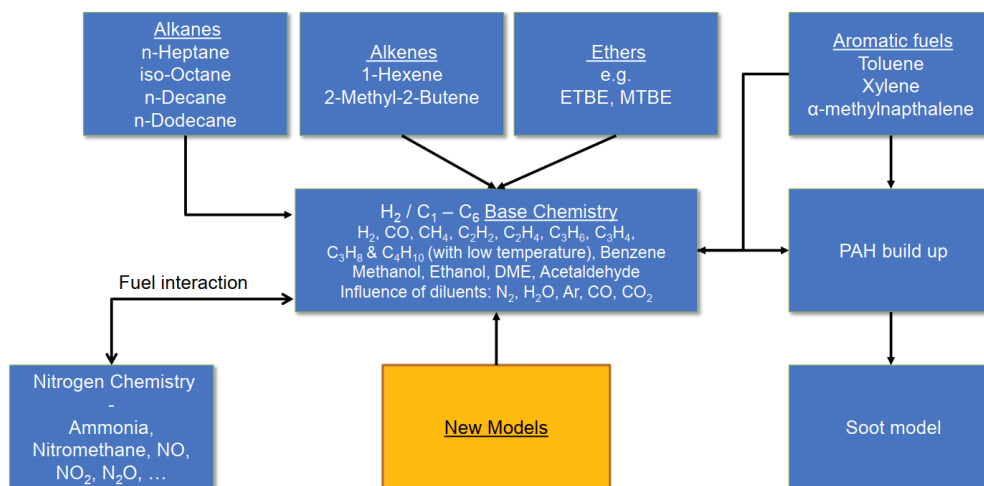


Figure 6: The variable mechanism concept [2].

All sub-models in the variable mechanism concept use the same base chemistry that contains reaction mechanisms describing the combustion process of following fuels and their mixtures:

- Hydrogen (H₂),
- Syngas (Mixtures of CO, CO₂ and H₂),
- Methane (CH₄),
- Acetylene / Ethyne (C₂H₂),
- Ethene / Ethylene (C₂H₄),
- Ethane (C₂H₆),
- Propane (C₃H₈),
- Propene (C₃H₆),
- Propyne (C₃H₄P),
- Propadiene / Allene (C₃H₄),
- n-Butane (C₄H₁₀),

- 1-Butene (C₄H₈-1),
- 1-Butene (C₄H₈-2),
- Iso-Butene (I-C₄H₈),
- 1,3-Butadiene (C₄H₆),
- Cyclopentane (CYC₅H₁₀),
- 1-Hexene (C₆H₁₂-D1),
- Benzene (A1),
- Toluene (A1CH₃),
- Methanol (CH₃OH),
- Ethanol (C₂H₅OH),
- Formaldehyde (CH₂O),
- Acetaldehyde (CH₃CHO),
- Dimethyl Ether (CH₃OCH₃-DME),
- iso-Octane (I-C₈H₁₈),
- n-DoDecane (N-C₁₂H₂₆),
- n-Heptane (N-C₇H₁₆).

The complete reaction scheme (v.2.00), which was a basis for the work presented here, consists of 566 species and 7370 reactions, including both forward and reverse reactions. The model includes NO_x chemistry and PAH growth model that is needed for simulating soot formation and oxidation. The model of PAH build-up process and oxidation captures the formation of soot precursor for different fuels. The models was validated against PAH measurements in different burner stabilized flames. The PAH growth is considered until 3 Ring species (A3R5 - acephentanthrylene, C₁₆H₁₀). This ensures compatibility of the model with the soot models implemented in LOGEsoft [2] software solutions. It also enables its coupling to third-party software. The core model of ammonia reaction mechanism is based on the work published in [11]. It was further updated within this work as described 3.2.

In this work, reaction kinetics for predicting the combustion process and emissions formation is used in the form of tabulated chemistry. The tabulated chemistry approach implemented in the SRM relies on a parameterization of the combustion progress as a function of Exhaust gas recirculation (EGR) rate, pressure, unburned temperature and equivalence ratio. The idea behind this approach builds on the assumption that an appropriately chosen progress variable can be used for reconstruction of the thermochemical state on the whole reaction trajectory. In the present work, the progress variable is defined based on the enthalpy of formation at the reference state and summed over all species that are included in

the mechanism. The combustion chemistry and emission source terms are precalculated and stored in a look-up table that is accessed during run time.

The use of tabulated chemistry dramatically reduces the computational cost, regardless of the size of the reaction mechanism. We can report CPU times that are below 0.1 second for the complete engine cycle calculated on a single processor core rated at 3.1 GHz.

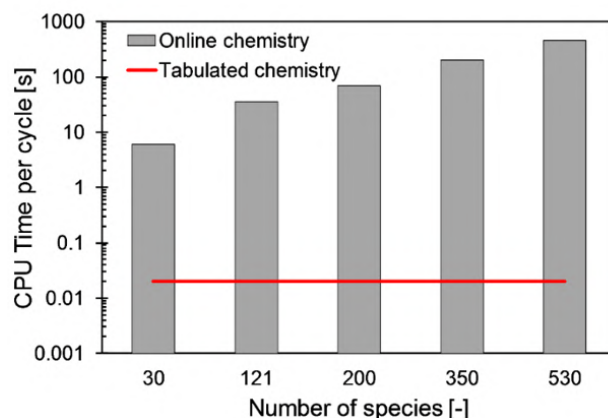


Figure 7: Computational cost of online and table-based calculations for mechanisms of different size

For the formation of emissions, the detailed soot model from [12] is used within the chemistry look-up table. The model distinguishes between particle inception, condensation, coagulation and agglomeration, surface growth, fragmentation, and oxidation with oxygen and hydroxyl radicals. The modelling of NO emissions is based on a transport equation describing the changes over time of the NO formation rate according to the thermal model. CO, CO₂, and unburned HC are directly retrieved from the chemistry look-up table. [8]

2.4 3D CFD Converge

Simulations are performed using the CONVERGE CFD software [1] with a similar setup as presented previously [13]. The code uses the collocated finite volume method with the Rhie-Choe interpolation scheme to solve the transport equations iteratively. Many studies show this code's capabilities for simulations of complex flows [14, 15, 16, 17, 18, 19]. The ICE flow is turbulent, therefore, one must solve the system of closed equations of motion, species transport, and energy conservation. The Navier-Stokes equations are subject to Reynolds decomposition with Favre averaging, and the closure for the turbulence fluxes is obtained by statistical modelling based on turbulence viscosity. The turbulence kinetic energy k and its dissipation rate ϵ are obtained with a two-equation RNG $k - \epsilon$ turbulence model widely adopted in ICE simulations. Different approaches can be used to track the liquid phase to model multi-phase spray flow during the liquid fuel into the in-cylinder gas mixture. To model liquid fuel spray, the Lagrangian solver is used to model discrete parcels, representing groups of identical drops and undergoing several physical processes. To emulate those effects, the employed models are selected based on recommendations from

previous CI engine simulation research [17, 18, 19, 20, 21, 22]. The spray breakup process is modelled using fundamental instability mechanisms of Kelvin-Helmholtz (KH) and Rayleigh-Taylor (RT). Only KH model is responsible for the primary breakup, whereas the secondary breakup is modelled by examining the competing effects of the KH and RT mechanisms as presented in [20]. In this approach RT model includes viscosity effects, and an ad-hoc definition of the breakup length is avoided. The No Time Counter (NTC) method [23] is used to account for droplet collisions, which result in grazing collisions, coalescence or stretching, and reflexive separation considered in the so-called post-collision outcomes approach. In addition, a collision mesh was applied with 2 levels of collision. The dynamic drag model is employed so that the drag coefficient includes variations in the drop shape. Uniform temperature distribution within each parcel was set, and fuel with real ammonia properties evaporated purely to NH₃ without any scaling factors applied to heat or mass transfer coefficients. Turbulent dispersion was modeled with the O'Rourke approach [24] where each component of added fluctuating velocity to the gas velocity follows a Gaussian distribution. Blob injection drop distribution was applied, and the parcels were evenly distributed throughout the solid cone spray.

An engine geometry motion is handled by creating a new mesh at each time-step instead of employing the moving mesh approach. Additionally, an adaptive mesh refinement (AMR) algorithm improves or adjust the grid size in the regions where it is needed based on pre-defined refinement criteria. The base grid cell size was set to 2 mm. Refinement criteria for AMR were based on sub-grid scale velocity of 1 m/s using 3 and 4 levels of embedding. However, an increase in one more level of embedding leads to a significant increase in the number of cells and CPU time but causes a minimal difference in the predicted results. Therefore we have applied 3 levels of AMR with 2 mm base grids based on our previous experience with engine modelling, and detailed grid dependency studies [13]. Moreover, the cell size of 0.25 mm in RANS simulations is small enough to provide correct liquid penetration length and thus is often set as the recommended value [25, 26]. Additionally, when it comes to the Lagrangian approach for spray simulations, the finer the cells, the more parcels have to be injected, and the cell size of 0.25 mm requires injection of over 512 000 parcels. Fixed embedding during crucial engine events and additional fixed embedding is applied with the refinement scale of 3 in the injectors regions to cover the cone shape of the expected spray plumes. In the reacting cases we have used SAGE combustion model with reduced chemical kinetic scheme for ammonia and n-heptane [27] consisting of 69 species and 389 reactions.

3 Simulation tool chain development

3.1 Tools chain concept

The modelling and simulations of engine in-cylinder processes employ three numerical models - the 0D SRM, the 3D CFD and LOGEfuel as database of fuel surrogates. 3D CFD simulations are carried using software package Converge [1]. They focus on aspects of locality of mixture formation, turbulence, mixing and combustion. The results of 3D CFD can support the 0D simulations with information about mixing time scales or mixture status that can be expressed by so called phi-T diagnostic maps. The CFD results indicate also about the potential mode of combustion (premixed or mixing controlled) based on the mixture status. This information help in selecting appropriate combustion model for 0D simulations. 0D simulations are based on LOGEengine ES platform from [2] with the SRM of engine in-cylinder processes. They aim at providing information about emissions formation and engine performance parameters for different engine operating points and fueling strategies with ammonia. These calculations are occupied by low computational costs - reaching real time and can be useful at early stage of engine development in helping to identify the potential directions of the development. LOGEfuel is a database of detailed reaction mechanisms describing the combustion process and emissions formation from variety of fuels. Figure 8 shows the overall concept of flow of information being exchanged between the numerical models and experimental

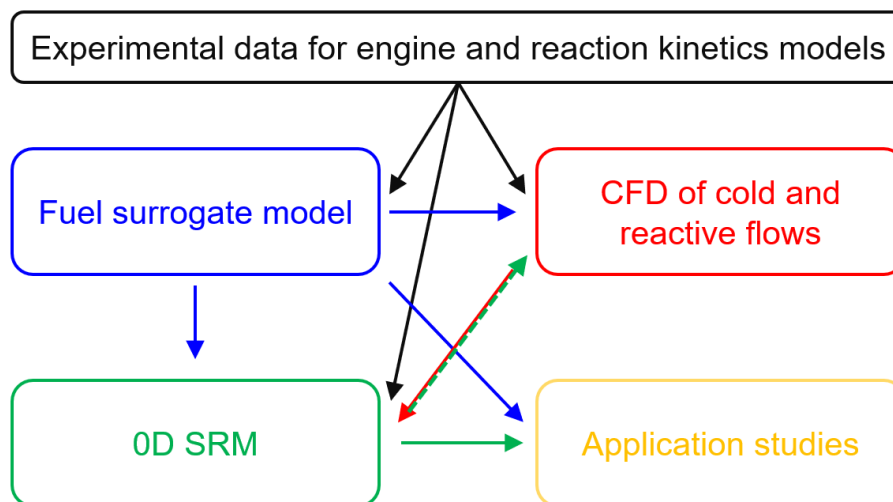


Figure 8: Concept of the flow of information between experimental data, 0D and 3D models that compose the tool chain.

The application of numerical tools in Figure 8 is supported by experimental data from an existing engine that provide basis and reference for retrofitting the engine into operation with different fuels. In the context of presented simulation process, the experimental data are used to developed both 0D and 3D CFD models, verify and validate their performance.

Typically needed minimum set of engine related data, besides geometry information and operating characteristic (fueling, equivalence ratio, engine speed, etc.), contains the data from engine indication that provides measured pressure history and exhaust emissions.

In turn, experimental data from fundamental studies on combustion and coming from rapid compression machine, shock tube and various reactors are used to validate reaction kinetics models that stands behind simulating of engine out emissions by 0D and 3D models.

Details of investigations using CFD, SRM and reaction kinetics, and pertaining to the development of an overall simulation chain are presented in the following subsections. These subsection contain preliminary investigations that were targeted at evaluating the performance of each numerical tool with respect to their application to an engine fueled with ammonia.

3.2 Ammonia/biodiesel chemistry development

This section provides an overview of the performed work on extending the LOGEfuel model by adding a bio-Diesel component updates done in the ammonia chemistry. The bio-Diesel model was compiled from different sources and a thorough revision of the kinetics has been carried out to improve performances of the model. The quality of both ammonia and biodiesel models was verified by a comparison of their performance against published experimental data.

Extension of the biodiesel surrogate

Biodiesel is modelled by methyl-decanoate as the single component surrogate. The methyl-decanoate model was taken from a previous LOGEfuel Diesel model and reaction rates have been updated to account for the new core model (LOGEfuel 2.01.00) and new findings by the scientific community. The updates in reaction rates and decomposition pathways follow mainly the work reported in [28] and the literature cited therein. An important part of the methyl-decanoate oxidation chemistry is the decomposition into linear alkanes with the chain length of 10 or 9 carbon atoms. To account for this, the n-decane model from the LOGEfuel diesel version 1.02 was included. Also for this sub-model rates has be adjusted to account for the fact that it had been developed for different base chemistry. The two models were combined with the LOGEfuel 2.01.00 by the listed below five main tasks.

- Unification of the species names.
- Unification of thermodynamic properties of all gas phase species included in both schemes.
- Selection of the best reactions rates for reactions which are included in 2 or 3 of the models.
- Decompilation of species which have been condensed into lumped species in the methyl-decanoate and n-decane mechanism but are distinguished in the LOGEfuel 2.01.00 model.

- Careful investigation of possible dead ends introduced due to missing decomposition pathways in the LOGEfuel 2.01.00.

Modifications in the ammonia sub-model

The LOGEfuel version 2.00.00 and 2.01.00 use the ammonia model published in [11] with the modifications included in [29] and [30]. While the model showed good predictions of several standard experiments it was found that it added - in combination with the methyl-decanoate model - a substantial numerical stiffness to the newly developed model. To overcome this problem the ammonia model was modified.

Stiffness removal and generation of CPV tables

The initial version of the ammonia / biodiesel model was found to predict standard experiments very well, but the process of generating CPV tables was very slow. The developed reaction scheme forced the solver to take very small time steps, in particular in regions which are relevant for the expansion phase in an engine cycle, after the main combustion. The reaction scheme was modified to reduced the stiffness by repeating the work steps outlined below using LOGEresearch package [2].

1. Compile a CPV table for ammonia / biodiesel mixtures.
2. Identify a combination of initial parameters for which the tabulation takes very long.
3. Identify the temperature point that needs the longest calculation time for that combination.
4. Run a life time analysis for this point to identify the species with the shortest lifetime.
5. Identify the reaction that forces the solver to take very small time steps, and modify that reaction.
6. Repeat calculation from point 4 and control if life time is longer. If not, repeat step 5.
7. Start again from point 1.

This process has been repeated countless times, until it was possible to compile a CPV table in the listed below parameters range.

- Pressure: 1 [bar] to 200 [bar].
- Equivalence ratio: 0.05 [-] to 6.0 [-].
- EGR rate: 0% to 40%.
- Unburned initial temperature: 300 [K] to 1400 [K].
- Fuel mass fraction: from pure ammonia to pure methyl-decanoate in 20% steps.

About 100 reactions have been modified in total, until no further nonphysical small life times have been observed. In addition to this, where necessary, the thermodynamic properties of species have been updated. When reactions belonging to the ammonia sub-mechanism have been modified, the selected rate was compared to recently published models and more recent reaction rate parameters have been evaluated in terms of life time and numerical stiffness. For most of the reactions it was found that more recent rate parameters did not reduce the stiffness. This is expected since those rates allow a decent prediction for the conditions in standard experiments (fairly low pressure and gas mixtures and temperatures showing a high reactivity) but tend to fail or cause problems for regions that can be found in an engine and need to be considered during tabulation (e.g. lean mixtures at high pressure and low temperatures).

Validation with experimental data

The final compiled reaction contains 1307 species and 13683 reactions. In the next sections, validation of the reaction scheme against published experiments for ammonia and biodiesel is presented. The validation work relies on the experimental data available at the time of executing the work. Due to the size of the mechanism a validation against premixed flames was not possible and is limited to shock tube experiments and jet stirred reactor experiments. Reference and experimental ignition delay times were obtained in shock tube experiments. They are modeled as homogeneous constant volume reactors in LOGEresearch. The jet stirred reactor experiments are modeled as perfectly stirred reactors with a constant temperature to account for heat losses.

- Ignition delay time for ammonia at different conditions

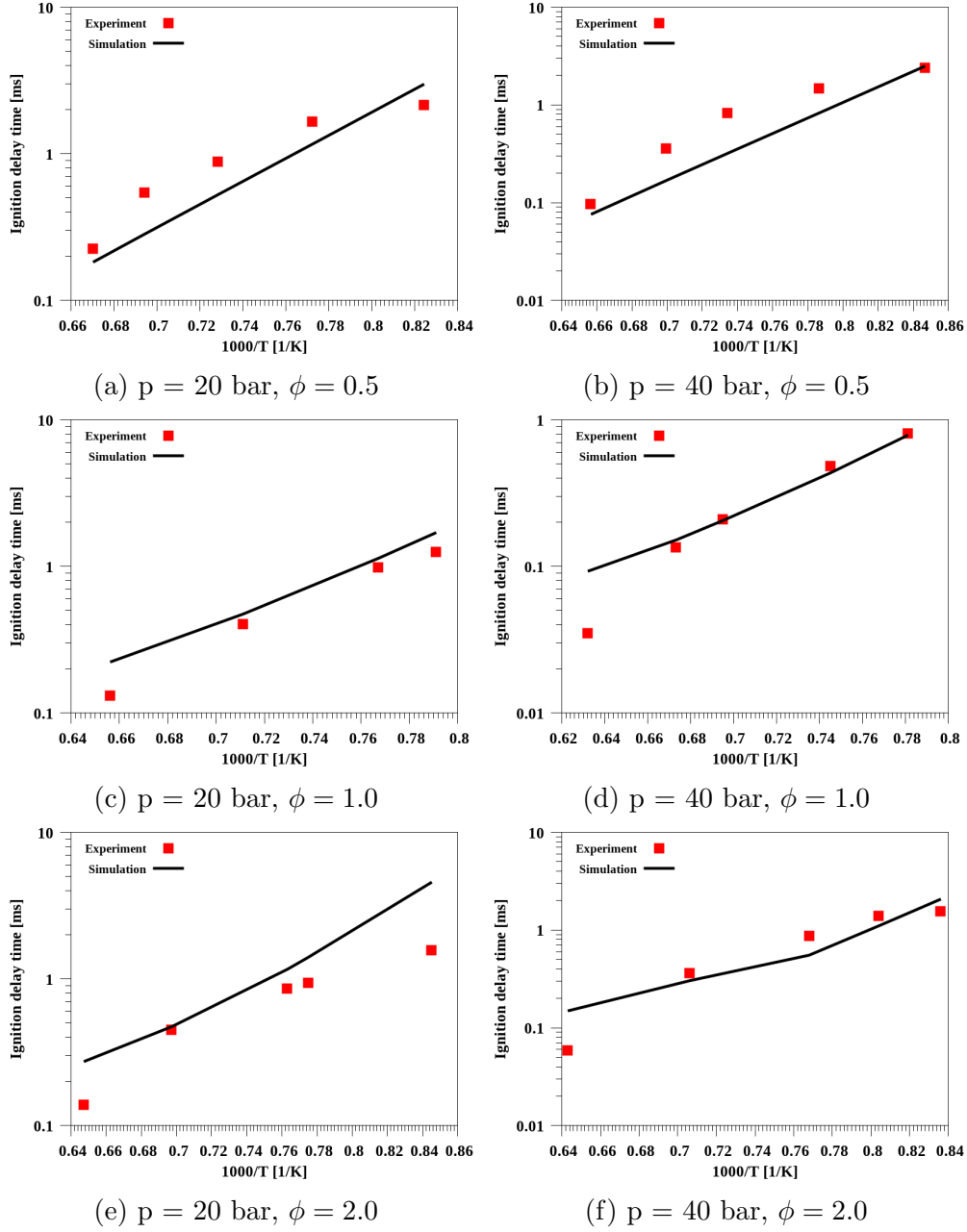


Figure 9: Ignition delay times of NH_3/air mixtures at different equivalence ratios and pressures. Symbols represent experimental data from [31] whereas lines represent calculations.

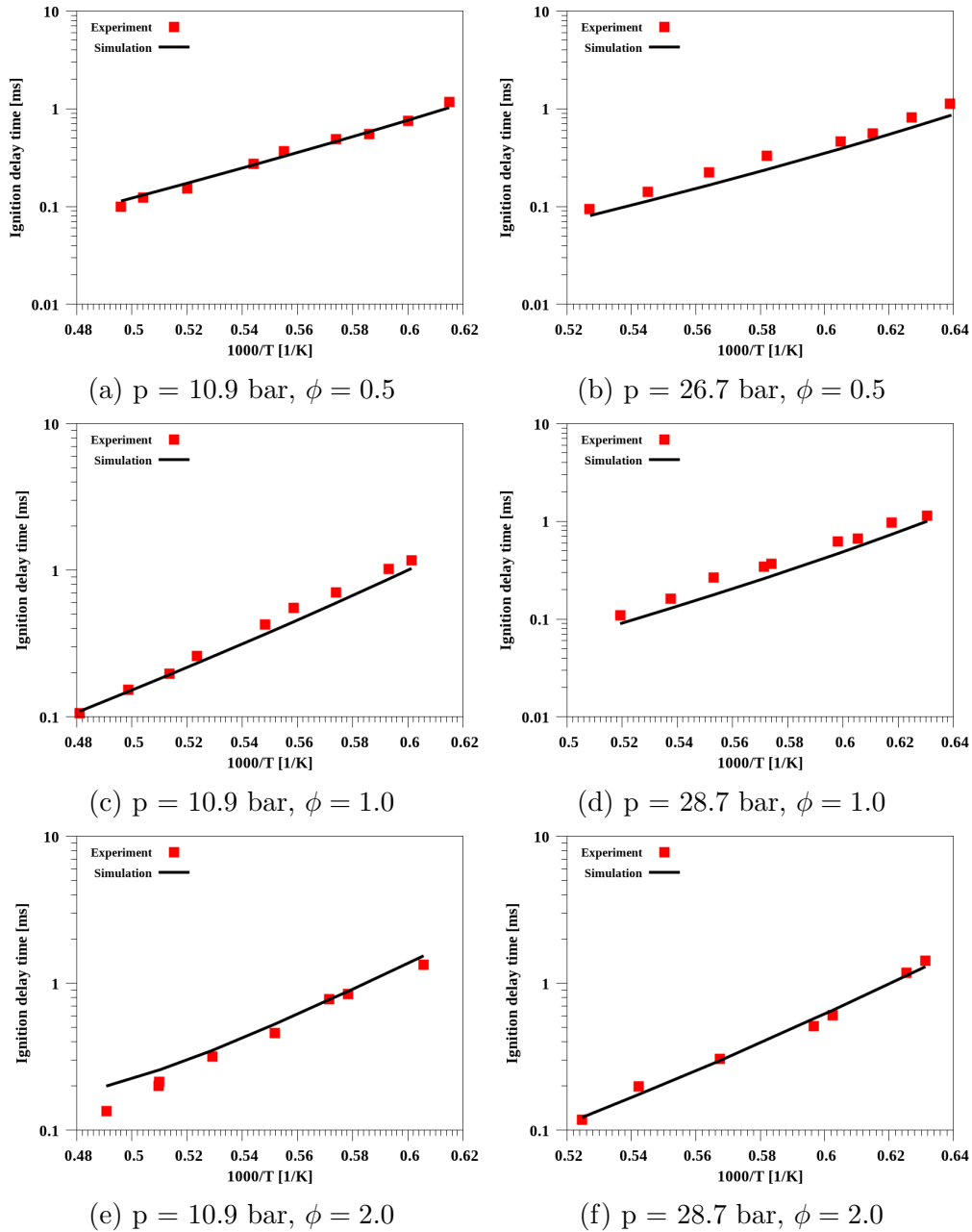


Figure 10: Ignition delay times of NH_3/O_2 mixtures diluted in 99% Ar at different equivalence ratios and pressures. Symbols represent experimental data from [32] whereas lines represent calculations from the developed model.

- Ignition delay time for methyl-decanoate (MD)

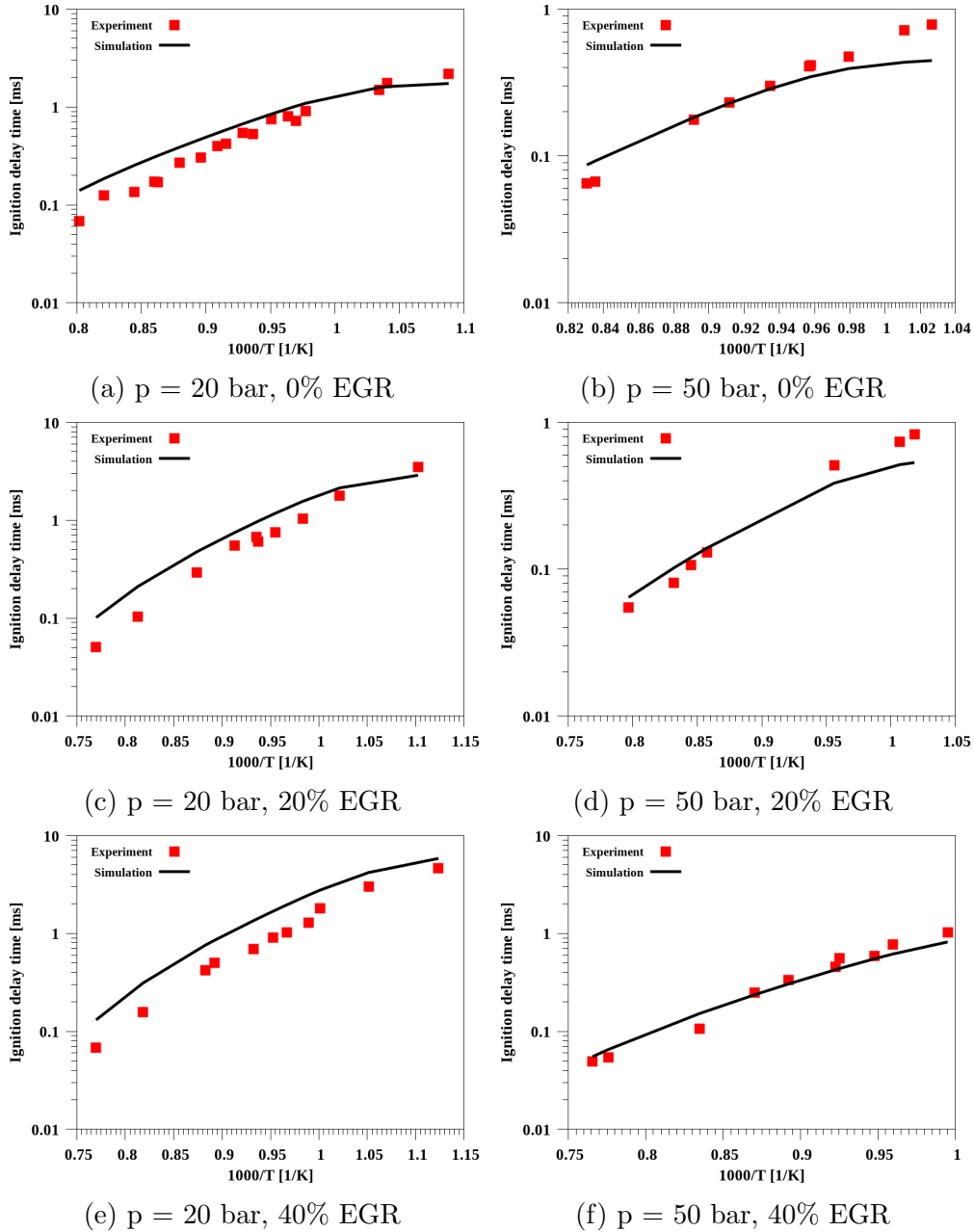


Figure 11: Ignition delay times for mixtures of MD/air at different pressure and EGR rates. EGR was defined as the complete products of stoichiometric MD/air combustion. Symbols represent experimental data from [33], lines are calculations with the developed model.

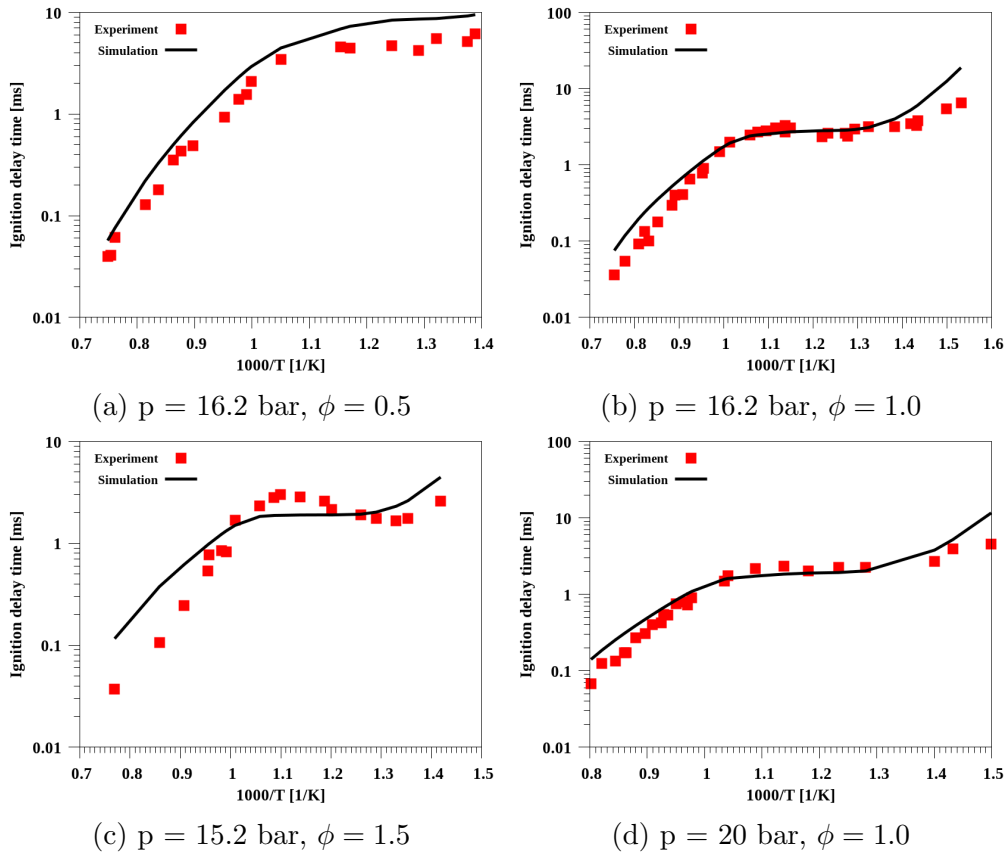


Figure 12: Ignition delay times for MD/air mixtures at different equivalence ratios and pressure. Symbols represent experimental data from [34] and [35], whereas lines calculations with the developed model.

- Simulations of MD and NH₃ in jet stirred reactor

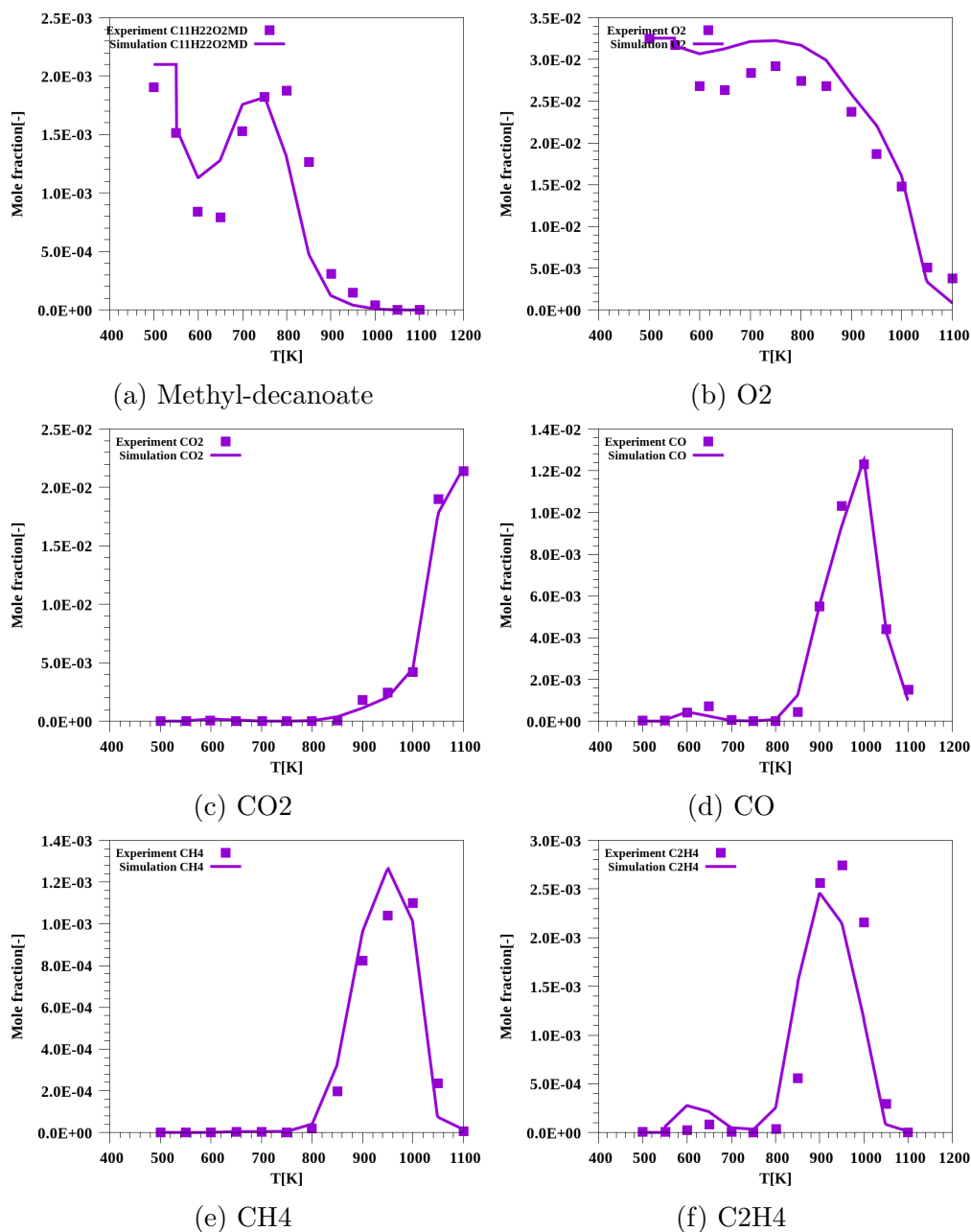


Figure 13: Evolution of species concentration in the oxidation of MD/O₂/Ar (0.0021/0.03255/0.96535) mixtures in jet stirred reactor at 1.6 bar and 1.5s residence time. Symbols represent experimental data from [36] and lines are calculations with the developed model.

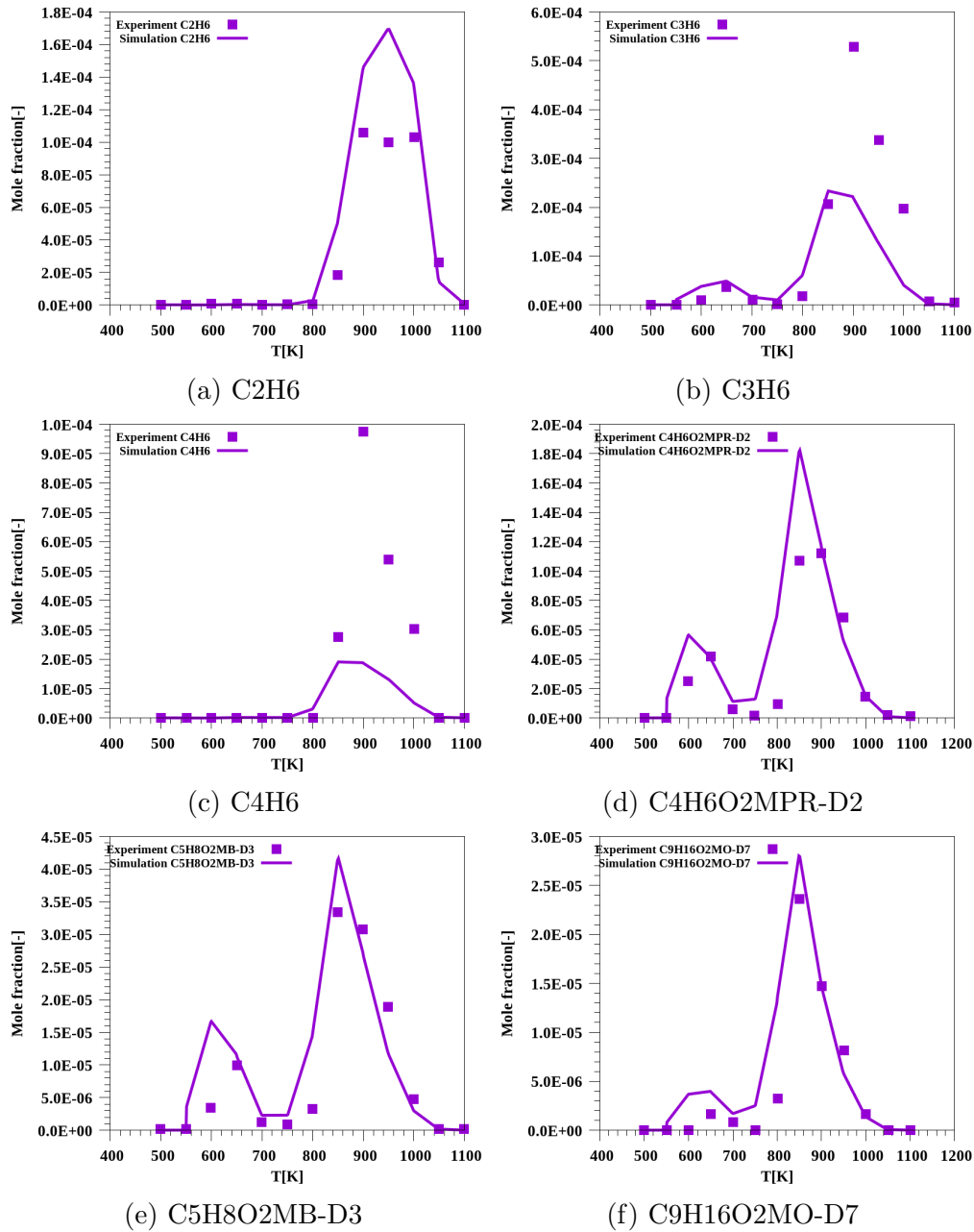


Figure 14: Evolution of species concentration in the oxidation of MD/O₂/Ar (0.0021/0.03255/0.96535) mixtures in jet stirred reactor at 1.6 bar and 1.5s residence time. Symbols represent experimental data from [36] and lines are calculations with the developed model.

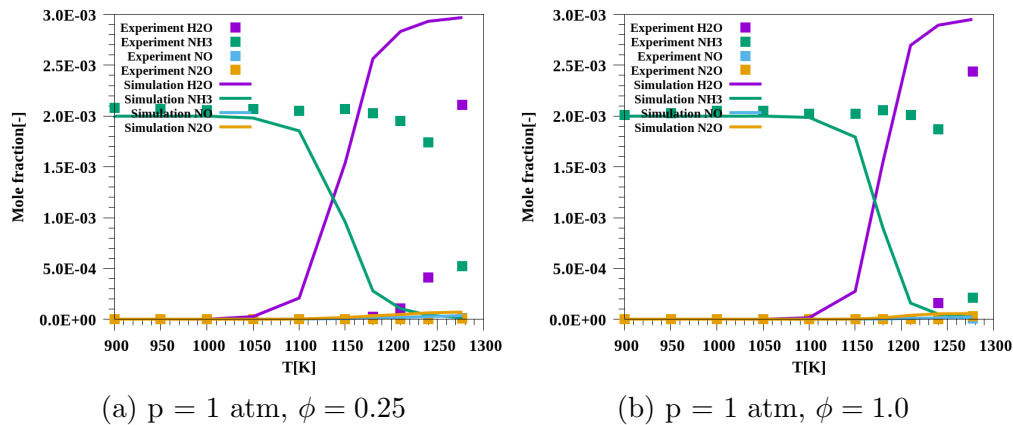


Figure 15: Evolution of species concentration in the oxidation of $\text{NH}_3(0.2\%)/\text{O}_2(1\%)/\text{N}_2(98.8\%)$ mixtures in jet stirred reactor at different equivalence ratios and residence time of 1s. Symbols represent experimental data from [37], whereas lines represent calculations with the detailed mechanism.

Summary

Overall, ignition delay times predicted by the model match with the available experimental data for ammonia and methyl-decanoate. The oxidation kinetics of methyl-decanoate is also captured for most of the quantified and major species such as CO, CO₂, CH₄, C₂H₄. Similarly well are captured intermediate species.

The developed model shows too high reactivity for the oxidation of ammonia in the jet stirred reactor experiment reported in [37], while the trends in species consumption and formation are well matched. However, this experiment was published just about one month before finishing the work and hence could not be used as a reference during the development process. The oxidation of ammonia starts about 100 K too early.

During the work on the current version of the mechanism, there was no published experimental data for ammonia/biodiesel mixtures. The measurement of combustion properties of binary ammonia/hydrocarbon fuel mixtures have started recently. Most of the current publications are focused on ammonia/hydrogen mixtures or mixtures with n-heptane in rapid compression machines. The developed in this work package mechanism was successfully used to compile an ammonia/biodiesel dual fuel CPV table that is needed for 0D SRM-based engine simulations.

3.3 3D CFD for investigating ammonia injection

Scope of work

The first phase of 3D CFD works aimed at providing calibrated engine model suitable for investigating ammonia combustion in CI engines. Firstly, geometrical analysis on the selected GDI injector position regarded as optimal for proper ammonia spray injection is presented. Secondly, numerical analysis is presented where the modelling approach is explained and validated against obtained experimental data from the liquid ammonia spray injections into the cylindrical vessel with optical access with varying initial pressure and temperature.

Geometrical analysis - GDI positioning

The use of pure ammonia in the compression ignition engine would be extremely difficult. Therefore it is necessary to use a pilot fuel to promote ignition and ensure a proper combustion process. The target pilot fuel in ACTIVATE project is rapeseed biodiesel, and the usage of two different fuels requires the installation of two separate fuel lines and two different injectors. In the WP1 of ACTIVATE project for biodiesel fuel, a standard diesel injector was used, whereas a Gasoline Direct Injection (GDI) type of injector was adopted to inject liquid ammonia spray. Figure 16 shows the schematic placement of the two injectors. Diesel injector (first from left) enters the chamber nearly perpendicularly (83°) to the engine head and aiming the fuel spray towards the center of the cylinder bowl. Due to space and manufacturing issues, there is little freedom in placing the GDI injector. It is located 1.5 cm from the diesel injector and enters the chamber at an angle of 32° . Such a position constitutes a risk of hitting the head's wall by some of the spray plumes, which may negatively affect the spray and, consequently, the mixture formation. For that reason, three additional scenarios have been planned: a) one of the nozzles is sealed (third picture in Fig. 16); b) injector is rotated by 30° and the two nozzles are sealed (fourth picture in Fig. 16); c) three nozzles are sealed (fifth picture in Fig. 16). The occurrence of spray-wall interaction will rely on:

- spray plume direction depended on the injector nozzles geometry;
- full outer spray angle and plume cone angle depended on the fuel type, thermodynamic conditions, or flashing.

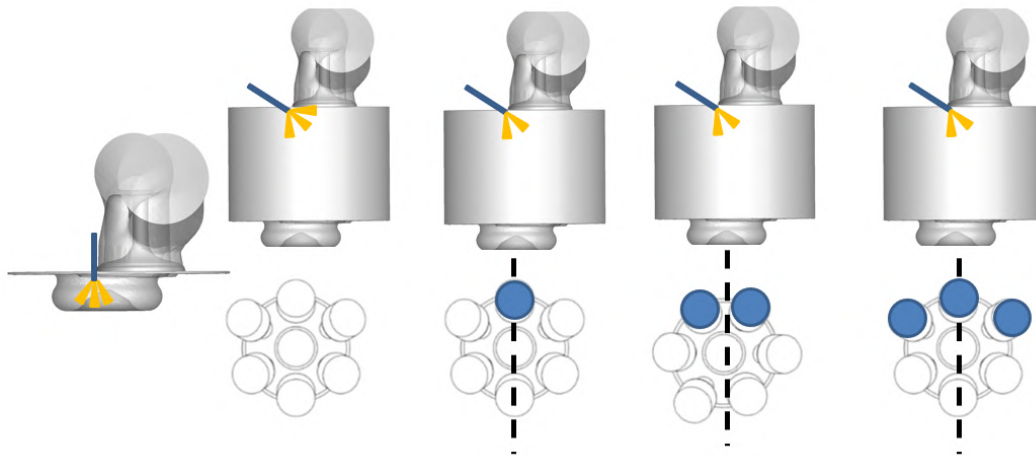


Figure 16: Schematic position of the pilot biofuel diesel injector (first left) and the GDI ammonia location with four configuration options.

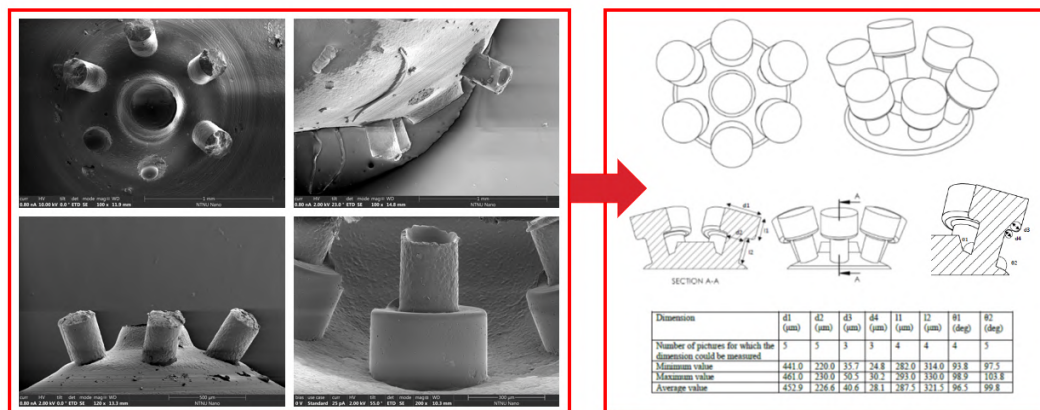


Figure 17: Scanning electron microscope (SEM) images (by *Amin Hossein Zavieh, NTNU Nanolab*) and CAD geometry (by *Jessica Gaucherand [38], NTNU ComKin*) of the adopted GDI injector interior.

Characteristics of gasoline multi-hole GDI injectors are very different from those of diesel injectors. Generally, their spray angles are much narrower ($60^\circ - 95^\circ$) compared to diesel injectors, where the angles can be two times wider ($140^\circ - 160^\circ$) [39]. The adopted GDI injector has six symmetrically oriented nozzles, and its internal geometry has been characterized by Gaucherand [38] using silicon mold technique and scanning electron microscope (SEM) images and is presented in Fig. 17. For the purpose of the present study, just a few of the collected dimensions related to the nozzles locations are needed as the detailed flow through the injector is not considered. The fuel spray is modeled with the Lagrangian approach injecting discrete liquid fuel parcels and will be described in the next section. Therefore, only the nozzle orifice diameter, radial distance from the injector seat, and the angle between the injector axis and an individual nozzle axis (drill angle) were required, and their values are 0.4529 mm, 0.6 mm, and 19° , respectively. Injector characteristics nomenclature has been

adopted from the Engine Combustion Network (ECN) [39]. Figure 18 shows a schematic representation of the GDI position in the chamber. The injector enters the chamber at an angle of 32° with respect to the engine head. Therefore, the full multi-nozzle spray cone angle, which would lead to the interaction with the wall, is equal to 64° . The angle of 38° marked with blue lines is the double of the drill angle, and for simplicity, it is assumed that the drill angle is the minimum full outer spray angle. As shown in Fig. 18 in such a geometrical configuration, the spray will not hit the head's wall. However, under different thermodynamic conditions or occurrence of fuel super-heat and associated with it flash boiling phenomenon, the spray width can increase [26]. Currently, the literature lacks published data for ammonia liquid spray in GDI engine configuration. Nevertheless, relevant ongoing research is being conducted at the University of Orléans, and data from the first study on ammonia spray characteristics using GDI in the cylindrical vessel with optical access with varying initial pressure and temperature has been obtained from Pelé et al. [40]. It has been found that the spray angle at half of the penetration length varied between 48° and 75° dependently on the thermodynamic conditions. Assuming proportional increase (56%) in the spray angle in the case of the present study, one can approximate the maximum spray angle to be equal to 59° (see green lines in Fig. 18), and it is still too small for the spray to interact with the wall.

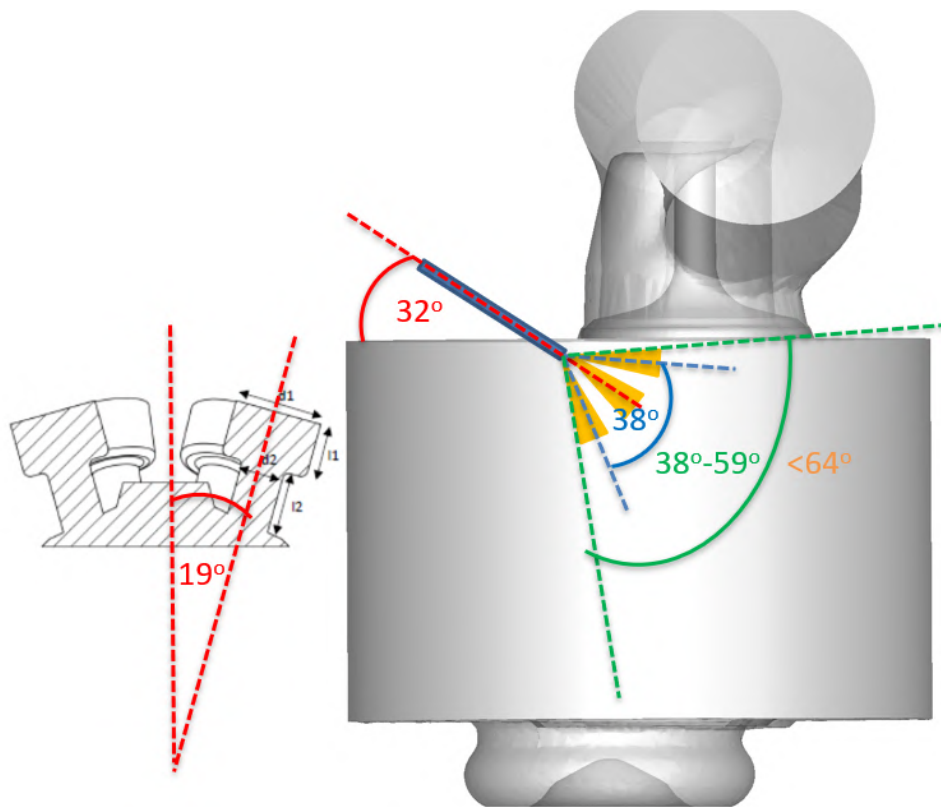


Figure 18: Schematic representation of the GDI position in the chamber, including relevant angles.

Pelé et al. [40] also reported that ammonia spray characteristics are more sensitive for

thermodynamic conditions than gasoline or ethanol. Moreover, ammonia spray has a diverse geometry and evolves differently with temperature and air density changes. Due to ammonia liquid properties, the fuel superheat state can be obtained much easier, and thus flash boiling and eventually the spray collapse can occur. Based on the above findings, it can be concluded that the spray wall interaction is unlikely to happen, and investigation of the four options of GDI configuration shown in Fig. 16 is of less importance for the mixture formation than ammonia spray behavior affected by thermodynamic conditions. Therefore, the following section focuses on the spray modelling issues and challenges related to the specific ammonia spray behavior accounting for flash-boiling. Different modelling setups are assessed and validated in order to accurately represent the flow and spray characteristics under different thermodynamic and superheat degree conditions met at various injection timings. These results are going to be crucial in the development of an ammonia injection strategy.

Ammonia sprays and flash boiling

Ammonia has a high vapor pressure at low temperature (it is a gas at normal conditions), and if injected as a liquid at high pressure to a low-pressure environment below its saturation pressure, a flash boiling will occur. If a liquid is undergoing flash boiling to regain thermodynamic equilibrium, it is then called as superheated. To quantify that state, the superheat degree can be introduced as the difference between liquid temperature T_f and the boiling point T_b dependent on the ambient pressure. However, it is easier and more common to use a non-dimensional superheat degree as the ratio of ambient pressure p_a to saturation pressure p_s of the liquid at temperature T_f . Therefore, superheat can be altered by the fuel temperature or the ambient pressure, and the liquid is superheated if $p_a/p_s < 1$. Flash boiling is similar to cavitation, however, it is induced thermally rather than mechanically [22]. This process intensifies the rate of change in droplets' mass and reduces their size. During flash boiling in liquid fuel, vapour bubbles are formed and grow until reaching a certain size, eventually leading to droplet explosion; thus, the breakup process is enhanced. Consequently, an increased number of smaller droplets are formed with additional radial velocity component, which causes spray widening. This phenomenon has been investigated previously for gasoline or alcohols sprays from multi-nozzle GDI injectors [26, 41]. In fact, they have observed spray widening and decreased penetration length for $p_a/p_s < 1$ [26]. However, due to the widening effect, single spray cones start to interact with each other what causes a pressure drop and eventually, at around $p_a/p_s = 0.3$, lead to so-called collapse into a single-body spray. Therefore, below superheat degree of 0.3, the trend is reversed, and the spray becomes thinner and longer. Such behaviour was confirmed for n-heptane, methanol, ethanol and thus was regarded as independent of the fuel. As a result of this study, Xu et al. [26] have proposed correlations for a spray penetration and spray-plume width in the following form:

$$S = (3.62 + 7.1 \frac{p_a}{p_s}) (\frac{\rho_a}{\rho_l})^{-0.268} \quad \text{and} \quad W = \frac{1.5 (\frac{\rho_a}{\rho_l})^{-0.38}}{1 + e^{3.8(p_a/p_s - 0.746)}} \quad (2)$$

for $0.3 \leq \frac{p_a}{p_s} < 1$ and for $\frac{p_a}{p_s} < 0.3$:

$$S = (9.2 - 12.45 \frac{p_a}{p_s}) (\frac{\rho_a}{\rho_l})^{-0.268} \quad \text{and} \quad W = (9.2 - 12.45 \frac{p_a}{p_s}) (\frac{\rho_a}{\rho_l})^{-0.38}, \quad (3)$$

where S stands for spray penetration and W is spray plume width. These correlations can be used to properly set up a spray model for a range of superheat degrees found during different fuel injection timings in engine simulations.

Flash boiling enhances phase change from liquid to gas; thus, change in the drop mass is more significant and can be regarded as an increased evaporation rate. Prince et al. [42] proposed a model with the assumption of spherical droplets whose surface temperature at superheated conditions is equal to the saturation temperature of the fuel. The total change in the drop mass is driven by heat transfer to the droplet surface: 1) from the surrounding environment (sub-cooled term); and 2) from the droplet center (superheat term). Therefore, being precise, such a model describes so-called external flash boiling. The model of Price et al. [42] is implemented in the CONVERGE code and has been recently employed in the CFD study of Duronio et al. [22] aiming to reconstruct flash boiling spray morphology in the case of ECN spray G. Their study is a relevant reference for simulation set up of a standard and flash boiling spray, however it is limited to only one global superheat condition and gasoline as a fuel. Properties of ammonia (e.g. high latent heat of vaporization) may have consequences leading to deviations from previously derived correlations and in general different spray behaviour, yet these are to be explored in this research project.

With respect to standard spray modelling using the Lagrangian approach, the following submodels or settings were found to be influential when modelling flash-boiling sprays [42]:

- model for evaporation,
- spray breakup model parameters,
- prescribed cone angles,
- droplet collision model,
- initial droplet diameter,
- heat transfer coefficient.

Experimental data

The literature lacks detailed experimental studies of liquid ammonia sprays. A recent study by Okafor et al. [43] concerns ammonia spray in the context of gas turbine application in a single-stage swirl combustor where the system is very different from GDI and operates at much lower pressures. The only relevant study for the present considerations is a very recent work performed at the University of Orléans by Pelé et al. [40]. Their experiment was performed in a constant volume chamber with optical access to investigate ammonia, ethanol, and gasoline spray characteristics under different thermodynamic conditions. They applied the Schlieren technique to capture images of liquid and liquid + vapor spray and measured penetration lengths, the angles near the injector, and the angles at half-penetration length. Their results show that the ammonia spray geometry behaves differently than the other fuels, and its sensitivity to air density and temperature is greater. It was pointed out that these experimental measurements are the first data for ammonia injection using GDI injector. Therefore, this data set has been adopted in the present study as the only available

source of information about the ammonia GDI spray characteristics. For the purpose of the present work, the case where the fuel was injected into the atmosphere at a pressure of 2 bar and temperature of 20°C was selected. This case is interesting because it represents the highest superheat degree, and since the fuel temperature was not measured, it was proposed to assume that its temperature is equal to the ambient temperature of 20°C [40]. In such conditions, superheat degree expressed as ambient to saturation pressure ratio p_a/p_s is equal to 0.23. The spray injections were performed with a Bosch seven-hole GDI injector with 365 μm diameter nozzles at 120 bar.

The effect of vaporization model

Four approaches to account for liquid droplets' evaporation have been assessed. In the drop evaporation process, the rate of droplet radius change was calculated with the method employing the Frossling correlation [44] or using Chiang correlation [45]. Two different methods were then combined with or without the flash boiling model of Price et al. [42] to account for intensified evaporation.

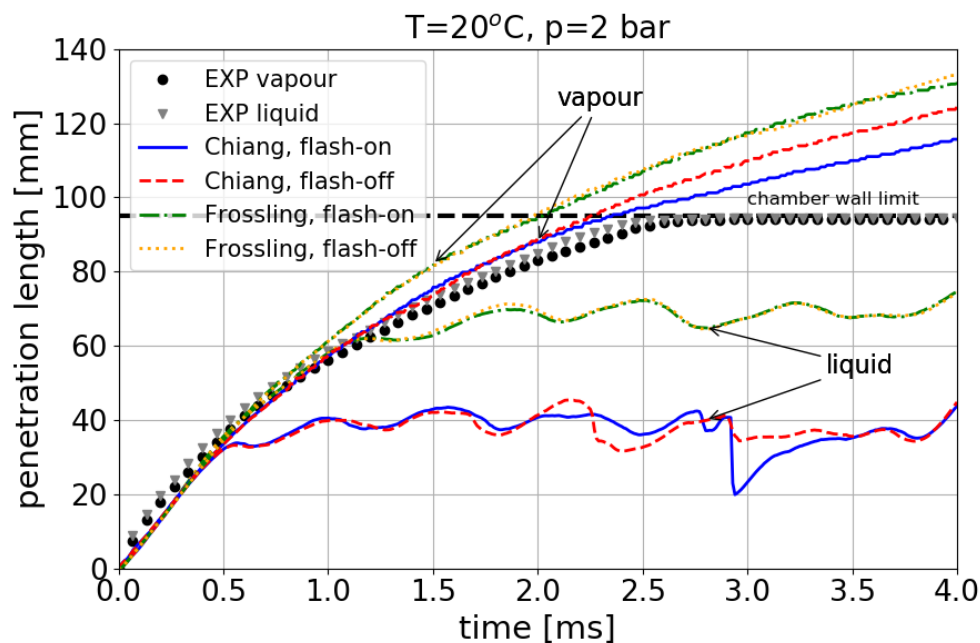


Figure 19: Ammonia spray penetration lengths (vapour and liquid) at $T=20^\circ\text{C}$ and $p=2$ bar calculated with different vaporization approaches compared to the experimental data.

Figure 19 shows the numerical results of penetration lengths (liquid and vapour) compared to the experimental data. The first very evident observation is that Frossling correlation provides higher liquid penetration length than the Chiang model by around 50%. The difference in vapour penetration is less significant, but still Frossling model gave higher vapor penetration lengths. The flash-boiling model in conjunction with Frossling correlation has not influenced the penetration length results. However, in conjunction with Chiang correlation flash-boiling model decreased vapour penetration length after around 2.5 ms.

The differences in LPL results are somehow less noticeable. In addition, LPL model results do not match the experimental data for which no clear separation between LPL and VPL exists. It should be pointed out here that the experimental data are flattened after 2.5 ms, because of the presence of the chamber wall (denoted with a dashed black line), which was not considered in our calculations. Simulations in the following sections used the Chiang evaporation model with the Price flash boiling model.

The effect of spray breakup model parameters

The spray breakup mechanism is modelled using the KH-RT approach, and as mentioned above, this process can be altered significantly if flash boiling occurs, changing the spray geometry. Tables 1 and 2 contain four different sets of model constants used in RT and KH models, respectively. They concern about breakup time and size constants. Modifying their values by increasing or decreasing breakup time constants ($B1$ or $C1$) breakup occurrence can be delayed or advanced, respectively. Altering the breakup size constants ($B0$ and CRT), the size of the resulting droplets can be controlled [22]. The first three sets of parameters denoted as "Diesel", "GDI non-flashing" and "GDI flashing" are recommendations from the literature and best practice guidelines in Converge software [1]. The fourth set of parameters was proposed by Duronio et al. [22] for flash boiling example of ECN spray G. As shown in Fig. 20 the first three sets of parameters provided very similar results of penetration lengths with marginal differences between them. However, the fourth set of parameters where $B1$ constant was reduced from 7.0 to 5.0 had a much stronger effect, as both LPL and VPL have decreased significantly, and the LPL value fluctuated. Indeed, a decrease in KH breakup time constant $B1$ advanced breakup occurrence, but VPL was much lower than the experimentally measured values. On the other hand, Duronio et al. [22] pointed out that $B1$ can vary for different injectors, and apparently, the value of 5.0 is not adequate for the present case. Simulations from the previous and the following sections used a "GDI-flashing" set of breakup model parameters.

RT model parameters	Diesel	GDI non-flashing	GDI flashing	Duronio [22]
$C1$ - time constant (0.1-1.0)	1.0	1.0	0.1	0.1
CRT - size constant	0.1	0.6	0.25	0.15

Table 1: Rayleigh-Taylor breakup model parameters recommendation.

KH model parameters	Diesel	GDI non-flashing	GDI flashing	Duronio [22]
$B0$ - size constant (0.61)	0.6	0.6	0.6	0.61
$B1$ - time constant (5-100)	7.0	7.0	7.0	5.0

Table 2: Kelvin-Helmholtz breakup model parameters recommendation.

The effect of cone angle

Using a purely Lagrangian approach to model fuel spray detailed fluid flow through an injector is not considered. Parcels are injected directly from the specified locations of the

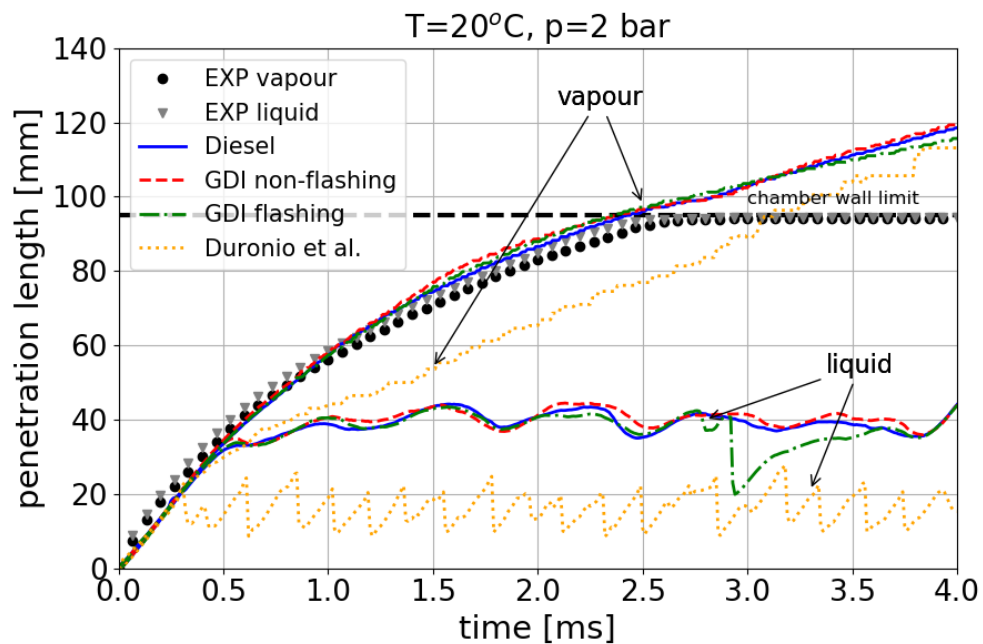


Figure 20: Ammonia spray penetration lengths (vapour and liquid) at $T=20^{\circ}\text{C}$ and $p=2$ bar calculated with different spray breakup model parameters compared to the experimental data.

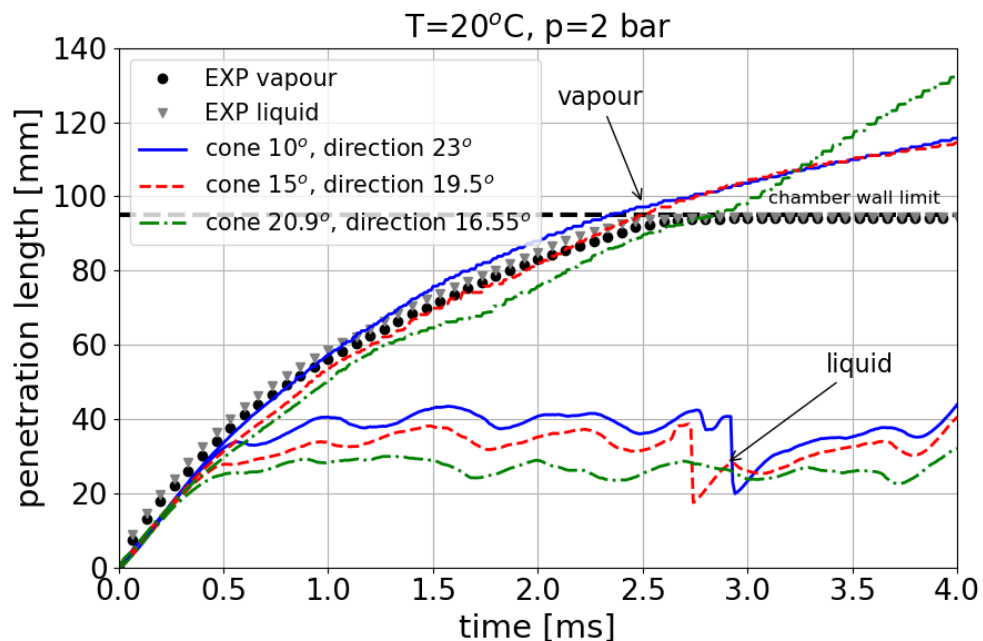


Figure 21: Ammonia spray penetration lengths (vapour and liquid) at $T=20^{\circ}\text{C}$ and $p=2$ bar calculated with different cone angle and plume direction compared to the experimental data.

injector's nozzles, and their outlet characteristics have to be specified, including plume cone angle. In this section, the effect of the prescribed cone angle and plume direction is assessed. Both angles are selected to match the full outer spray angle equal to 54° , measured as the angle at half the penetration length by Pelé et al. [40]. The values of the angles are provided in Table 3. The first set corresponds to the case where the plume direction is equal to the drill angle of 23° taken from the injector geometry and the resulting cone angle has to be equal to 10° , which is also the setup used in the simulation results showed in the two previous sections. During flash boiling, the single spray plume is widened, thus for the second case, the plume cone angle was increased by 50%. In the third set, the ratio of plume cone angle to plume direction was chosen to correspond to the one used in the flash-boiling case of ECN spray G applied by Duronio et al. [22]. Simulation results of spray penetrations for the three selected sets of angles are shown in Fig. 21. A clear trend is observed that the wider spray plume cone angle and the narrower plume directions are, the shorter the spray penetration is.

Plume cone angle	Plume direction	Full outer spray angle
10°	22°	54°
15°	19.5°	54°
20.9°	16.55°	54°

Table 3: Different set-up of spray angles

Discussion and thermal analysis

In the three previous sections, the effect of selected important spray model parameters was analysed. Although VPL results agreed well with the experimental data, none of the models reproduced LPL accurately. To find the reason for such a deviation, it is worth considering why the experimental data for LPL and VPL are so similar even when injected to relatively low pressure of 2 bar and temperature of 20°C . At these conditions, ammonia is in a gaseous state, and assuming fuel temperature to be equal to the ambient temperature of 20°C , the injected fluid is superheated ($p_a/p_s=0.23$) as its saturation pressure is then equal to 8.6 bars. At the pressure of 2 bar, ammonia boiling temperature is 254 K ($T_f-T_b=39$), thus sudden evaporation is expected to shorten LPL leading to its separation from VPL as predicted by models unless the spray hits the wall before that is happening. Ammonia's high latent heat of vaporization can lead to significant cooling, thus delaying the separation of LPL from VPL. However, as shown in Fig. 22 (left plot), even at elevated ambient temperatures, experimental data indicate that the spray hit the wall before complete vaporization. On the other hand, it may also happen that inside of the GDI injector, the supply pressure decreased below the saturation pressure of liquid ammonia at 293 K, and consequently encouraged the vaporization of the liquid inside of the injector and resulted in cavitation at the spray nozzle as described by Okafor et al. [43]. The phase change would require heat subtraction from the liquid resulting in its cooling, and thus, potentially ammonia could have been injected at a much lower temperature than the ambient one. The right plot in Fig. 22 shows the penetration results obtained from the simulations at different fuel temperatures. It can

be seen that when the fuel temperature was decreased to 270 K, the separation between VPL and LPL still take place. When ammonia temperature was further decreased below its boiling point to 250 K, the difference between VPL and LPL became small, and there is no more clear separation between them with LPL stabilizing at some distance from the nozzle.

It is now also worth showing the cooling effect due to ammonia vaporization for these three different temperatures of injected fuel. Fig. 23 shows the temperature distributions along the single spray plume axis and along the injector axis for selected times and the three different fuel temperatures. The initial ambient temperature for all the cases is 293 K, and the results in plots in the left column of Fig. 23 show rapid temperature decrease along the single plume axis, down to ca. 200 K. At the time of 1 ms, the temperature profiles sharply rise to the ambient temperature at the distance of ca. 60 mm, which corresponds to the penetration length. For the subsequent times, this distance move downstream correspondingly. The temperature is not that low along the injector axis, but it drops below 270 K and 250 K for the cases where the injected fuel temperature was 293 K and 270 K, respectively. Therefore, we see that the cooling effect is more substantial when the fuel was cooled down by 23 K. However, the temperature along the spray plume is indeed the coldest for the case where the fuel was cooled down below its boiling temperature at 2 bars. On the other hand, along the injector axis, the gas temperature is always higher than the liquid fuel temperature. Therefore, in this case the cooling effect on the surrounding environment is the lowest due to the lack of intense vaporization. This effect is also qualitatively presented in Fig. 24 where the temperature contours are shown at the distance of 40 mm downstream the injector. The results indicate that for the intensively vaporizing sprays where the fuel was superheated, the cooling of the surrounding environment is vital, whereas for the case with ammonia injected below its boiling temperature, the effect is much weaker and only the spray plume regions are cooled down.

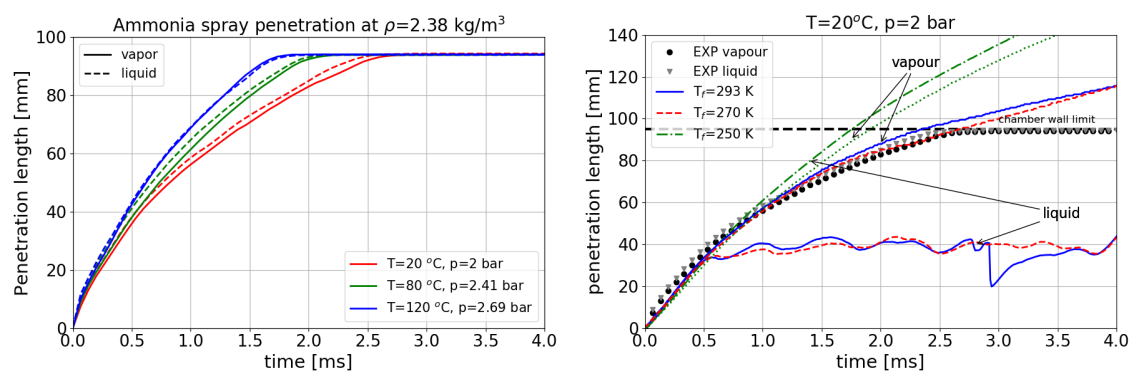


Figure 22: Experimental data of ammonia spray penetration lengths (vapour and liquid) at three different ambient temperatures and constant density $\rho=2.38 \text{ kg/m}^3$ (left plot) and comparison of experimental data at $T=20^\circ\text{C}$ and numerical results for the three different injected fuel temperatures.

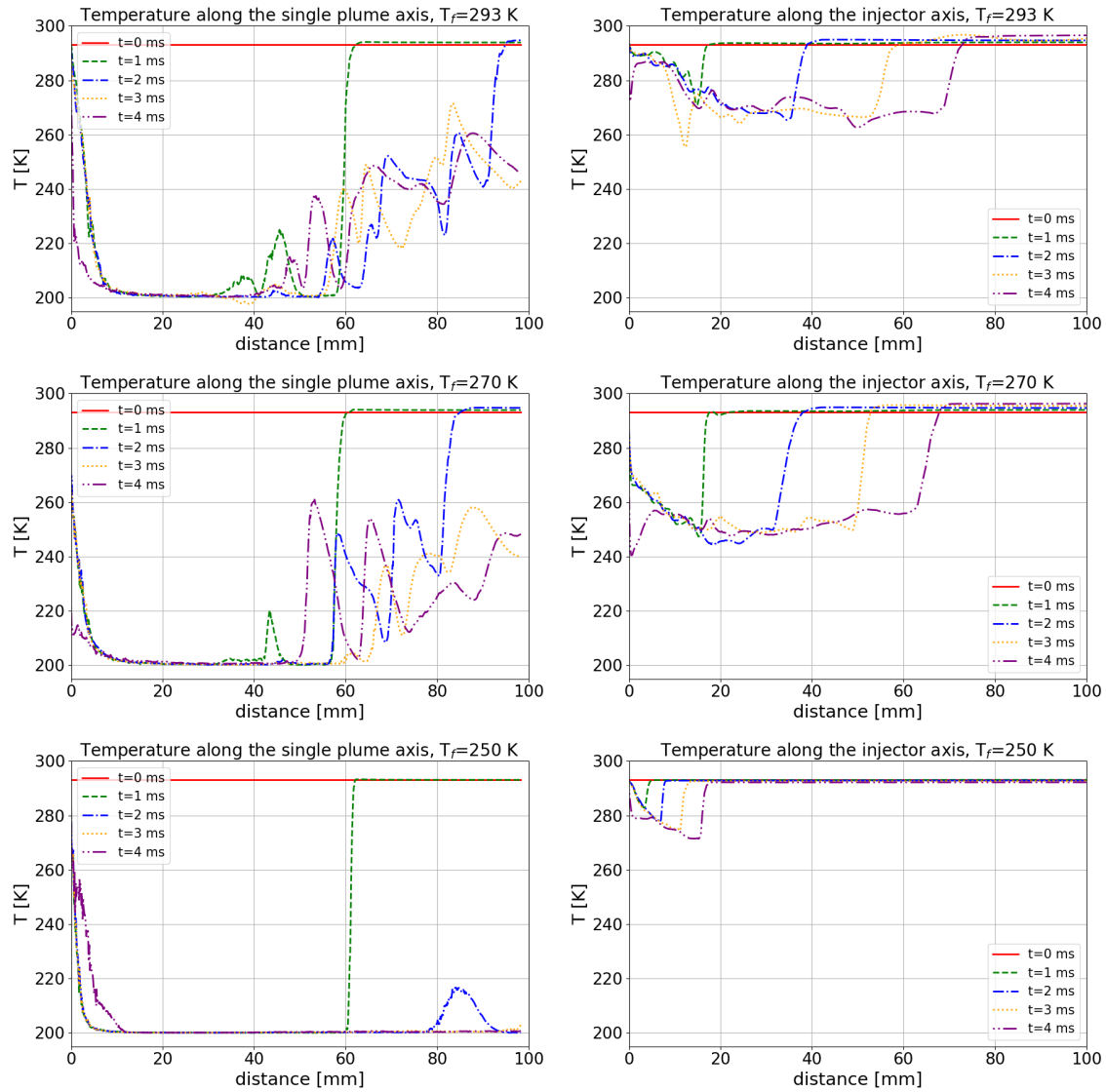


Figure 23: Temperature distributions along the single plume axis (left column) and the injector axis (right column) for the three fuel temperatures: $T_f = 293$ K (top row), $T_f = 270$ K (middle row) and $T_f = 250$ K (bottom row). Each line represents the temperature profile collected after 1 ms, 2 ms, 3 ms and 4 ms after the injection.

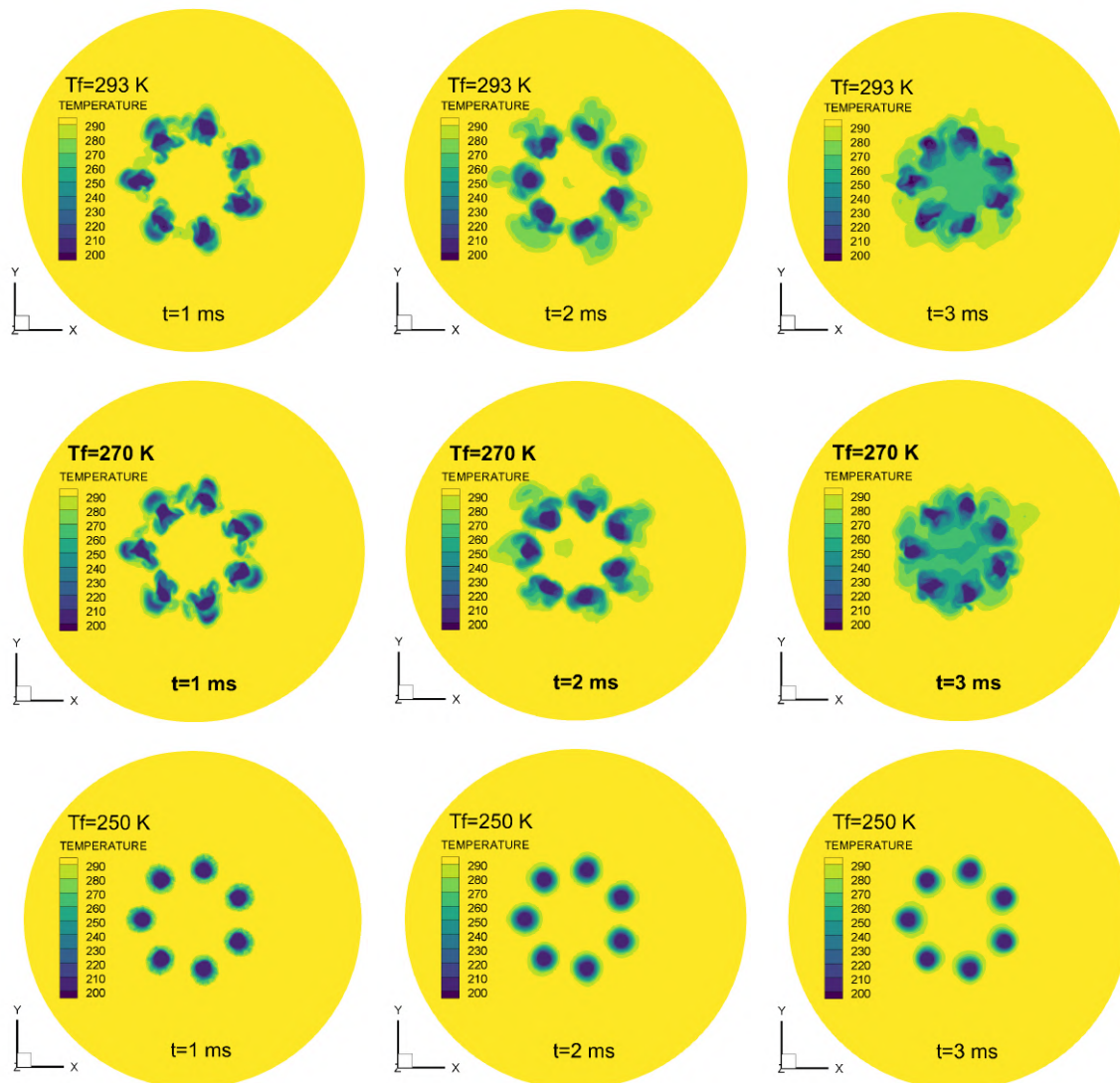


Figure 24: Temperature contour maps collected at XY plane 40 mm downstream the injector for the three different fuel temperatures ($T_f=293$ K (top row), $T_f=270$ K (middle row) and $T_f=250$ K (bottom row)) and three times after the injection.

Summary

In the first part of this study, the geometrical model of the single-cylinder Hatz engine has been prepared. Different geometrical GDI positions were considered, and the possibility of the spray wall interaction was assessed. Based on the obtained detailed geometrical data of the GDI injector and recent ammonia spray measurements, it was concluded that the spray wall interaction is not expected.

On the other hand, flash boiling was found as likely to occur during early ammonia injections. This phenomenon is a challenging part of numerical modelling. The relevant literature was reviewed, including numerical and experimental studies, which in their ma-

major part concern more typical fuels such as gasoline and alcohols. Nevertheless, the crucial models for capturing the flash boiling spray characteristics were identified and further assessed. Attention was paid mainly to the vaporization model (accounting for external flash boiling, which intensifies vaporization), spray breakup model parameters and spray angles. The numerical results were compared to the experimental data obtained from the unique and very recent study of Pelé et al. [40]. Numerically obtained vapour penetration lengths (VPLs) compared well with the experiment, however, liquid penetration lengths were not reproduced accurately.

The inconsistencies between the numerical and experimental results were discussed and followed by thermal analysis. Since there was no control over the injected fuel temperature in the experiment, it is hypothesized that the injected fuel could have been reduced due to the pressure drop inside the injector and consequent phase change and cavitation. It was also shown that ammonia vaporization is accompanied by a significant cooling effect, changing the spray characteristic and limiting flash boiling to just a part of the spray. Although fundamental aspects of direct injection of liquid ammonia are still to be explored, both experimentally and numerically, the present study has revealed the expected challenges and provided some guidelines to overcome them. At this stage in the project, it will be assumed that the injected liquid fuel temperature is equal to 20°C since it is possible to control it by heating or cooling as it was done in the experiment performed by Okafor et al. [43].

The analysis of GDI geometry and its position in the Hatz engine combustion chamber assessing the possibility of the spray-wall interaction. It was found that such a phenomenon is unlikely to happen. Nevertheless, alternative scenarios with the injector rotated and with sealed selected nozzles were provided.

The assessment of the vaporization models, spray breakup model parameters, and the effect of changed spray angles. Modifications of those models were discussed to present their effects on the spray penetration lengths to account for flash-boiling relevant for the conditions when the injected liquid ammonia is superheated.

The literature review and identification of major physical challenges that can occur during liquid ammonia spray injection. Attention was paid to the flash-boiling phenomena and the ammonia cooling effect due to the phase change.

The above findings are crucial to proceed with performing the 3D numerical analysis in the single cylinder Hatz engine. They serve as guidelines for setting an appropriate modelling approach for different operating conditions and injection timings.

3.4 0D SRM for simulating engine performance parameters

Scope of work

The primary objective of the work described in this section is to develop and verify 0D SRM-based simulation procedure capable of simulating combustion in a CI engine that is operated with direct injection of ammonia and biodiesel. This work is the first attempt to use SRM to examine such configured engine and combustion system.

The work starts from simulations conducted for pure diesel and then biodiesel. These provide basis and reference while moving towards the target application with ammonia and biodiesel that is presented subsequently.

Reference experimental data

Simulations refer to the experimental data from a single cylinder CI engine investigated in the project. The basic specification of the engine is given in Table 4. Overall, the engine was tested as port and direct injection. With respect to the used fuel, the measurements campaign started from pure diesel. Then pure biodiesel was analyzed, and finally biodiesel and ammonia. All experiments were conducted by the project partner Silesian University of Technology (SUT). and made available on the 19th of August 2022. In this section we present only basic information about the experimental engine and operating points for the completeness of the report. Details on retrofitting the engine for the dual fuel technology are beyond the scope of this milestone report. They can be found in the reports by project partners.

Table 4: Engine basic specification.

Engine type	Compression ignition
Bore (mm)	86
Stroke (mm)	70
Compression ratio (-)	16.5:1
Number of valves (-)	4
Rated power (kW @3500rpm)	6.4

The development of numerical 0D in-cylinder model was carried out in reference to the experimental data obtained at one engine speed and four different injection timings of ammonia. The start of injection (SOI) for biodiesel remained unchanged and equal -17 deg after top dead center (aTDC). The operating points are briefly summarized in Table 5.

Table 5: Engine operating points with direct ammonia and biodiesel injection.

OP	1	2	3	4
Engine speed (rpm)	1500	1500	1500	1500
IMEP (bar)	5.08	4.97	5.10	5.06
Phi (-)	0.43	0.41	0.40	0.41
AES (%)	26	26	25	29
SOI NH3 (deg aTDC)	-10	-14	-17	-20
SOI biodiesel (deg aTDC)	-17	-17	-17	-17

Results for pure diesel

Simulations of an engine fueled with pure diesel were conducted at earliest phases of the project when experimental data for model calibration were not available yet. Therefore, for these early-phase tests we adopted our in-house available data from another single cylinder engine. The main purpose of these tests was just to verify, at possible early phase of the project, the performance of the applied reaction kinetics that contained also sub-model for n-heptane that can be used as single component surrogate of a diesel fuel. The use of pure diesel (see, Fig.25) as a first test was beneficial since most of the experience in modelling and simulations with the SRM has been gained exactly based on diesel engines. The obtained simulated in-cylinder pressure and rate of heat release (RoHR) histories agree with the experimental counterparts. This good agreement was a first and preliminary step towards evaluating the performance of the reaction mechanism.

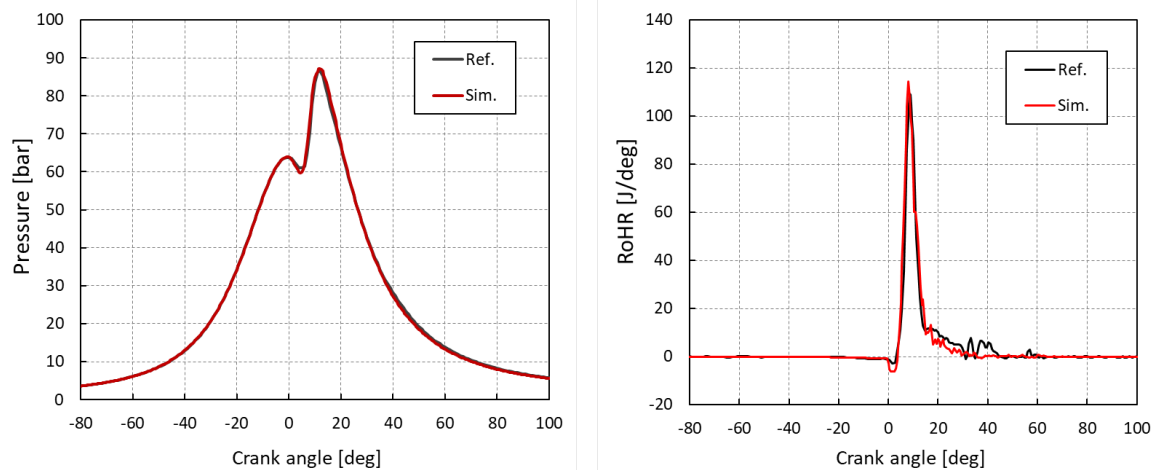


Figure 25: Simulated in-cylinder pressure and RoHR histories (Sim.) compared to the experimental counterparts (Ref.).

Results for pure biodiesel

Simulations for pure biodiesel were carried out for the engine presented in Section 4.4. They refer to four operating points presented in Table 4.4

Table 6: Engine operating points with pure biodiesel.

OP	speed	torque (Nm)	mass flow (g/s)
OP1	1500	4	0.109
OP2	1500	8	0.156
OP3	1500	12	0.207
OP4	1500	17	0.292

The SRM was set up through calibrating adjustable parameters in the zero-dimensional turbulence model developed in [7]. From the calibrated turbulence model, mixing time history is derived that is the main model parameters for the SRM. Table 7 contains calibrated model constants.

Table 7: Model constants in the calibrated $k - \epsilon$ turbulence model.

Parameter	$C_{\epsilon,1}$	$C_{\epsilon,2}$	C_{inj}	C_{τ}	$C_{k,init}$
Value	7	3	0.0063	8.11	11

In Table 7, $C_{\epsilon,1}$ and $C_{\epsilon,2}$ denote model parameters for in-cylinder flow and inflow/back squish flow, respectively. C_{inj} is the model parameter that influences the flow velocity due to fuel injection. C_{τ} is a general model parameter that enables scaling the history of mixing time, and $C_{k,init}$ is the model parameter influencing the initial turbulent kinetic energy.

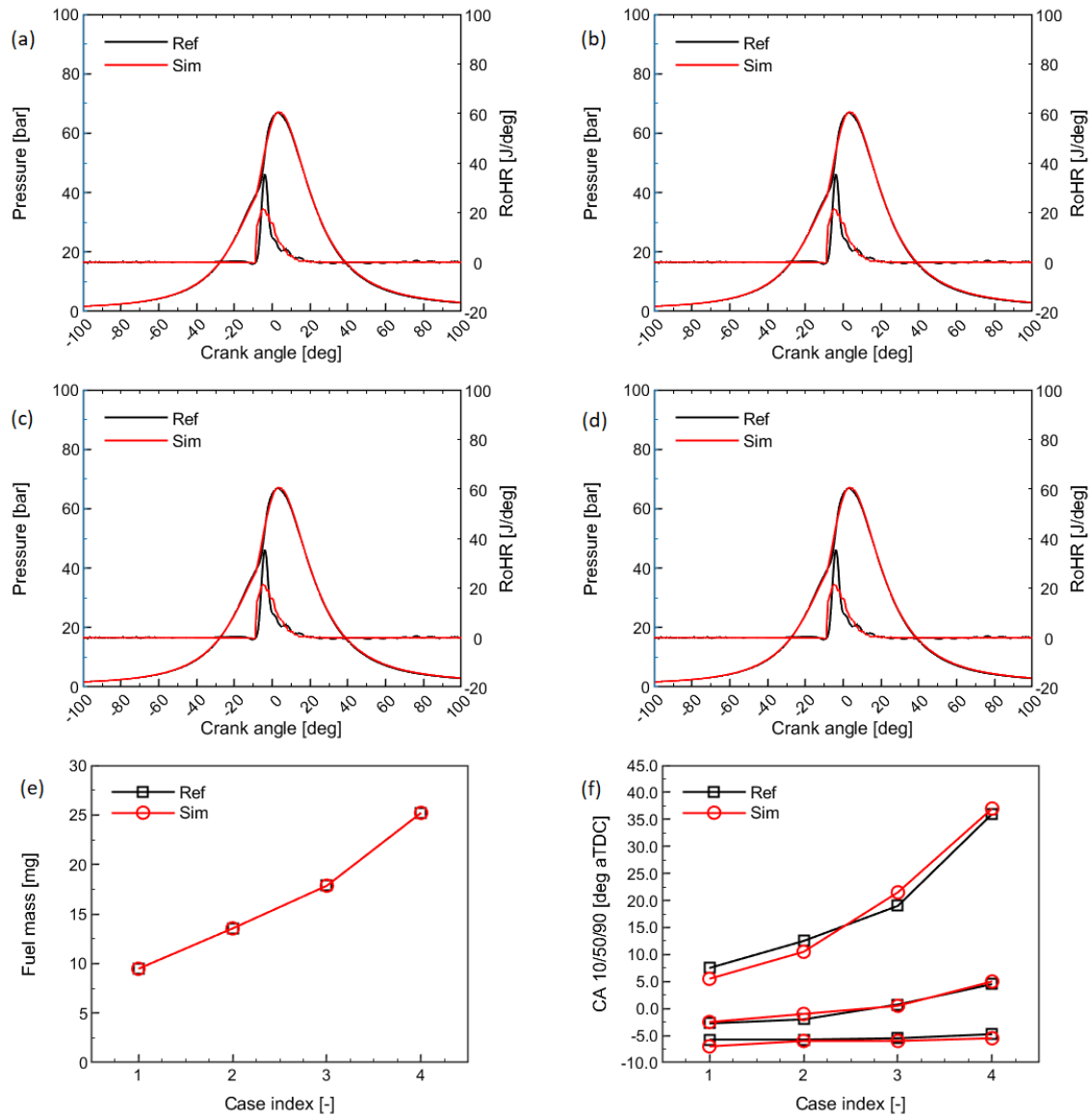


Figure 26: Simulated in-cylinder pressure and RoHR histories (a, b, c, d), fuel mass (e) and combustion progress (f) compared to the experimental counterparts for operating points in Table 4.4.

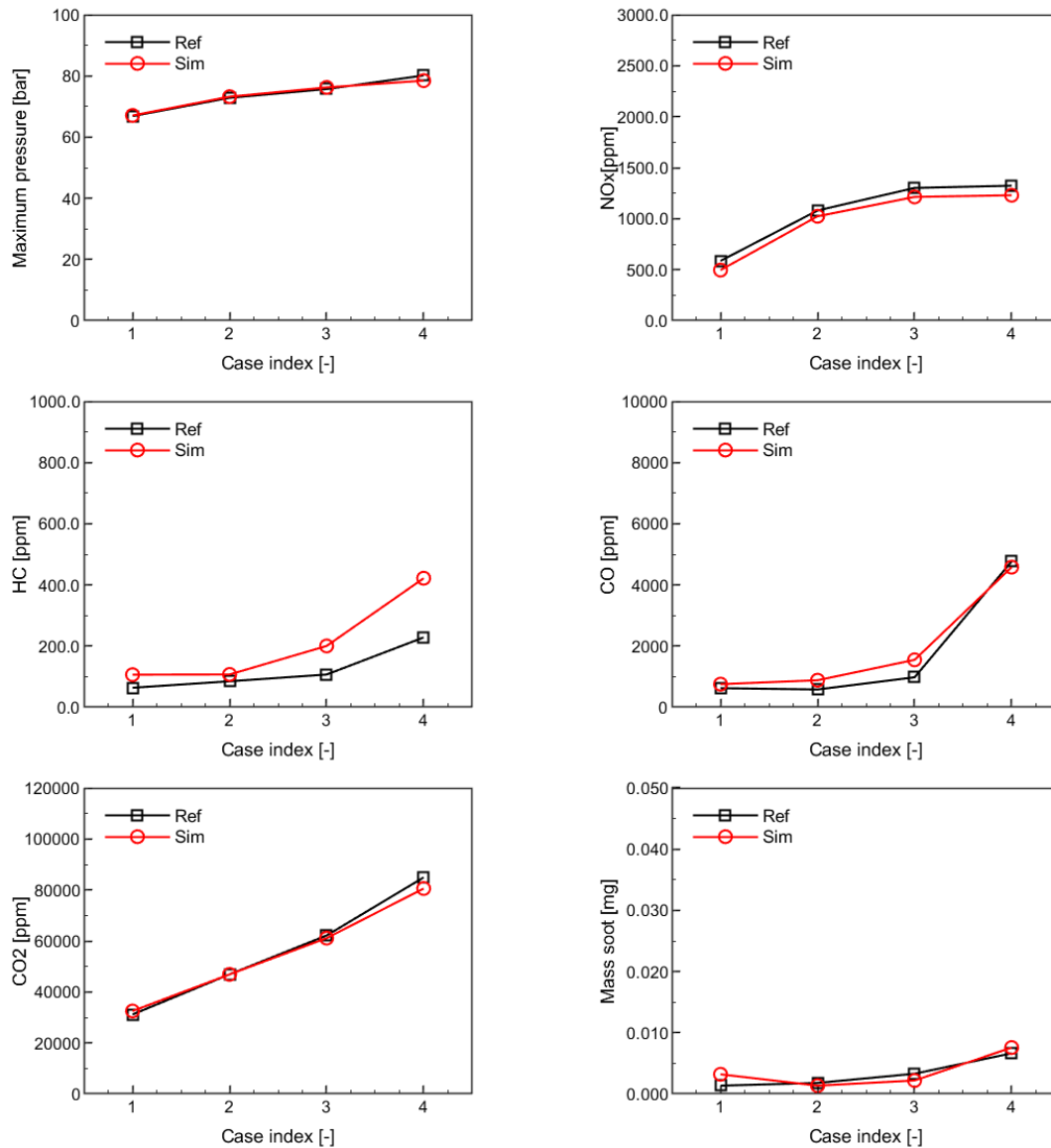


Figure 27: Simulated maximum in-cylinder pressure and selected emissions compared to the experimental counterparts for operating points in Table 4.4.

For the engine performance parameters presented in Fig. 26 and Fig. 27, and for all simulated operating points, the simulated results agree well with experimental counterparts, giving thus an indication about the qualities and capabilities of the developed reaction kinetics in simulating biodiesel fueled engine. This simulation campaign was a prerequisite to apply the developed model to simulations where besides biodiesel, ammonia is additionally injected into the combustion chamber.

Computational setup for simulating ammonia/biodiesel

To simulate performance parameters of the engine operated with ammonia and biodiesel (Table 5), the numerical procedure similar to the one presented in previous section was adopted. The inclusion of the second fuel injection rate due to presence of ammonia was the main change in the numerical model configuration when compared to simulations of pure biodiesel.

Table 8 summaries parameters of the SRM that were used through the simulations and Table 9 lists the most important parameters of the $k - \epsilon$ turbulence model. These parameters were defined during the model calibration.

Table 8: Setup of the SRM parameters.

Parameter	Value
Number of particles (-)	500
Number of cycles (-)	30
Time step (-)	0.5
Stochastic heat transfer coefficient (-)	15
Mixing model	Curl

Table 9: Model constants in the calibrated $k - \epsilon$ turbulence model.

Parameter	$C_{\epsilon,1}$	$C_{\epsilon,2}$	C_{inj}	C_{τ}	$C_{k,init}$
Value	7.0	3.0	0.0529	9.448	11

Model calibration results

• OP1

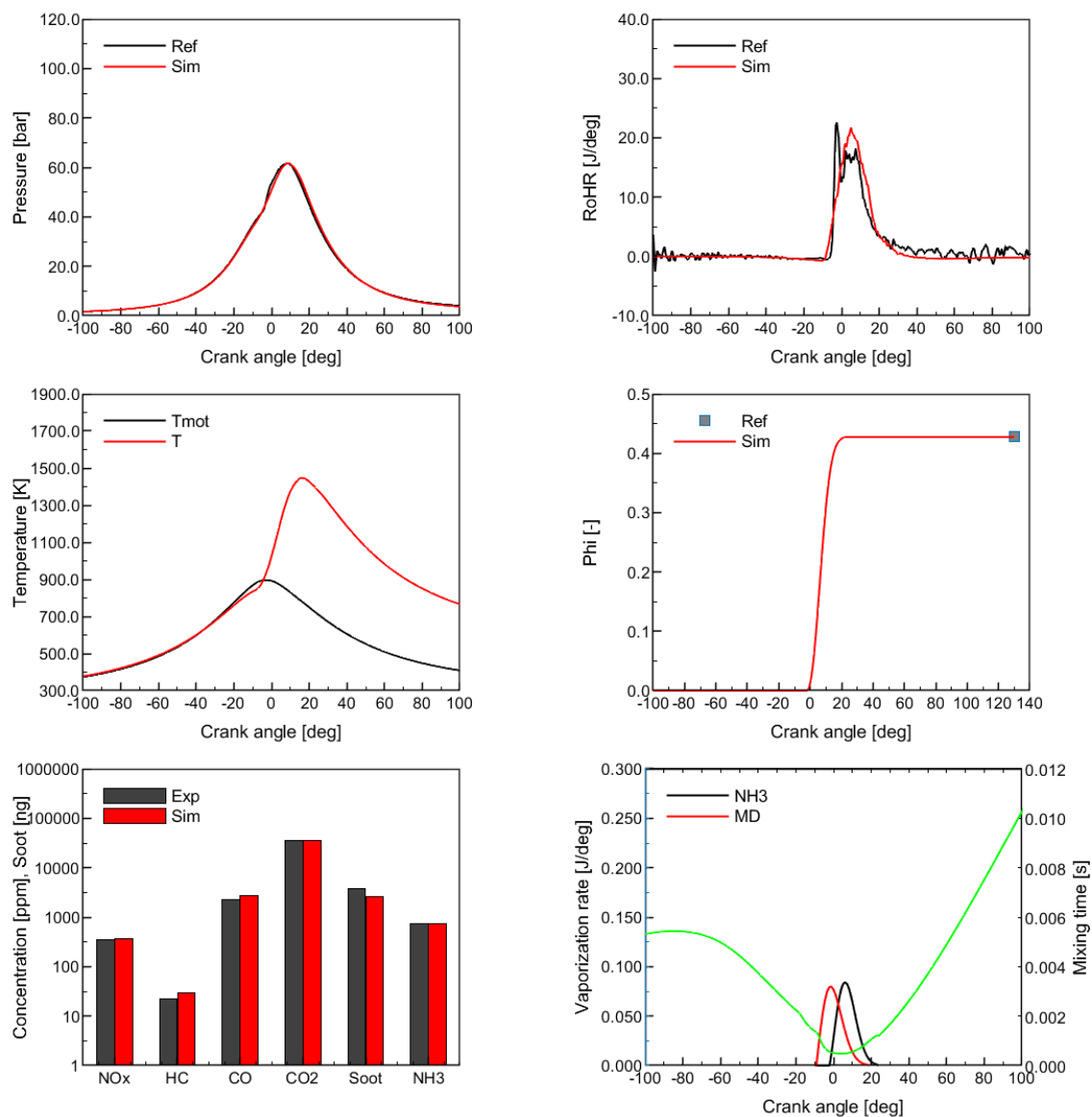


Figure 28: Selected engine in-cylinder performance parameters, exhaust emissions and operating conditions compared to their experimental counterparts for OP1.

• OP2

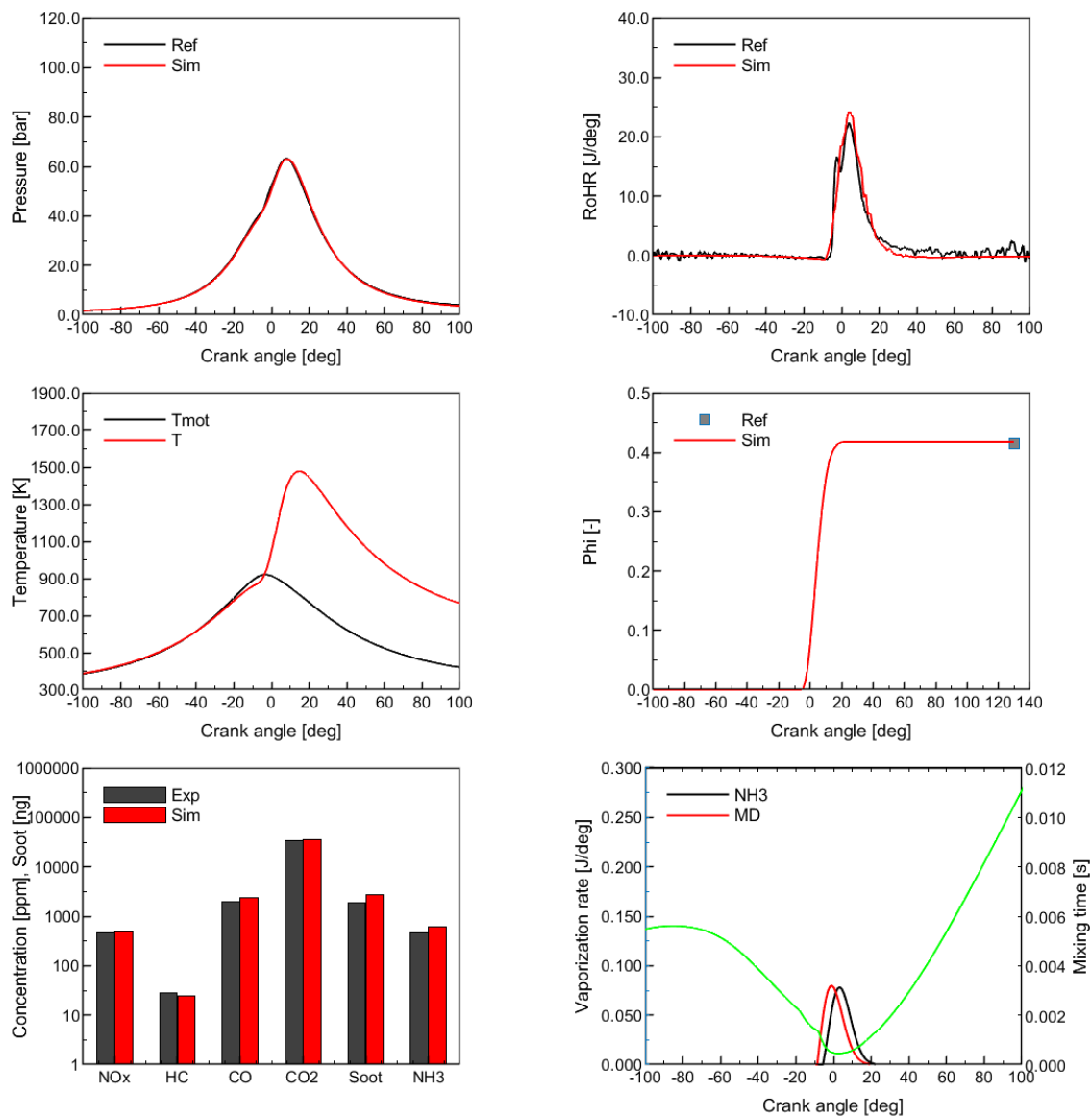


Figure 29: Selected engine in-cylinder performance parameters, exhaust emissions and operating conditions compared to their experimental counterparts for OP2.

• OP3

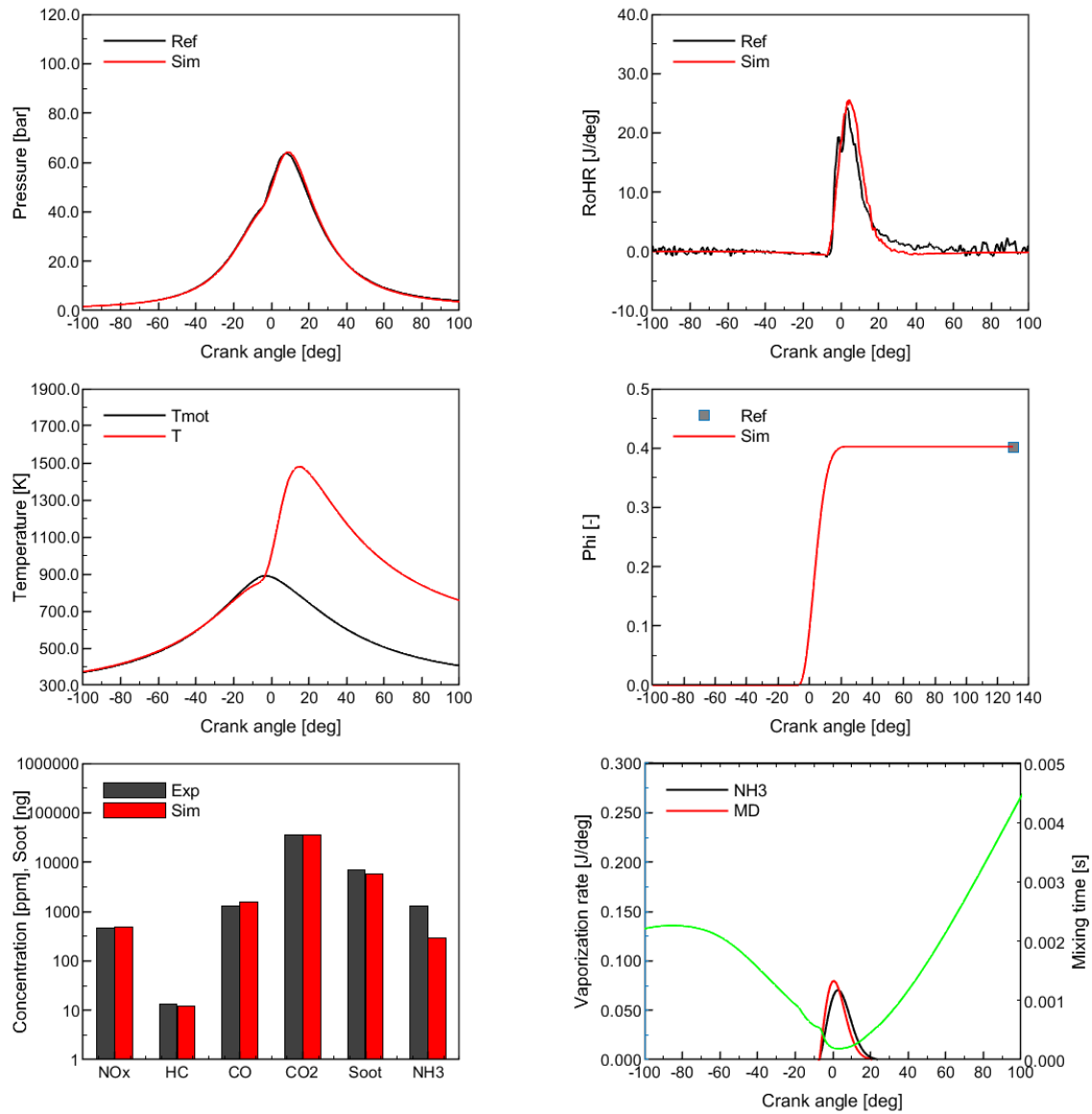


Figure 30: Selected engine in-cylinder performance parameters, exhaust emissions and operating conditions compared to their experimental counterparts for OP3.

• OP4

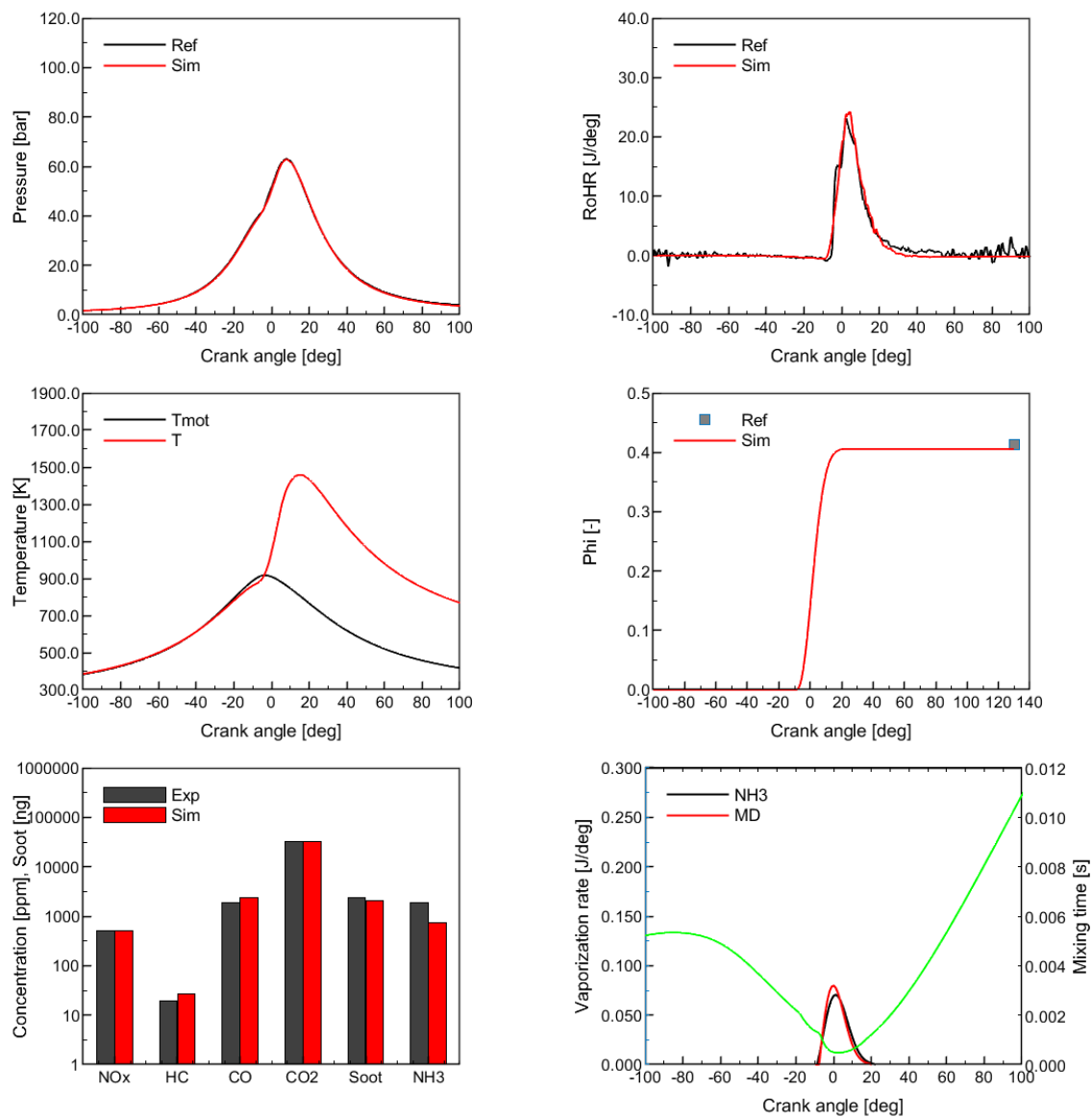


Figure 31: Selected engine in-cylinder performance parameters, exhaust emissions and operating conditions compared to their experimental counterparts for OP4.

- Global performance parameters

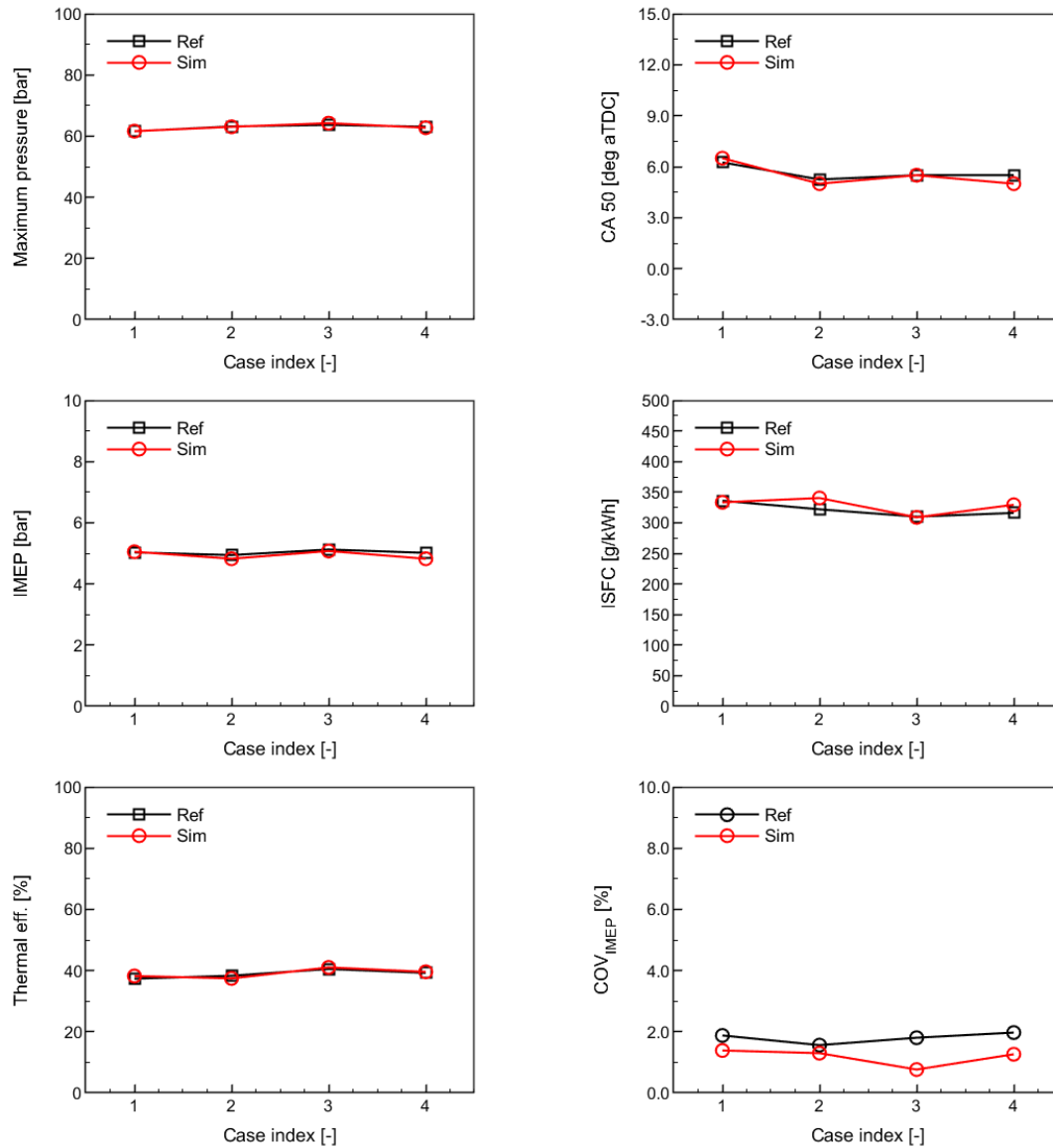


Figure 32: Selected global engine performance parameters for OP1-4 from Table 4.4.

Summary

Overall, for all 4 operating points available for the SRM calibration, good agreement between simulated and measured data is noted. Simulated results were obtained with one set of model constants in the $k - \epsilon$ turbulence model. The simulated crank angle dependent pressure and RoHR histories agree well with the reference counterparts. The reference maximum values of in-cylinder pressure and RoHR are also well matched by simulations. For OP1 (Figure 28) the reference RoHR exhibits two peaks that are not captured by simulations. Consequently, the simulated in-cylinder pressure history is slightly under-predicted around 0 deg aTDC that corresponds to the first peak in the RoHR history. However, in general, such an agreement between the measured and the predicted results can be considered as high quality for 0D models. Besides, it should be noted noise character of the reference RoHR history that is derived from the measured pressure data. It is expected that the noise contributes partially to such a well seen two peaks in the reference RoHR history.

As to the emission results, the predicted by the model NO_x , HC, CO, CO_2 , soot and NH_3 agree reasonably well with the measured experimental counterparts. Ammonia emission is accurately predicted for OP1 and OP2 but less accurately for OP3 and OP4, in which combustion results in more ammonia in the exhaust. At OP3 the SOI of ammonia equals the SOI of biodiesel and at OP4 ammonia is injected after biodiesel. At the time of simulations of these two operating points, no supporting 3D CFD results were available that could indicate about the sources for higher ammonia emission. Hence, we have decided not to perform any tuning or scaling of the 0D numerical model results until the increase of exhaust ammonia for these particular points is better understood.

Good agreement between simulated and measured crank angle depended quantities resulted in good agreement for global engine parameters such as IMEP, ISFC (indicative specific fuel consumption), maximum in-cylinder pressure, combustion center (CA_{50}) and thermal efficiency.

4 Simulation results

4.1 3D CFD modelling of ammonia injection

Scope of work

The description of the 3D CFD numerical model of a single-cylinder Hatz engine constituting a baseline configuration of the injection system used in further developments is presented. Detailed description accompanied by an explanation of selected modelling approaches justified in Sec 3.3 is followed by the presentation of the results for different operating conditions. The model results provide insight into the flow structures inside the cylinder and local phenomena, such as spray formation and vaporization, ignition characteristics.

First, a detailed description of the engine geometry and its preparation for the 3D CFD modelling is presented. Then, the numerical grid study, thermodynamic conditions assessment, and their impact on the selection of sub-models to simulate flash boiling spray are discussed. Subsequently, the presented results consider three cases with different starts of ammonia injection. At first, the mean turbulence integral time scale is considered representative of a mixing time scale, which later on can support setting up the 0D model. Next, the ammonia cooling effect is investigated and followed by an ammonia evaporation assessment. The last results section focuses on presenting selected data to assess the mixture formation and calibrate the position of the pilot fuel nozzles.

Engine description

Full description of the single cylinder CI engine and the details of the experimental rig were given in the M1.1 and D.1.1 reports of the ACTIVATE project. Here only a brief summary and the most relevant data are given. It is the Hatz engine with a type number 1B30 with 347 cm³ of displacement volume, max. torque of 16.2 Nm and power from 2.3 to 5.0 kW. Selected characteristic parameters of the engine are provided in Table 10. Figure 33 shows the picture of the engine and the geometry of the combustion chamber, including piston, inlet and exhaust ports.

Parameter	Unit
Bore	80 mm
Stroke	69 mm
Displacement	0.347 l
Connecting rod length	114.5 mm
Compression ratio (CR)	21.5
Inlet valve closure (IVC)	-100 CAD
Exhaust valve opening (EVO)	100 CAD

Table 10: Selected characteristic Hatz 1B30 engine data



Figure 33: Hatz engine picture (left) and the geometry of the combustion chamber (right), including piston, inlet and exhaust ports.

Geometry preparation

The first step in building the 3D CFD model was the Hatz engine geometry preparation. In order to obtain the geometrical data, the engine was disassembled, and its parts were sent for 3D scanning (see Fig.34). The separate scans were performed for the engine head, piston, and valves. Some geometry elements had defects due to light reflections and limited optical access to some inner parts of the engine head, such as inlet and exhaust ports. Those defects were corrected, and the geometry was completed with the use of Converge Studio software, and Fig. 35 schematically presents the process.

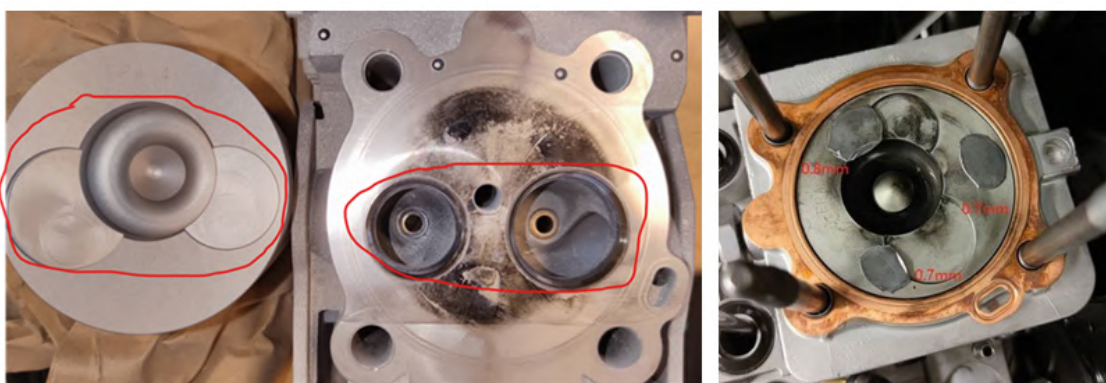


Figure 34: The geometry elements disassembled for the 3D scanning and measurements.

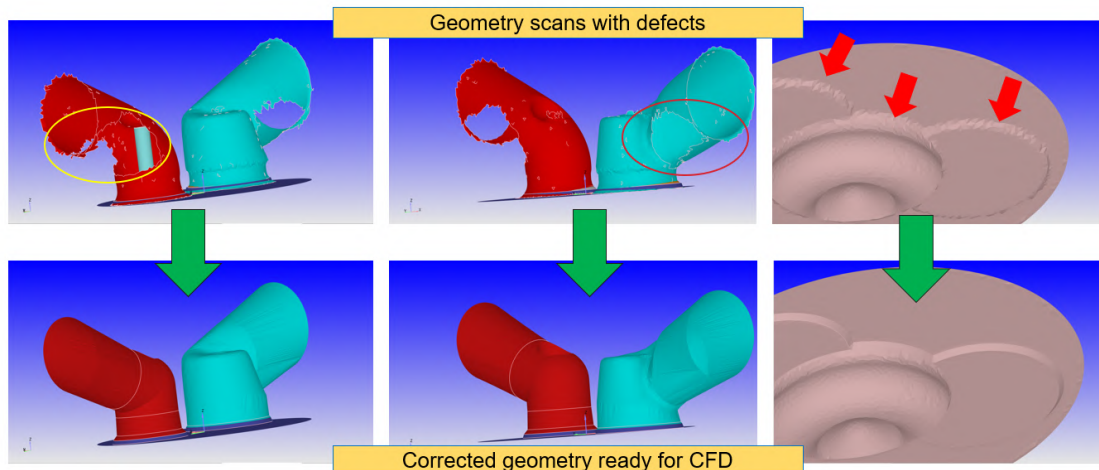


Figure 35: The geometry STL files with defects (first row) and the same geometry parts corrected, ready for the use in simulations (second row).

Numerical grid

The CONVERGE code has the capability of employing autonomous grid generation to model complex geometries. In contrast to many other codes, an engine geometry motion is handled by creating a new mesh at each time-step instead of employing the moving mesh approach. Additionally, an adaptive mesh refinement (AMR) algorithm assists in improving or adjusting the grid size in the regions where it is needed based on predefined refinement criteria. Such an algorithm is advantageous when solving the flow during valve opening or closing and fuel injection. AMR and fixed embedding (predefined grid refinement in the selected region) and user-defined grid control parameters are essential tools for designing appropriate numerical mesh for complex and moving geometry. Nevertheless, these tools have to be employed carefully in order to efficiently improve the predictions in dynamically changing transient flow by refining only the necessary regions. Otherwise, the usage of too strict AMR algorithms adopted in too many regions and less important periods of simulations can lead to an unreasonable increase in CPU time.

The numerical grid is perfectly orthogonal, and the cells close to the boundaries are created with a cut-cell Cartesian grid generation algorithm that allows for the reproduction of the complex surfaces. In this work, the base grid cell size was set to 2 mm and the sizes of each subsequent scale of embedding/refinement are shown in Table 11. Refinement criteria for AMR were based on sub-grid scale velocity of 1 m/s using 3 and 4 levels of embedding. However, an increase in one more level of embedding leads to a significant increase in the number of cells and CPU time but causes a minimal difference in the predicted results. Therefore we have applied 3 levels of AMR with 2 mm base grids based on our previous experience with engine modelling, and detailed grid dependency studies [13]. Moreover, according to Senecal et al. [25] and Xue et al. [26] who have performed non-reacting vaporizing spray simulations using CONVERGE code, the cell size of 0.25 mm in RANS simulations is small enough to provide correct liquid penetration length and thus is often set as the recommended value. Additionally, when it comes to the Lagrangian approach for

spray simulations, the finer the cells, the more parcels have to be injected, and the cell size of 0.25 mm requires injection of over 512 000 parcels. Additionally, attention was paid to activate the AMR algorithm and fixed embedding during crucial engine events (compression close to TDC, closing and opening the valves). Figure 36 shows selected 2D slices with the resulting mesh and velocity magnitude as a background contour map for the three different positions of the crankshaft. Figure 37 presents positions of the GDI (left) and diesel (right) injectors, separately from the same view. Fixed embedding is applied with the refinement scale of 3 in the injectors regions to cover the cone shape of the expected spray plumes.

refinement scale	cell size [mm]
0 (base)	2
1	1
2	0.5
3	0.25
4	0.125

Table 11: AMR and fixed embedding scales and corresponding cell size.

Thermodynamic conditions

The first Hatz engine simulation runs concerned motored conditions at a speed of 2000 rpm. The simulations started with intake stroke at -360 CAD with the initial in-cylinder gas temperature of 300 K and at atmospheric pressure. Intake pressure and temperature were 1.3 bar and 400 K, respectively. Figure 38 shows the pressure trace and the maximum in-cylinder temperature between the intake valve closure at -100 CAD and exhaust valve opening at 100 CAD. Ammonia injection timing is an element of the injection strategy that has to be determined in the ACTIVATE project. Depending on the selected injection time, the liquid ammonia will enter the atmosphere at very different thermodynamic conditions, and as discussed in M3.1, the flash-boiling phenomena can occur.

Ammonia vapour pressure is presented in Fig. 39 in the $p - T$ plot with a solid black line. The color line shows the pressure and the temperature from Fig. 38 at the same crankshaft positions where the crank angles are marked with color (see the color legend). Blue and red dashed lines indicate the fuel temperature of 293 K and 363 K (90°C), respectively. From this, we can conclude that when the fuel temperature is 293 K, its saturation pressure is 8.6 bar, which is achieved in the cylinder during the compression stroke at 45.5 CAD before TDC. After that time, ambient pressure is higher than the saturation pressure, thus the ratio p_a/p_s is larger than one. Thus the injected ammonia is superheated only before 45.5 CAD when the flash boiling can take place. If during the operation engine gets heated, the fuel temperature can also rise to approximately 363 K (90°C). Under such conditions, flash boiling can take place for the ammonia injections until 9.8 CAD before TDC.

Ammonia injection

The injection time of the liquid ammonia directly into the engine was not decided a priori, but it is to be determined throughout the project. However, we expect to find the optimal

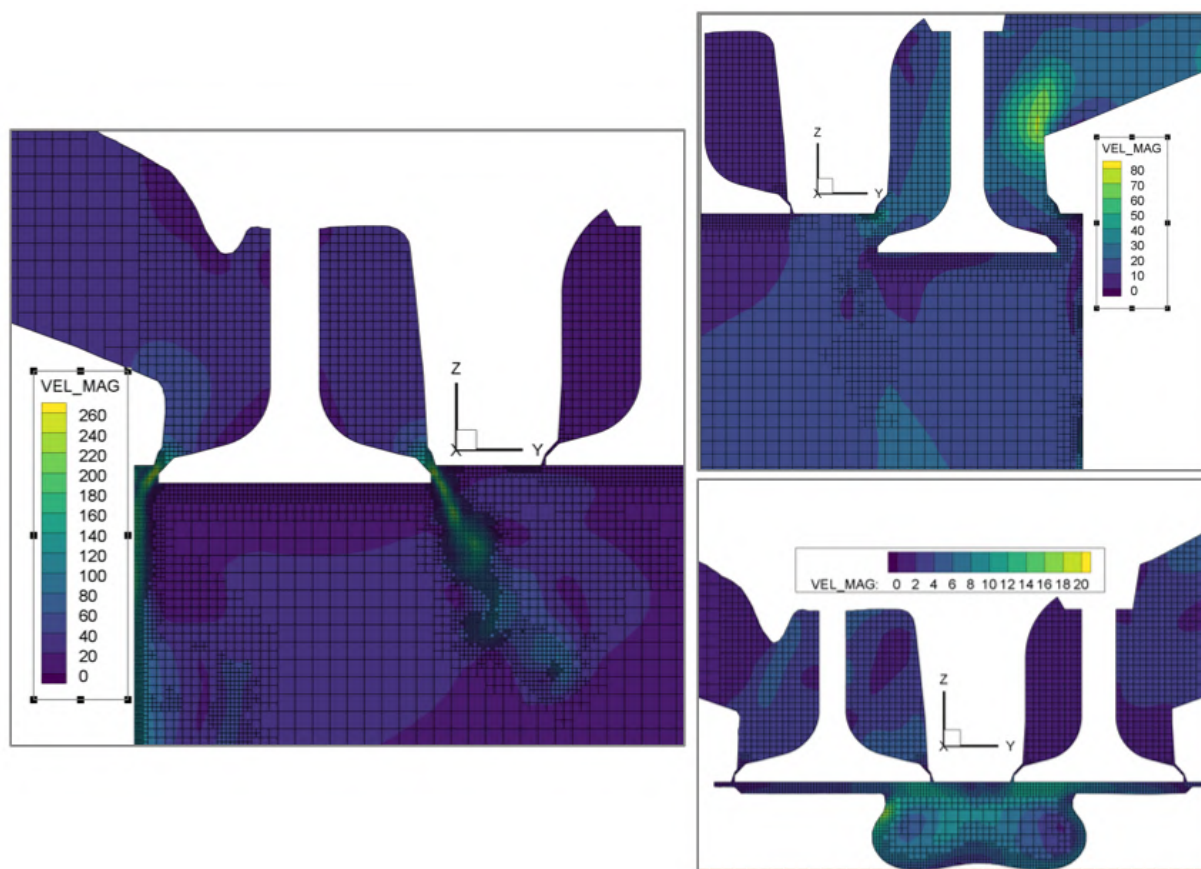


Figure 36: Selected 2D slices with the resulting mesh and velocity magnitude as a background contour map for the three different positions of the crankshaft. Left picture presents intake valve closing, right top shows exhaust valve opening and bottom right presents top dead center position.

choice between the inlet valve closure at -100 CAD and the top dead center. Diesel injection is foreseen to promote ammonia injection and will take place at -15 CAD. Therefore ammonia

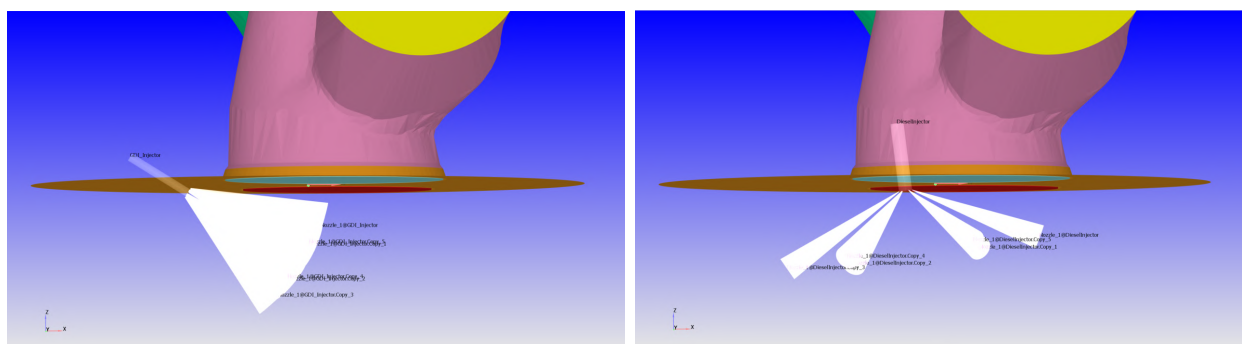


Figure 37: Positions of the GDI (left) and diesel (right) injectors. The view from the intake port side (colored with a pink).

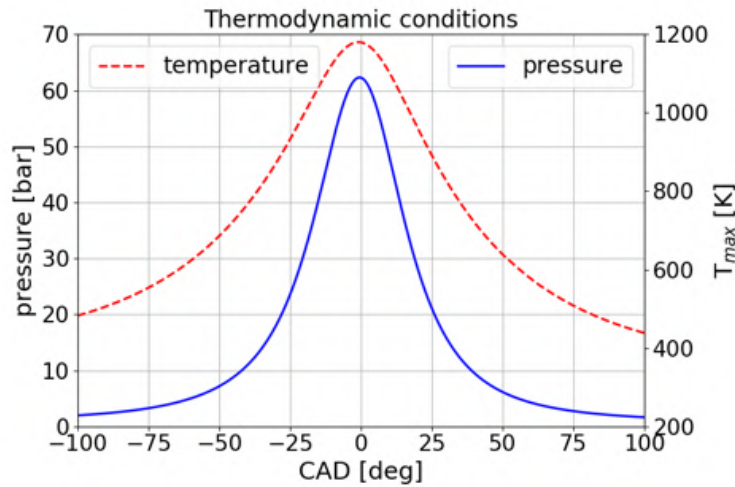


Figure 38: The pressure trace and the maximum in-cylinder temperature between the intake valve closure at -100 CAD and exhaust valve opening at 100 CAD

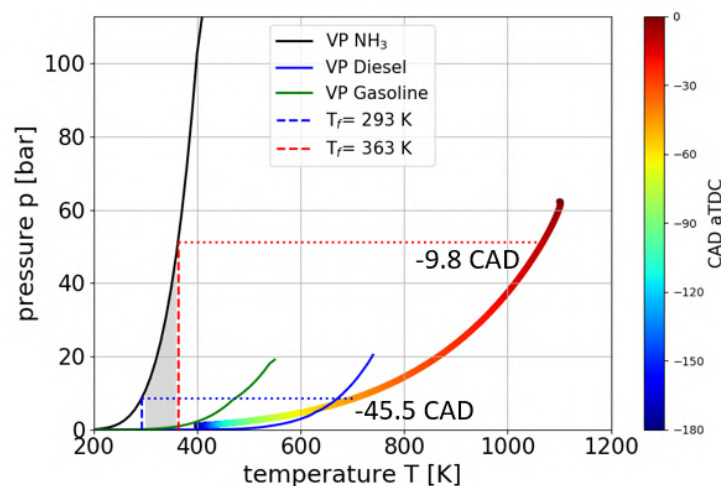


Figure 39: Ammonia vapour pressure (black solid line) and in-cylinder thermodynamic conditions from -180 CAD to TDC (denoted by colors). The numbers indicate at which crank angle in-cylinder pressure equals the saturation pressure of ammonia at two different fuel temperatures.

should be injected before that. Early injections provide enough time for good mixing of the fuel and air, whereas late injections can lead to ammonia and diesel spray interactions. Additionally, the ammonia cooling effect may influence the flame stability and the overall combustion process, which is to be explored.

In this first modelling study, the goal is to assess three different injection timings. They are selected to cover several degrees of superheat, from flash boiling to non-flashing, and can be named as early (-60 CAD), moderate (-40 CAD), and late (-20 CAD) injection with the diesel spray interaction. At these injection timings the superheat degree p_a/p_s for the fuel temperature $T_f = 293$ K is 0.58, 1.27 and 3.6, respectively as shown in Fig. 40. Additionally,

two other lines show p_a/p_s ratio for different crankshaft positions when the fuel is 20 K colder or warmer to present how the fuel temperature can affect the flash boiling conditions. For example, if the injected ammonia is cooled due to the phase change inside the injector as discussed in M3.1, the p_a/p_s ratio increases, and the flash boiling is less likely to occur. On the contrary, if the fuel is heated during the engine operation, p_a/p_s ratio decreases, and flash boiling may also occur for the late injections. However, as shown in the report M3.1, even if the injected fuel is warm, strong cooling of the surrounding takes place during its vaporization, which may additionally limit the flash boiling.

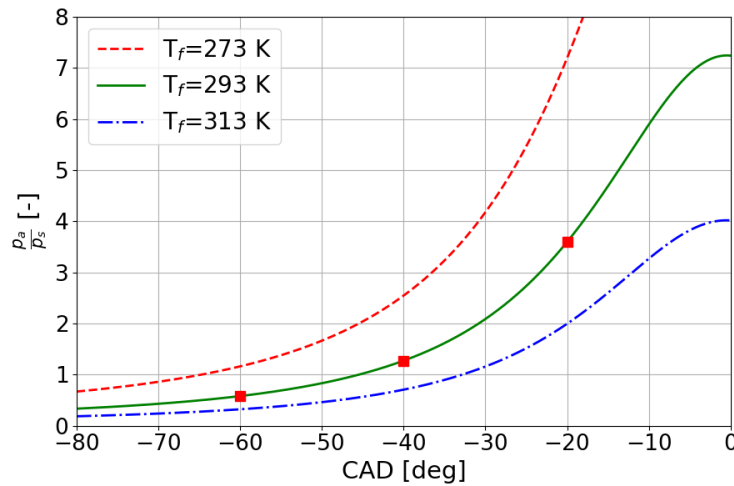


Figure 40: Superheat degree as p_a/p_s ratio as a function of crankshaft position for the three different fuel temperatures. Red symbols denote conditions during selected injection timings.

Nevertheless, the goal here is to assess the given conditions and select an appropriate modelling approach with the findings presented in the M3.1 report. Only the case with injection at -60 CAD is regarded as flash boiling, whereas the other two are assumed to be non-flashing. Consequently, only the early injection case employed the enhanced vaporization model of Price et al. [42], as well as modified RT breakup model parameters to advance a breakup process as mentioned in the M3.1 report. Additionally, based on the ammonia spray measurements of Pelé et al. [40] discussed in M3.1 report, it is possible to prescribe spray angles varying continuously as a function of superheat degree p_a/p_s . Figure 41 presents measured spray angles by Pelé et al. [40] and estimated full spray angle for the GDI injector used in the present work. As discussed in M3.1, the minimum spray angle at half of the penetration length measured by Pelé et al. [40] was 48° which corresponded to the double of the drill angle of their injector in the respective plane. The double of the drill angle of the current GDI injector is 48° and is assumed to be equal to the minimum full spray angle occurring for $p_a/p_s \geq 2.9$. As indicated by the experimental data, lower p_a/p_s ratios led to wider sprays. Therefore, the full spray angle in the present work was estimated using the proportional increase observed in the experiment with respect to the minimum full spray angle (double of the drill angle) and is denoted with a solid black line in Fig. 41. In a multi-hole injector, the full spray angle is calculated as the sum of spray plume cone angle and double angle of the spray plume direction. Therefore, the two angles must be specified

to assign the full spray angle. In the work of Duronio et al. [22] a separate set of angles was used for the standard case and different for a flash boiling case. For the cases with $p_a/p_s \geq 1$ we have adopted the same ratio of plume direction angle to the plume cone angle as in the standard case (37/30) and for $p_a/p_s < 1$ the ratio as in the flash boiling case (19/24). The resulting angles are shown with dotted-dashed blue and green lines for plume direction and plume cone angle, respectively. The summary of the numerical setting for the three cases with different injection timings is given in Table 13.

SOI	-60 CAD	-40 CAD	-20 CAD
p_a/p_s	0.58	1.27	3.6
vaporization	Frossling + Price (flashing)	Frossling (non-flashing)	Frossling (non-flashing)
KH-RT breakup	GDI flashing	GDI non-flashing	GDI non-flashing
Angles	cone: 19.74° direction: 15.63° full: 51°	cone: 16.587° direction: 20.46° full: 57.5°	cone: 10.96° direction: 13.52° full: 38°

Table 12: Summary of the modelling setup for different injection timings.

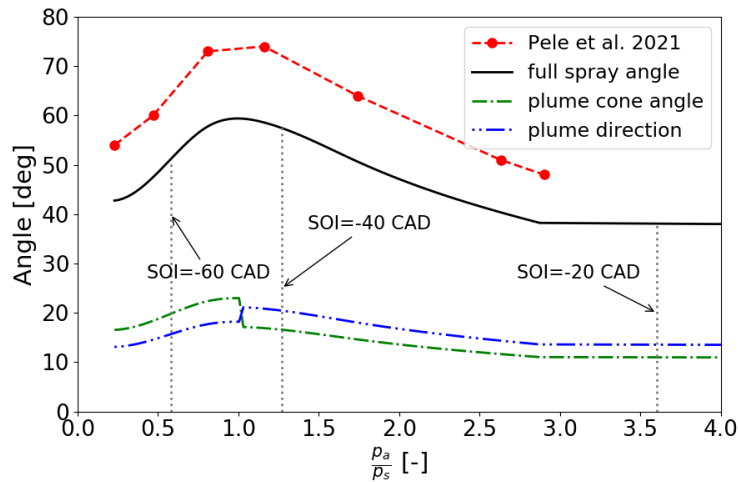


Figure 41: Spray angles as a function of superheat degree. Red symbols with dashed line represent experimental data [40] and black solid lines stands for estimated full spray angle for the GDI injector used in the present work. Dotted-dashed blue and green lines denote plume direction and plume cone angle.

To express the ammonia fraction in dual fuel injection mode we have adopted formulation of heat fraction of ammonia after Okafor et al.

$$E_{NH_3} = \frac{Y_{NH_3} LHV_{NH_3}}{Y_{NH_3} LHV_{NH_3} + Y_{diesel} LHV_{diesel}}, \quad (4)$$

where Y_i stands for mass fraction and LHV_i is the lower heating value (18.6 MJ/kg and 45.5 MJ/kg for ammonia and diesel, respectively). Reiter and Kong [46] have studied combustion of port-injected gaseous ammonia in compression ignition engine using dual ammonia-diesel fuel. They have demonstrated that it is possible to burn ammonia in a very wide range of energy contribution up to 95%. However, too low or too high ammonia concentrations negatively influence exhaust emissions (NO_x, soot, HC, CO ammonia slip) or overall fuel efficiency. They have concluded that the favorable operating range in their dual-fuel approach requires 40–60% diesel fuel energy. Therefore, in the present numerical study, it is assumed that adaptation of 50-50% ammonia/diesel by energy basis is a good starting point. Such proportions correspond to 71% of ammonia and 29% of diesel by mass. It results in the injection of 15 mg of ammonia and 6 mg of diesel per cycle for the selected operating point. Based on the available data duration of ammonia injection was estimated to 13.334 CAD and diesel to 4.28 CAD when the engine running at a speed of 2000 rpm.

	diesel	ammonia
energy fraction	0.5	0.5
mass fraction	0.29	0.71
mass per injection [mg]	6	15
injection duration [CAD]	4.28	13.334

Table 13: Diesel and ammonia injection details.

Mixing time

The mixing time scale τ is an important parameter to 0D combustion models used for engine simulations such as Stochastic Reactor Model (SRM) [4], which is going to be employed in further research in ACTIVATE project. It is defined as a fraction of integral time scale defined as k/ϵ multiplied by a factor C_{mix} . Here C_{mix} was set to 0.5. Figure 42 shows mixing time scale τ averaged over the volume of the engine cylinder for three different values of ammonia SOI as a function of crankshaft position. The characteristic sharp drop in the time scale value is observed shortly after the fuel injection, which indicates intensified mixing process. In the considered case, a relatively long ammonia injection duration causes the mixing time profile to not return to the values, which would be observed in case of the absence of the injection. As a result, we can see that the mixing time scale drop began from different values for each SOI case during the diesel fuel injection. However, the minimum mixing time values observed during each injection establish at the same value of ca. 0.04-0.05 ms for ammonia injections and ca. 0.01 ms for diesel injections. During the expansion, τ is nearly identical for all the three SOIs.

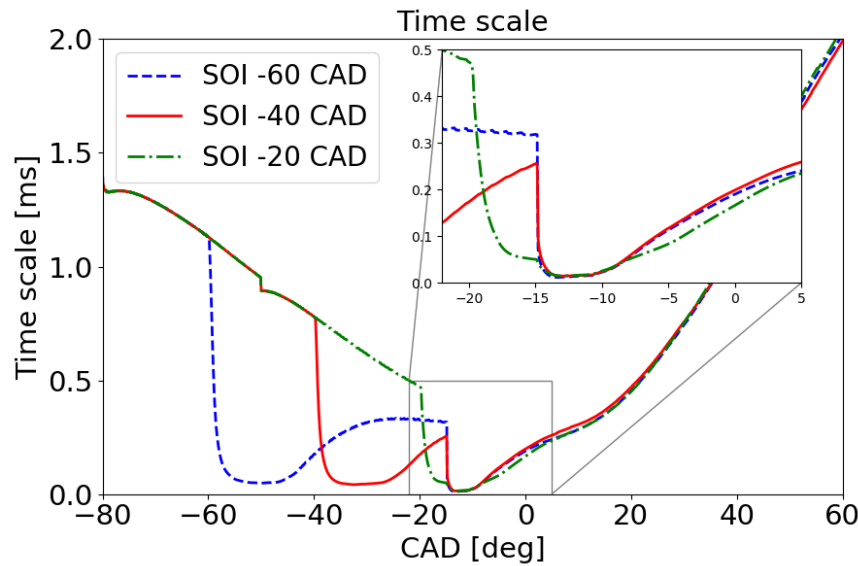


Figure 42: The mixing time scale average value over the combustion chamber volume for the three ammonia injection timings. Zoom inset shows period of diesel fuel injection.

Cooling effect

Ammonia has a high latent heat of vaporization of 1370 kJ/kg, and as pointed out by Lesmana et al. [47], one of the challenges in using ammonia as a fuel injected as a liquid is its cooling effect. Significant heat absorption is present during vaporization, which consequently leads to a strong decrease in temperature. Figure 43 shows the influence of ammonia injection on minimum, maximum, and mean cylinder temperature for the different start of injection times. The start of injection is indicated by a sudden drop in the lowest observed temperature in any location (computational cell) in the cylinder due to ammonia evaporation. For the early and moderate injection times, diesel injection is also visible in the minimum temperature profile. Differences in maximum temperature start to be visible closer to TDC when the in-cylinder gas is mixed more homogeneously. Ammonia injection leads to a 40-60 K drop in the mean temperature shortly after the injection, and at TDC, the decrease is around 120 K. Correspondingly the maximum pressure is lower by 5 bars when the ammonia is injected.

It is worth pointing out that for the late ammonia injection, the pilot diesel fuel dose enters the combustion chamber when the mean gas temperature is the highest. However, at that time, due to overlapping injections and ammonia evaporation, the mixture is not homogeneous, and cold regions exist. Nevertheless, as shown in Fig. 44 (second and fourth plot in the third column) the two liquid sprays do not interact, and the ignition may not be affected by these cold spots. Figures 44-46 show parcels, temperature, and ammonia mass fraction contours at selected YZ and YX cross-sections for the three injection timings (columns) and 4 CAD, 8 CAD and 12 CAD after ammonia injection and 4 CAD after diesel injection (rows). Parcels in Fig. 44 are colored by droplets temperature, and it can be noticed that during early injection, they remain cold until the spray hits the cylinder bowl. For early injection case, the number of parcels is visibly much lower than in the case of the

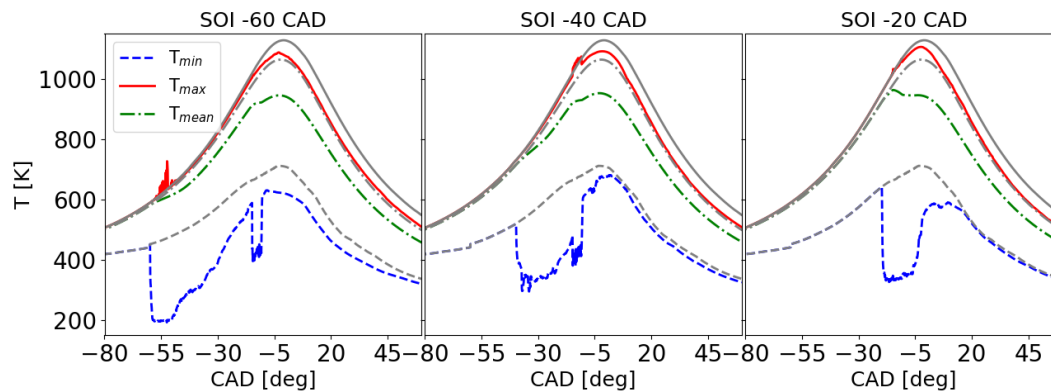


Figure 43: In-cylinder temperatures: maximum (red solid line), minimum (blue dashed line) and mean (green dashed dotted line) at three different ammonia injection timings -60 CAD, -40 CAD and -20 CAD compared to the temperatures history at motored conditions without fuel injections (respective gray lines).

two later injections, which is related to the fact that only the first case is regarded as flash-boiling with enhanced evaporation driven by heat flux from liquid droplet to its surface and advanced breakup occurrence. The moderate and late injections occur when the liquid fuel is not superheated and undergo a normal vaporization process where the heat is provided from the surrounding gas. Obviously, for later injections, warmer surrounding gas heats the liquid fuel much quicker. Figure 45 shows the temperature contours with a similar pattern during the fuel injection as presented in M3.1 report. Spray plums significantly cool down the surrounding gas what is especially visible for the early injection case where the flash boiling occurs. Noticeably different spray widths for different SOI are the outcome of the assigned conditions described in Sec. 4.1. Figure 46 shows ammonia mass fraction contours that correspond well to the temperature field. The correlation of low-temperature regions with ammonia concentrations indicates a featured problem of ammonia ignition without pilot fuel injection or another type of ignition promotion.

Ammonia evaporation

Ammonia at atmospheric pressures and in-cylinder conditions should naturally occur at a gaseous state. However, due to its high latent heat of vaporization and thus strong cooling effect described above can prolong its evaporation process. It has also been presented in the ACTIVATE milestone report M3.1 that the ammonia sprays cool down the surrounding gas dramatically and, dependently on the initial fuel temperature, can remain in the liquid phase relatively long. Therefore, it is of interest to quantify ammonia evaporation at different injection timings.

As it is visible in Figs. 44-46 ammonia spray does not hit the engine head, but it interacts with the piston bowl at various degrees dependently on the injection timing. Therefore, an appropriate wall treatment has to be considered in the Lagrangian spray modelling. Lagrangian parcels can either create a wall film or rebound and slide during contact with a wall. Rebounding would significantly influence the flow field and the ammonia-related scalar

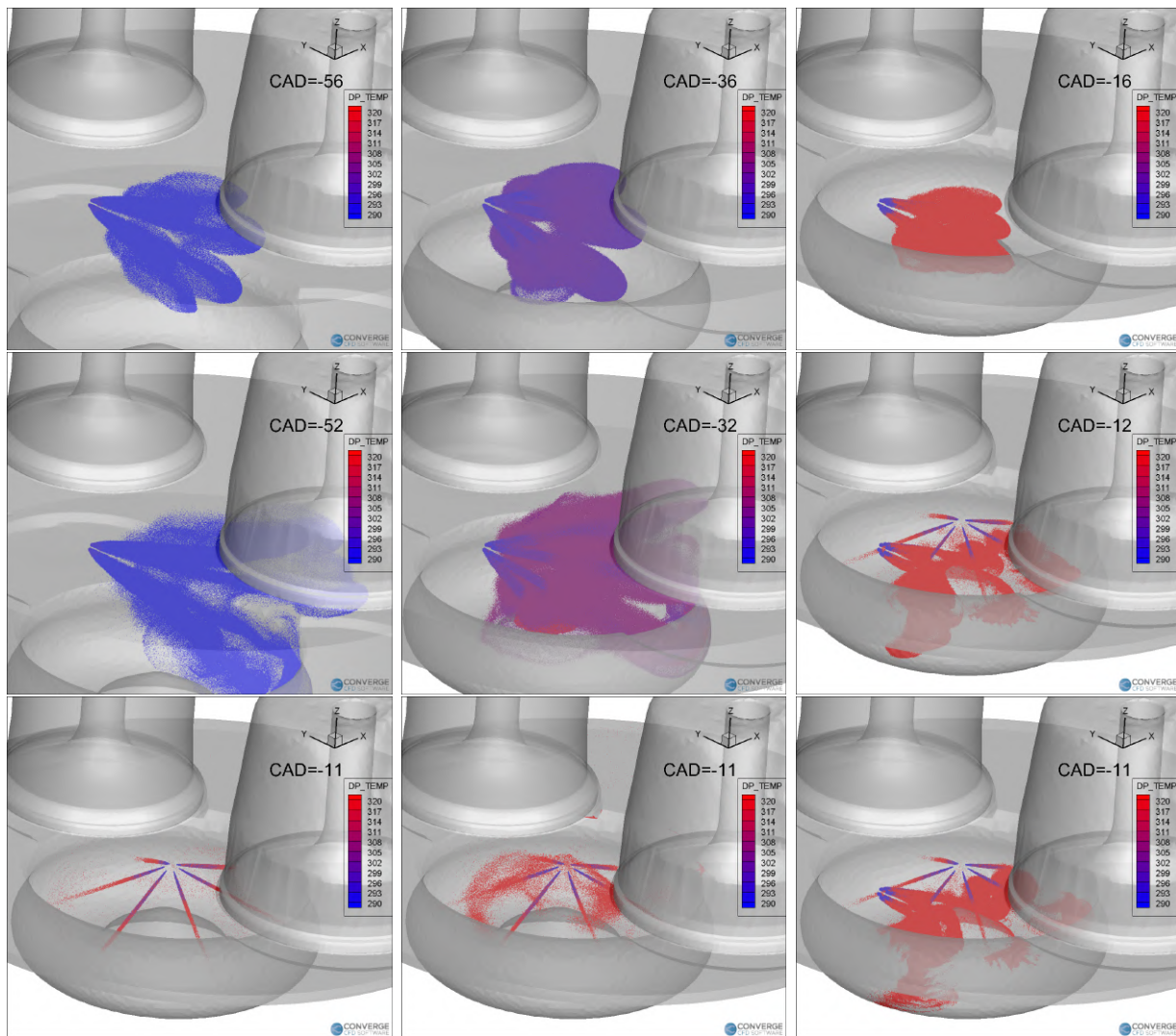


Figure 44: Parcels representing liquid fuel spray colored by temperature for the three injection times: -60 CAD, -40 CAD and -20 CAD shown in first, second and third column, respectively. First, second and third rows show snapshots 4 CAD, 8 CAD and 12 CAD after ammonia injection and the fourth row shows results from 4 CAD after diesel injection.

fields, and also this is not representative of the considered physical behaviour. Considering wall film require the involvement of other submodels to determine film properties and account for its evaporation. In this study, O'Rourke film splash model has been employed, and the splashing was determined using criteria based on Weber number, film thickness, and viscosity. Additionally, evaporation of the film was allowed to ensure complete ammonia evaporation.

Figure 47 show the amount of evaporated ammonia and diesel mass for the three different ammonia injection timings. It takes about 20-25 CAD to evaporate all the ammonia mass for all the injections, however, as shown in the right plot of Fig. 47 evaporation rate for SOI at -20 CAD aTDC is higher, and the process is shorter compared to the two earlier injections whose evaporation rate profiles are very similar. However, at the beginning of the

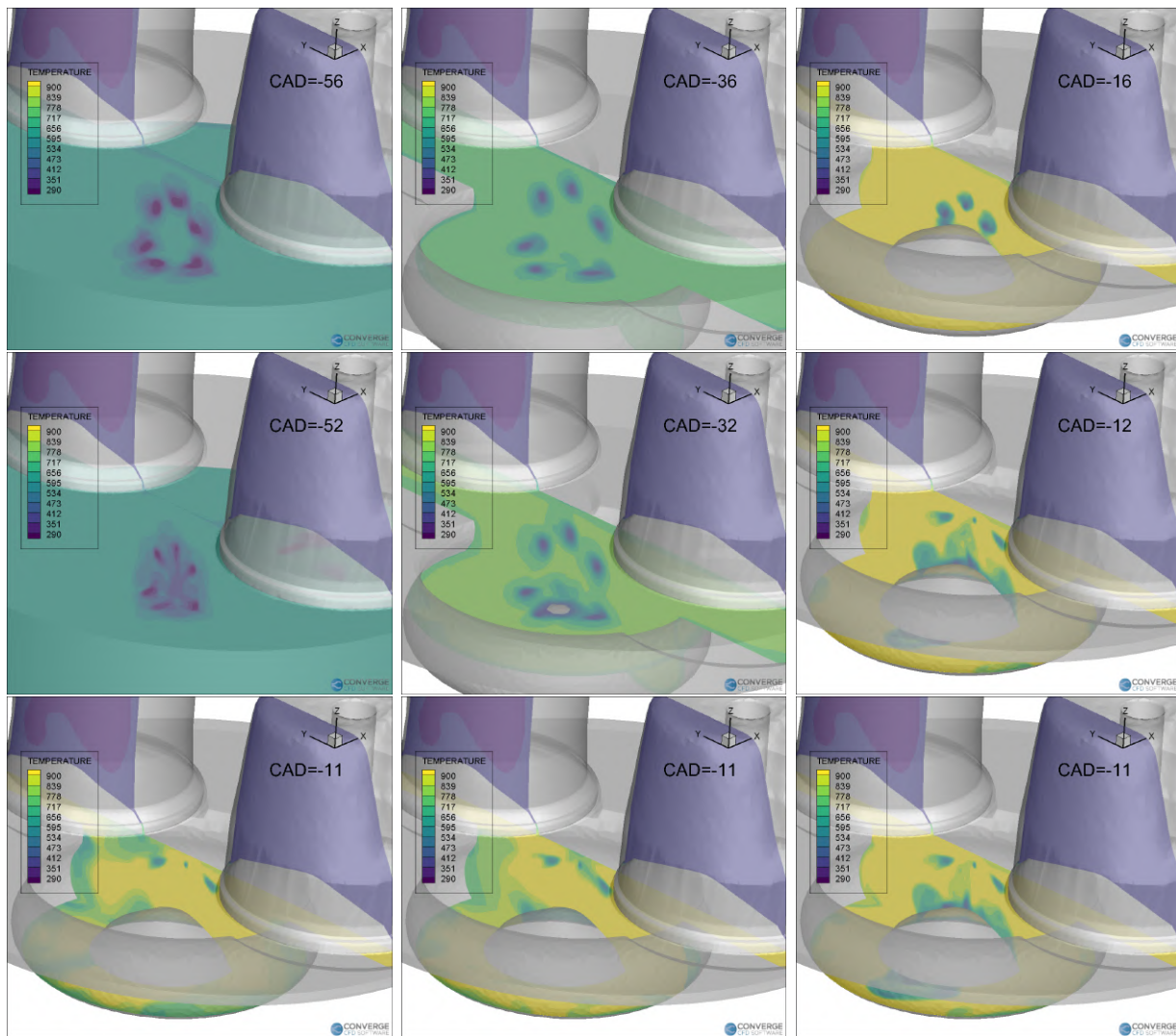


Figure 45: Temperature contours at selected YZ and YX cross-sections for the three injection times: -60 CAD, -40 CAD and -20 CAD shown in first, second and third column, respectively. First, second and third rows show snapshots 4 CAD, 8 CAD and 12 CAD after ammonia injection and the fourth row shows results from 4 CAD after diesel injection.

early injection at -60 CAD aTDC the evaporation rate is much steeper than for the medium injection timing due to the flash boiling presence. The dotted black vertical line on the left plot in Fig. 47 denotes -15 CAD aTDC when diesel pilot fuel is injected, and arrows point out the amount of ammonia mass at the gaseous phase at that time. For the two early injections, all the mass is evaporated at the time of pilot fuel injection, and for the case with SOI at -60 CAD, there is enough time for premixing the ammonia prior to its combustion. Ammonia is completely vaporized for the medium injection time just after the pilot fuel injection; thus, no full premixing can be achieved. On the other hand, for the late injection case, only 19% of the ammonia mass has evaporated, and the two fuels injections overlap, and fully non-premixed combustion mode is foreseen driven by mixing and diffusion.

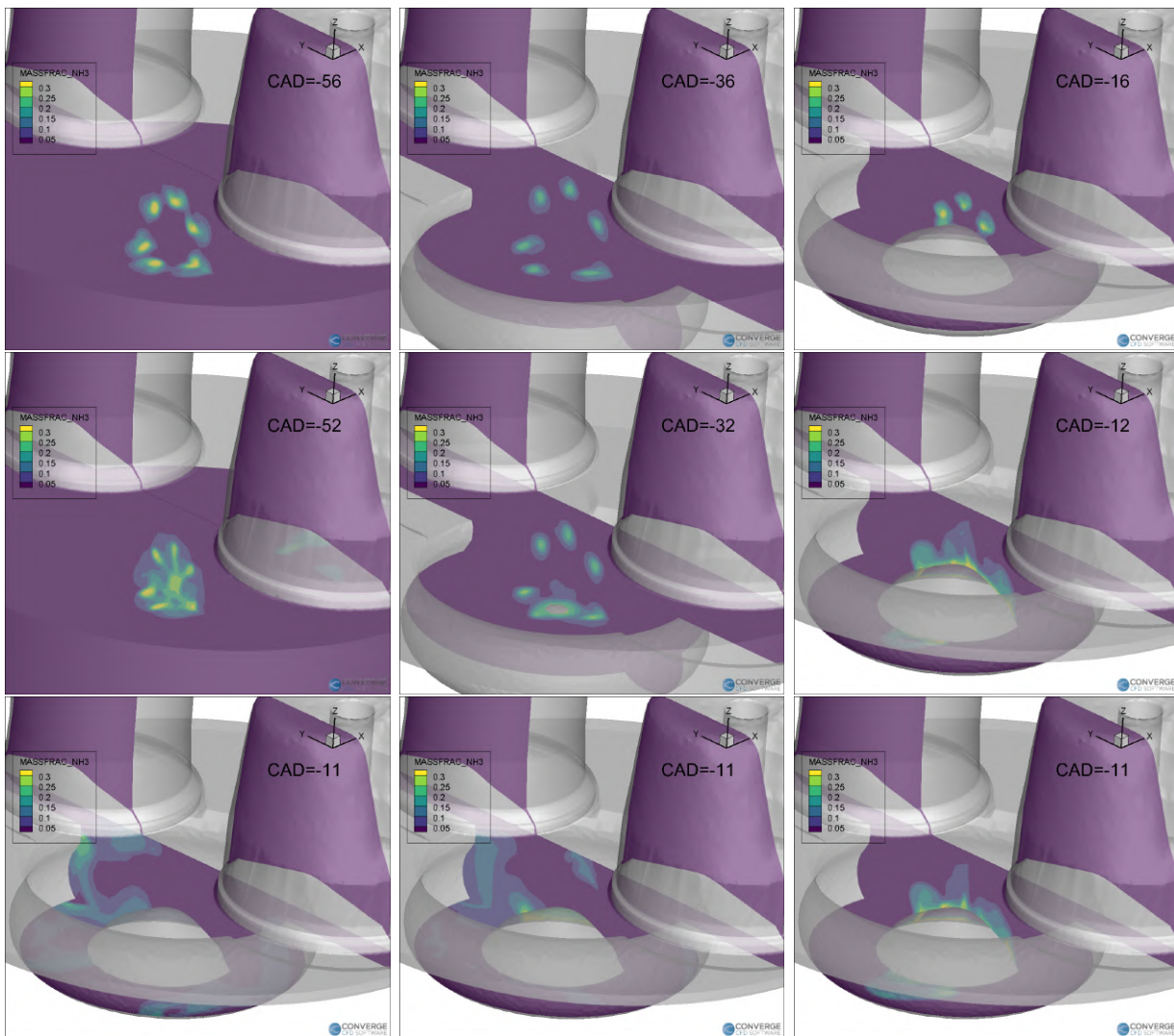


Figure 46: Ammonia mass fraction contours at selected YZ and YX cross-sections for the three injection times: -60 CAD, -40 CAD and -20 CAD shown in first, second and third column, respectively. First, second and third rows show snapshots 4 CAD, 8 CAD and 12 CAD after ammonia injection and the fourth row shows results from 4 CAD after diesel injection.

Mixture formation

Presented in Sec. 4.1 average time scale provides some global information about the turbulence-driven mixing process but does not say much about mixture homogeneity itself. Here, the ammonia mass fraction results are presented to show how the mixture is formed and how it looks like during pilot fuel injection. The result should show how well mixed is the ammonia within the cylinder and the piston bowl during early injections and how the mixture is formed during later injections. These results can also help adjust the pilot fuel injection timings but also its direction. Much smaller pilot fuel portions must be injected during the operation at a high ammonia fraction than regular operation. Therefore, the electronically

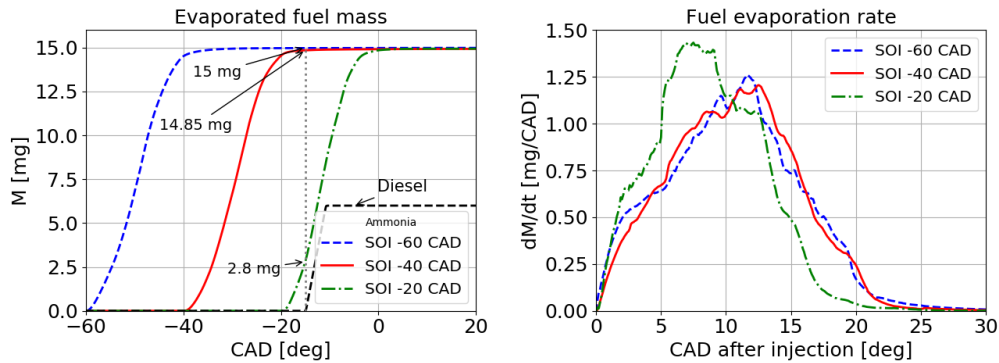


Figure 47: Evaporated mass of fuel for the three different ammonia injection timings (left). Colour lines denote evaporated mass of ammonia whereas black dashed line stands for evaporated pilot fuel. Right plot shows rate of ammonia evaporation as a function of CAD after start of injection.

controlled common rail diesel injector may have to be modified by welding some of the nozzles to provide lower mass flow rates. Consequently, the decision must be taken on which nozzle should be closed and which should remain open. It is known that for pure ammonia, leaner mixtures show higher reactivity [48]. However, for ammonia blends with other fuels, ignition delay time dependence on equivalence ratio may differ. With this information, one may target certain regions with a pilot fuel injection to more effectively promote ignition.

Figures 48 - 50 show isocontours of ammonia mass fraction at the values of 0.08, 0.15 and 0.25 (purple, green and yellow, respectively) for the three injection timings at different views at the time of -13 CAD aTDC during the pilot fuel injection. Assuming that all the remaining mass fraction is air, these values correspond to the equivalence ratios of approximately 0.5, 1, and 2, respectively. In these simulations, we have 405 mg air and 15 mg NH_3 (global $\phi=0.22$). Note that the colour surfaces are isocontours, so e.g. in late ammonia injection, there are rich regions inside the spray. Black dots representing Lagrangian parcels are shown to visualize the pilot fuel single spray plumes directions. Additionally, it should be pointed out that as mentioned in the milestone report M3.1, liquid penetration length has not been validated, and not all the ammonia spray modelling aspects are resolved. Therefore, it should be kept in mind that ammonia spray behaviour may differ. However, compared to the experimental results of Pelé et al. [40], we somewhat underestimated liquid penetration length, but still, we experienced spray wall interaction inside the engine's combustion chamber.

Because the ammonia GDI injector enters the chamber at an angle, ammonia air mixture formation is strongly dependent on the fixed spray direction. However, the results of early injection case with SOI at -60 CAD aTDC show relatively well-mixed ammonia evenly distributed within the piston bowl with only several rich spots. In such conditions, initiated combustion would result in mixed mode, i.e. kinetically controlled for ammonia and classical diffusion flame for diesel. On the other hand, for the case with SOI at -40 CAD aTDC, ammonia has also already completely evaporated and is spread over the piston bowl; however, a distinct rich region is located where the ammonia spray hit the piston wall. When ammonia is injected at -20 CAD aTDC, the liquid spray is still present at -13 CAD aTDC,

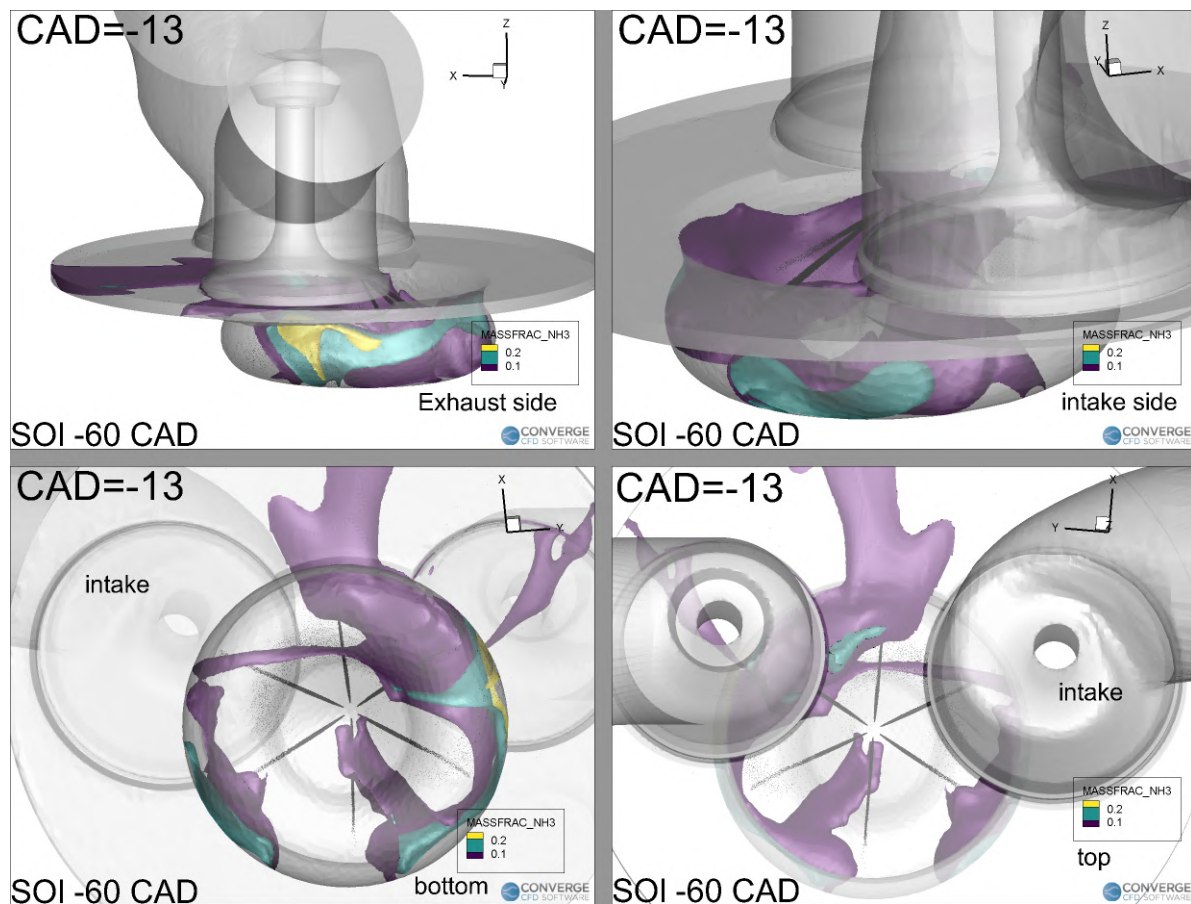


Figure 48: Isocontours of ammonia mass fraction at the level of 0.08, 0.15 and 0.25 (purple, green and yellow, respectively). Screenshots consider case with ammonia SOI at -60 CAD aTDC and the time of -13 CAD shortly after diesel injection (black points represent spray parcels) for exhaust side view (top left), intake side view (top right), bottom view (bottom left) and top view (bottom right).

and a wide spectrum of the mass fraction is present, with the visible lean region in the outer side at the top of the spray (three top plumes) and the massive rich region at the tip of the piston bowl visible from the bottom view (see Fig. 50), where the spray collides with the wall. If leaner mixtures are easier to ignite, one may think of north/east-north-west or south/east-south-west (looking at the top view) nozzles of the GDI injector are good candidates to remain open.

Summary

The process of building a CFD model of a single-cylinder Hatz engine has been presented. The example thermodynamic conditions have been analysed to identify superheated conditions for ammonia. In order to account for flash boiling in the spray simulations, relevant models have been selected based on findings from the previous M3.1 report. To reproduce ammonia spray shape full outer spray angles were assigned based on the experimental mea-

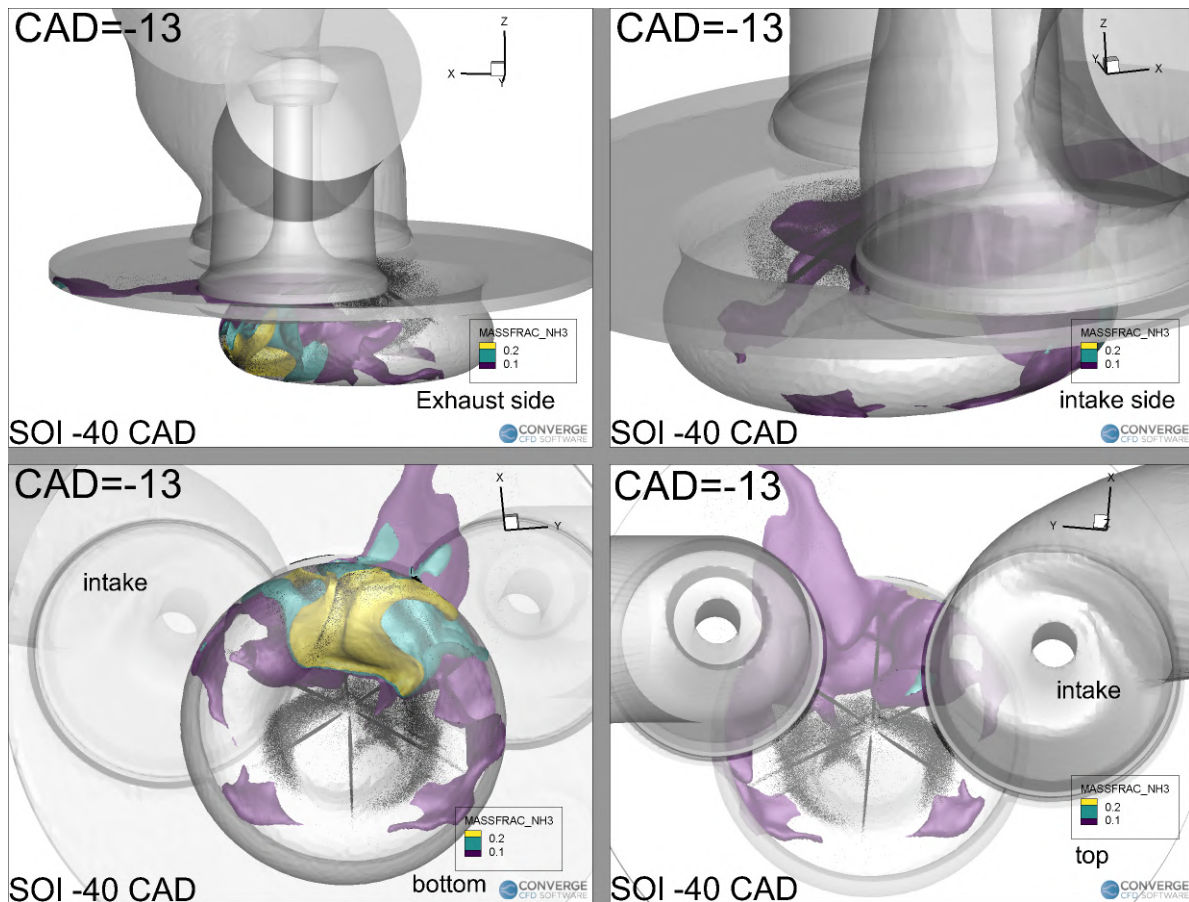


Figure 49: Isocontours of ammonia mass fraction at the level of 0.08, 0.15 and 0.25 (purple, green and yellow, respectively). Screenshots consider case with ammonia SOI at -40 CAD aTDC and the time of -13 CAD shortly after diesel injection (black points represent spray parcels) for exhaust side view (top left), intake side view (top right), bottom view (bottom left) and top view (bottom right).

measurements of Pelé et al. [40] and propositions of Duronio et al. [22] for flash boiling and non-flash boiling conditions. Three cases with different start of ammonia injections have been selected and further analysed. Presented results consider mixing time scale as an essential input parameter to the 0D Stochastic Reactor Model simulations. Additionally, the ammonia evaporation process and its cooling effect have been assessed. Finally, mixture formation for the selected injection timings has been studied to provide initial ideas about expected combustion modes and provide guidelines on which diesel injector nozzles should remain open to ignite ammonia effectively.

The main observations and conclusions that can be drawn from the analysed results are as follows:

- The mixing time drops down to the similar value for both NH_3 and diesel injections regardless of ammonia SOI;
- Even for ammonia SOI at -60 CAD aTDC mixing time does not come back to the

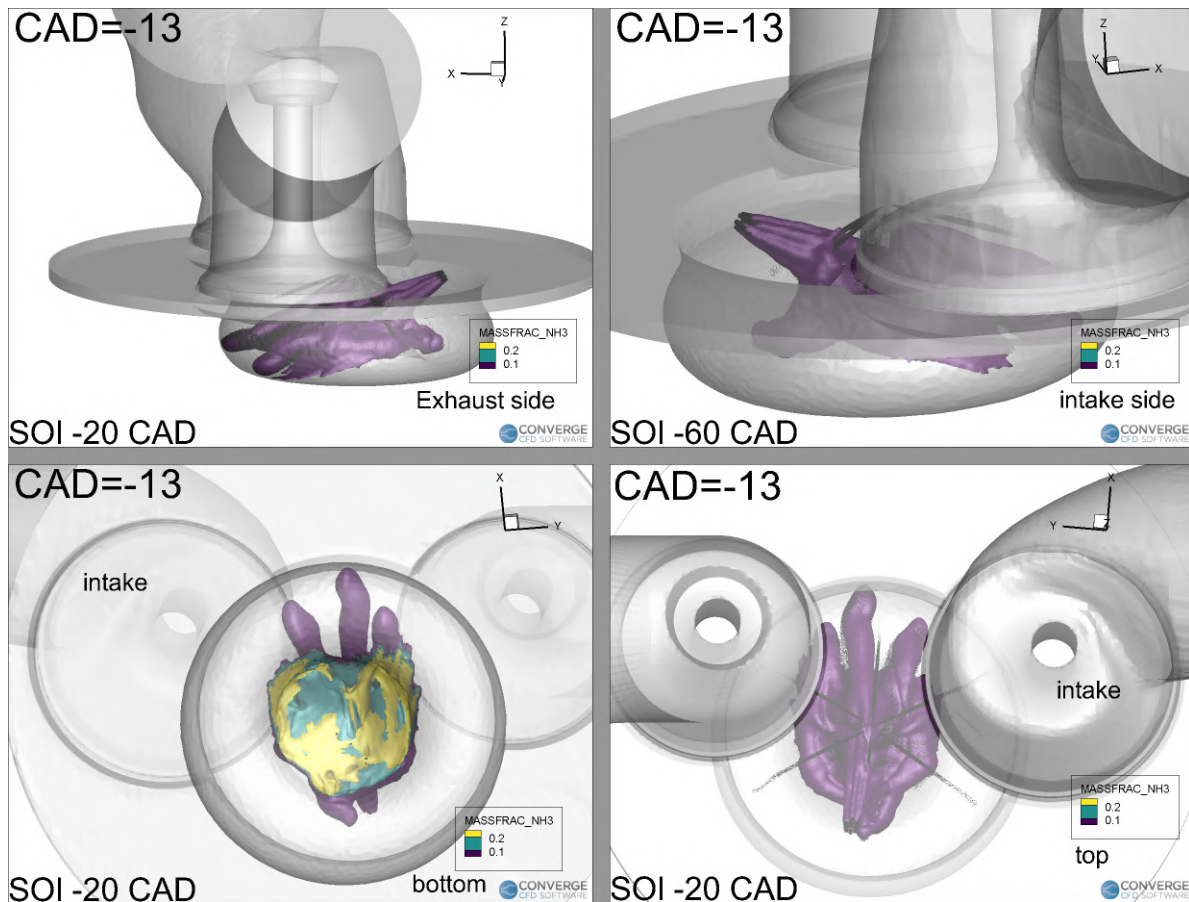


Figure 50: Isocontours of ammonia mass fraction at the level of 0.08, 0.15 and 0.25 (purple, green and yellow, respectively). Screenshots consider case with ammonia SOI at -20 CAD aTDC and the time of -13 CAD shortly after diesel injection (black points represent spray parcels) for exhaust side view (top left), intake side view (top right), bottom view (bottom left) and top view (bottom right).

non-injection profile prior to diesel injection, and in general, all three profiles differ until diesel injection and the compression stroke when they become similar;

- Although liquid ammonia spray - head wall interaction has been excluded, the ammonia liquid spray will hit the piston bowl walls. The piston is made of aluminium so no corrosion is expected;
- Ammonia injection decreases the mean in-cylinder temperature and pressure at TDC by 120 K and 5 bar, respectively;
- For the late ammonia injection, pilot diesel fuel dose enters the combustion chamber when the mean gas temperature is the highest;
- Temperature field is inversely proportional to ammonia mass fraction field, thus ammonia is concentrated in the low-temperature regions what indicates a featured problem of ammonia ignition without pilot fuel injection or another type of ignition promotion;

- Ammonia completely evaporates prior to the pilot fuel injection at -15 CAD aTDC if injected between -60 and -40 CAD aTDC;
- Ammonia evaporation rate for early injection at flash boiling conditions is similar to the one at medium injection time, but the highest evaporation rate is during late fuel injection;
- Premixed combustion mode is expected at the two early injections where the early injection provides a relatively homogeneous mixture, and for the medium injection, a distinct rich region is located in the piston bowl. The late injection is expected to lead to non-premixed combustion as it overlaps with the diesel injector and ammonia still evaporates;
- Mixture formation analysis gave guidelines on which diesel injector nozzles should remain open.

4.2 Impact of ammonia share in the fuel for a given fuel injection strategy

Scope of work

The primary objective of the work is the determination via 0D simulations the maximum ammonia energy share in the total fuel mass that the engine can tolerate without penalty in overall performance parameters and combustion stability for a given fuel injection strategy; determination of the optimum fuel mixture composition. This work was projected as supporting the developments by the team at Silesian University of Technology (SUT) while retrofitting the baseline compression ignition (CI) engine to the operation with ammonia being directly injected into the cylinder. Similarly as reported in Sec. 3.2 the work here reported also aims to further assess the feasibility of using that SRM-based approach to simulate a CI engine ammonia and biodiesel being directly injected into the cylinder.

Engine data, reference operating point and numerical model setup

Simulations presented in this report refer to the same engine and experimental data as the ones described in Fig. 3.4 Detailed information about the data can be found in the reports by project partner from SUT who investigated the engine experimentally. The basic specification of the engine is given in Table 4. Table 5 summarizes operating conditions for four operating points that are depicted in Fig. 51 At these points the engine was operated at fixed start of injection (SOI) for biodiesel and varied SOI of ammonia.

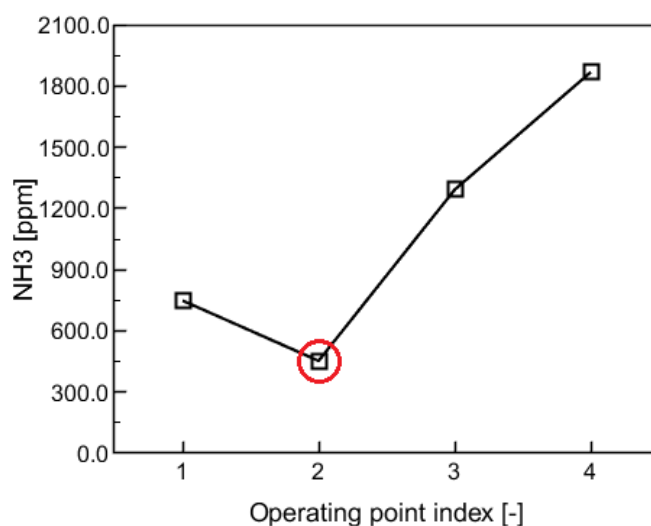


Figure 51: Measured concentration of ammonia in engine exhaust gasses for OPs in Table 5.

Out of four operating points presented in Table 5, OP2 was selected as basis for the analysis of the impact of increasing the ammonia energy share in the fuel on overall engine performance parameters and exhaust emissions. The OP2 was selected since at this point the lowest engine out ammonia was measured as shown in Figure 51. Table 8 summarizes parameters of the SRM that were used through the simulations and Table 9 lists the most important parameters of the $k - \epsilon$ turbulence model. These parameters were defined during model calibration presented in Sec. 3

Combustion metrics

Ammonia energy share (AES) The share of ammonia in the total energy delivered with the fuel was calculated according to the formula given by Eq. 4.

Rate of heat release (RoHR) The history of RoHR is used to quantify the combustion process. It provides the information about the ignition delay time, the start of combustion (SOC), the end of combustion (EOC) and the amount of heat transferred to the wall. Finally, it determines the total amount of the energy that is released during combustion. These parameters further complement the information obtained from the in-cylinder pressure data. RoHR is calculated from the in-cylinder pressure data (p), changes of the cylinder volume (V) and it depends on the in-cylinder mixture composition that is expressed by the ratio of specific heats (γ). The calculation of RoHR is carried out incrementally with time step defined by crank angle degree (φ).

$$RoHR [J/deg] = \frac{\gamma}{\gamma - 1} p \frac{dV}{d\varphi} + \frac{1}{\gamma - 1} V \frac{dp}{d\varphi}. \quad (5)$$

The RoHR history obtained from Eq. 5 is referred to as the apparent rate of heat release that is a measure of the energy effectively absorbed by the working fluid; integrating Eq. 5 over the closed part of the engine cycle, one obtains cumulative heat release (CHR). By defining a crank angle (CA) corresponding to the point where on the CHR history 50% of the energy has been released, one obtains combustion center that is denoted by CA_{50} and is another parameter used for quantifying the combustion process.

Indicative thermal efficiency (ITE) The ITE was calculated based as the ratio of the indicative work (W_i) and the energy delivered with the fuel that was calculated from known masses of ammonia (m_{NH_3}) and MD, and their corresponding LHV values.

$$ITE [\%] = \frac{W_i}{m_{NH_3} LHV_{NH_3} + m_{MD} LHV_{MD}} \times 100. \quad (6)$$

Baseline model calibration

Simulations pertaining to the analysis of the impact of increasing the ammonia energy share in the fuel on overall engine performance parameters and exhaust emissions were carried using as basis the the 0D model calibrated for OP2 from Table 5. The results of the calibration process are, for selected engine parameters, presented in Figure 29.

Starting from the calibrated baseline model (AES=26%), simulations were carried out in two modes: 1) at fixed equivalence ratio (ϕ) and consequently varied load due different amount of ammonia in the fuel, and 2) at constant engine load that was due to the changes in total fuel mass and ϕ . These two modes are discussed in the next paragraphs.

Results for varied engine load

The share of ammonia in the total fuel mass was increased gradually, and at the same time, the total mass of fuel and actual air fuel ratio were kept constant. In such a configuration, the energy delivered to the engine with the injected fuel varies due to the increased share of ammonia that has LHV lower than that of biodiesel. Results obtained in this configuration are refereed to as results for varied engine load.

Initially, the share of ammonia in the total fuel mass was increased gradually from 0% to 100%. However, the preliminary results showed that for operating points with above AES=56% the quality of combustion dramatically deteriorates and therefore we excluded these points from the analysis. The matrix of investigated operating points is presented in Table 14 and the obtained results are in Figure 52 and Figure 53.

Table 14: Matrix of operating points for simulating the impact of ammonia share at varied load. Operating condition No. 9 corresponds to the baseline model OP2 presented in Figure 29.

No.	NH3 [-]	MD [-]	$E_{in,tot}$ [MJ/kg]	$E_{in,NH3}$ [MJ/kg]	AES [%]
1	0	1	34.44	0	0
2	0.05	0.95	33.65	0.93	2.8
3	0.1	0.9	32.86	1.86	5.7
4	0.15	0.85	32.07	2.79	8.7
5	0.2	0.8	31.27	3.72	11.9
6	0.25	0.75	30.48	4.65	15.3
7	0.3	0.7	29.69	5.58	18.8
8	0.35	0.65	28.9	6.51	22.5
9	0.39	0.61	28.26	7.25	25.7
10	0.4	0.6	28.11	7.44	26.5
11	0.45	0.55	27.31	8.37	30.6
12	0.5	0.5	26.52	9.3	35.1
13	0.55	0.45	25.73	10.23	39.8
14	0.6	0.4	24.94	11.16	44.7
15	0.64	0.36	24.3	11.9	49
16	0.65	0.35	24.15	12.09	50.1
17	0.66	0.34	23.99	12.28	51.2
18	0.67	0.33	23.83	12.46	52.3
19	0.68	0.32	23.67	12.65	53.4
20	0.7	0.3	23.35	13.02	56

Figure 52 shows selected engine operating quantities as a function of crank angle. These results visualize how the increase of ammonia deteriorates the combustion process – more exhaust NH3 and MD, lower levels of MFB, in-cylinder pressure, temperature, and RoHR. These results are further supplemented by the results in Figure 53 that provides global engine in-cylinder performance parameter for the analyzed matrix of operating points. In this report as global results we understand these that describe through a single value engine in-cylinder processes that are crank angle dependent in an actual engine cycle. The global results are useful for determining the limiting value of AES, above which the engine operates less efficiently and with more engine out ammonia.

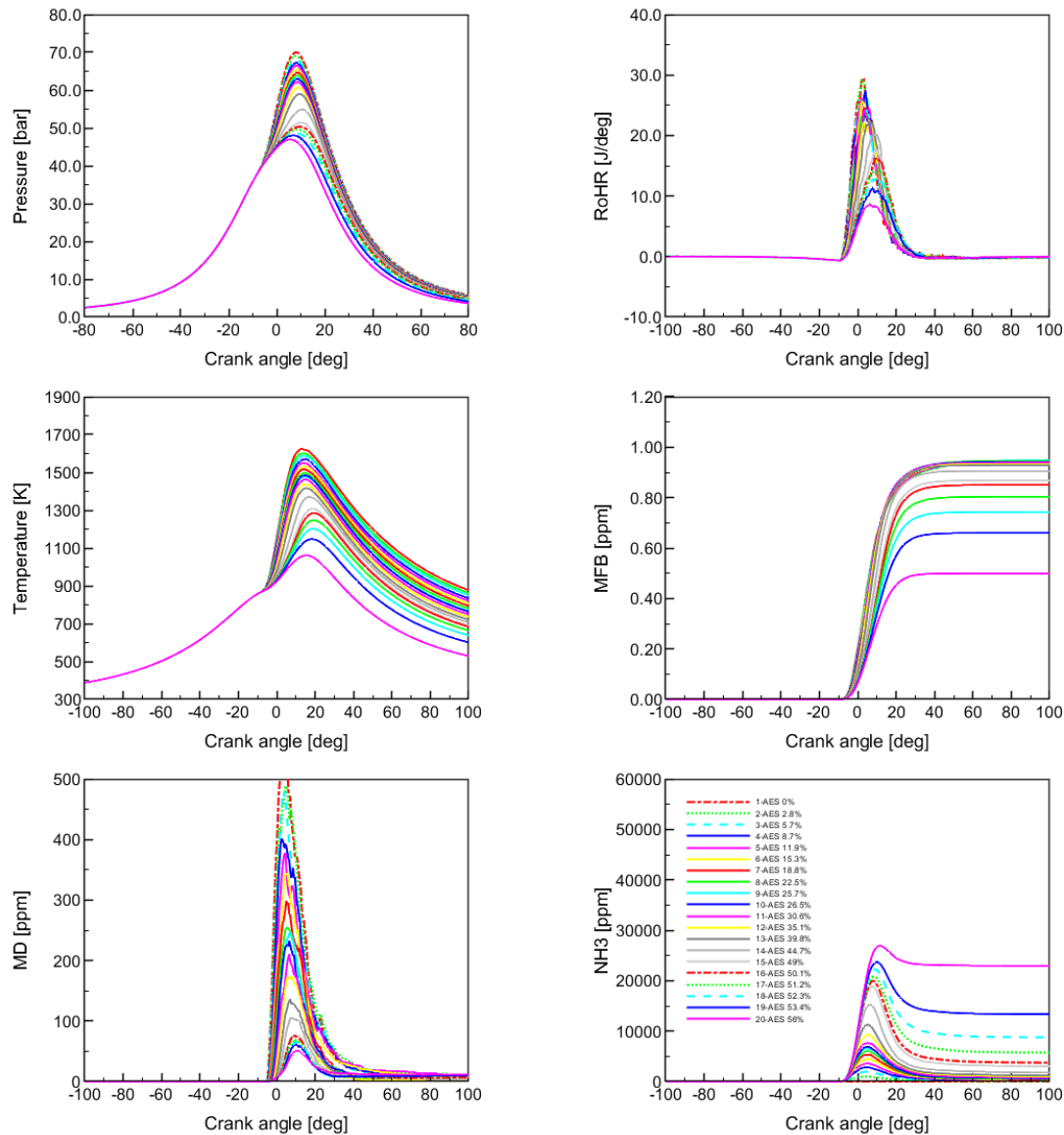


Figure 52: Selected, crank angle based, engine in-cylinder performance parameters for different ratio of ammonia and biodiesel that is represented by methyldecanoate (MD).

From the results in Figure 52 and Figure 53, one can conclude that for the considered fuel injection strategy, AES=50% is the last point for which the thermal efficiency is at a level that is comparable to the points with AES<50%. After that point a decrease of ITE is observed that for AES=56% reaches almost 50% of that for the baseline point (AES=26%). For AES above 56% only a marginal amount of energy is released with extremely high engine out emissions and as mentioned earlier, these points were excluded from the analysis. Using ITE as a criterion, one can say that AES=50% is a limit for this operating point for stable and efficient operation. For AES above 50%, and up to 56%, the quality of combustion starts decreasing significantly.

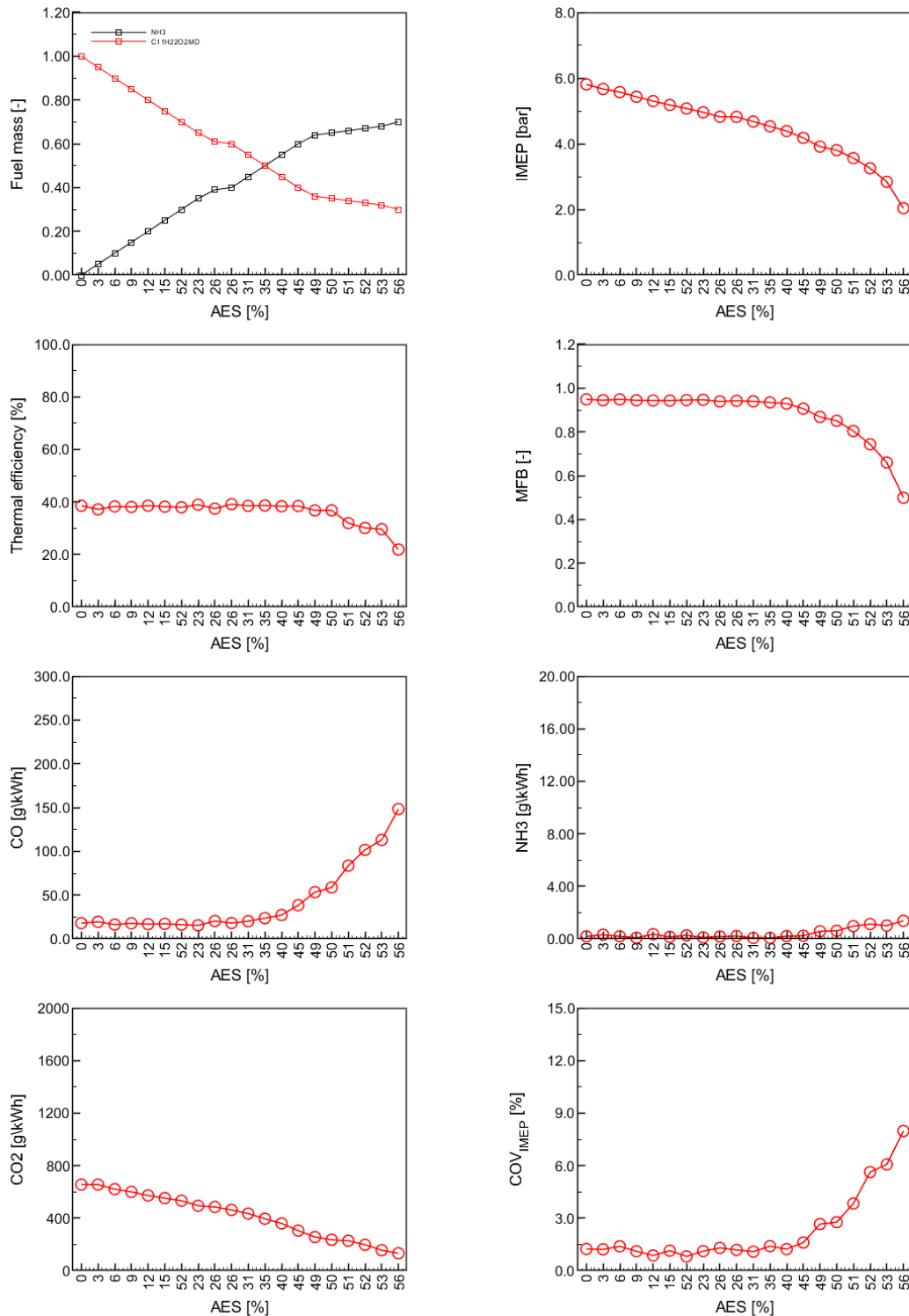


Figure 53: Selected global engine in-cylinder performance parameters for different ratio of ammonia and biodiesel.

Results for constant engine load

As results at constant engine load are referred those obtained with the same amount of energy delivered to the cylinder due to fuel injection, and for every investigated operating point. To maintain constant load for increased amount of ammonia, the mass of MD must have been increased to compensate for lower LHV of ammonia. This have led to also different lambda for every investigated operating point (Table 15). Calculations were carried out for AES between 0% and 100%. However, at operating points with AES above 57% the quality of combustion was extremely poor, with only a marginal amount of energy was released. Therefore we excluded these points from the analysis.

Table 15: Matrix of operating points for simulating the impact of ammonia share at fixed load.

No.	$E_{in,tot}$ [MJ/kg]	$E_{in,MD}$ [MJ/kg]	E_{in,NH_3} [MJ/kg]	AES [%]	Lambda [-]
1	28.26	21.01	7.25	26%	2.41
2	28.26	18.94	9.32	33%	2.435
3	28.26	17.22	11.04	39%	2.457
4	28.26	15.5	12.76	45%	2.479
5	28.26	13.78	14.48	51%	2.501
6	28.26	13.43	14.83	52%	2.506
7	28.26	13.27	14.99	53%	2.508
8	28.26	13.09	15.17	54%	2.51
9	28.26	12.74	15.52	55%	2.515
10	28.26	12.4	15.86	56%	2.519
11	28.26	12.05	16.21	57%	2.524

- Results for the baseline fuel injection timings

Simulations of operating points listed in Table 15 were carried out with fuel injection timings the same as for the baseline point (OP2 in Table 5).

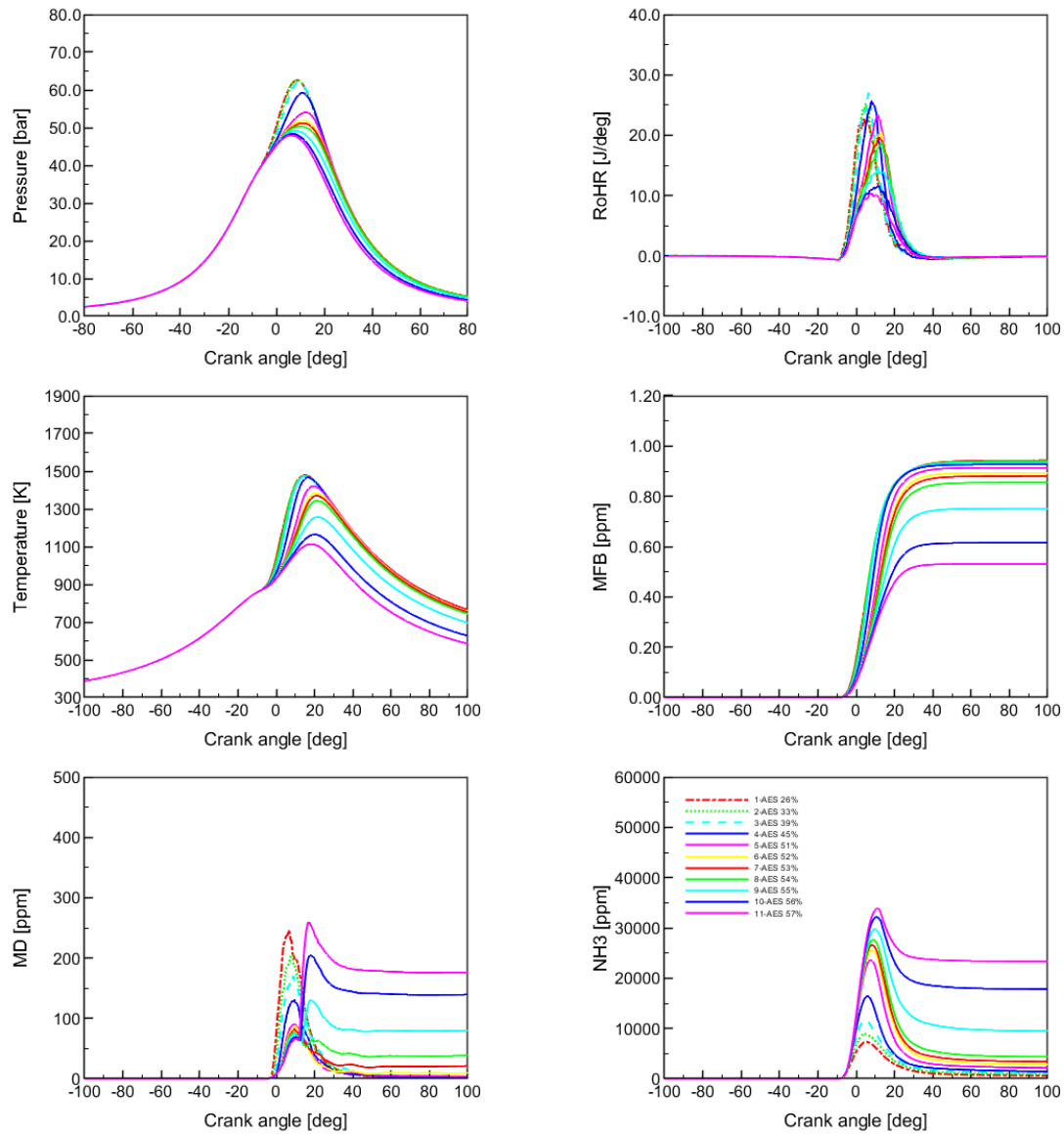


Figure 54: Selected, crank angle based, engine in-cylinder performance parameters for different ratio of ammonia and biodiesel that is represented by methyldecanoate (MD); fixed energy delivered to the cylinder due to fuel injection.

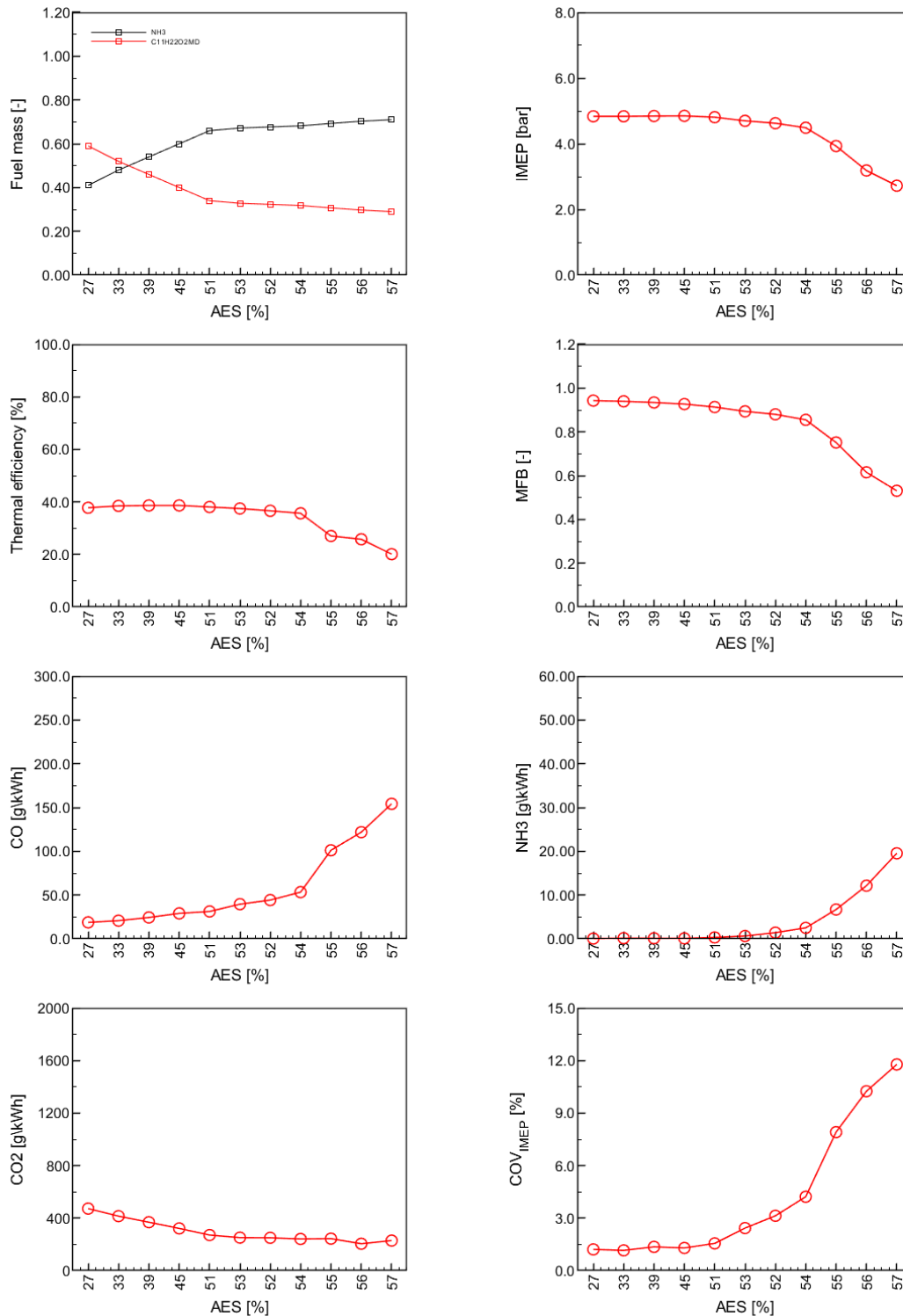


Figure 55: Selected global engine in-cylinder performance parameters for different ratio of ammonia and biodiesel; fixed energy delivered to the cylinder due to fuel injection.

Up to AES=54% ITE is at a level that is comparable to the points with AES<54%. After that point, the ITE starts decreasing and for AES=57% the ITE drops down by almost factor 2. For AES above 57% only a marginal amount of energy was released these points were excluded from the analysis. For AES above 54% the ITE, MFB, IMEP decrease even though the energy input due to injected fuel remains unchanged (Table 15). This further indicates on deteriorating the quality of combustion for AES above 54%.

• Results for the optimized fuel injection timings

Increasing AES from the baseline value 26% to 54% have deteriorated engine performance parameters and exhaust emission even though that the energy delivered with the injected fuel was the same in both cases. The location of CA₅₀ is delayed that results in lower IMEP. CO and NH₃ emissions, expressed in the unit of g/kWh, increase that is due to lower IMEP, but indicates also less efficient combustion. The relative increase of NH₃ can also be due to more ammonia in the fuel along with its less efficient burning. CO₂ is reduced as the amount of biodiesel in the fuel is reduced, but it is also affected by less efficient combustion seen in an increase of CO emission. From the results in Figure 54 it is expected that advancing the location of CA₅₀, which is delayed when compared to the baseline result (AES=26%), could improve the results for AES=54%. The most effective and simplest way to advance CA₅₀ is the advancing of SOI that was done in this work. The results are presented in Figure 56.

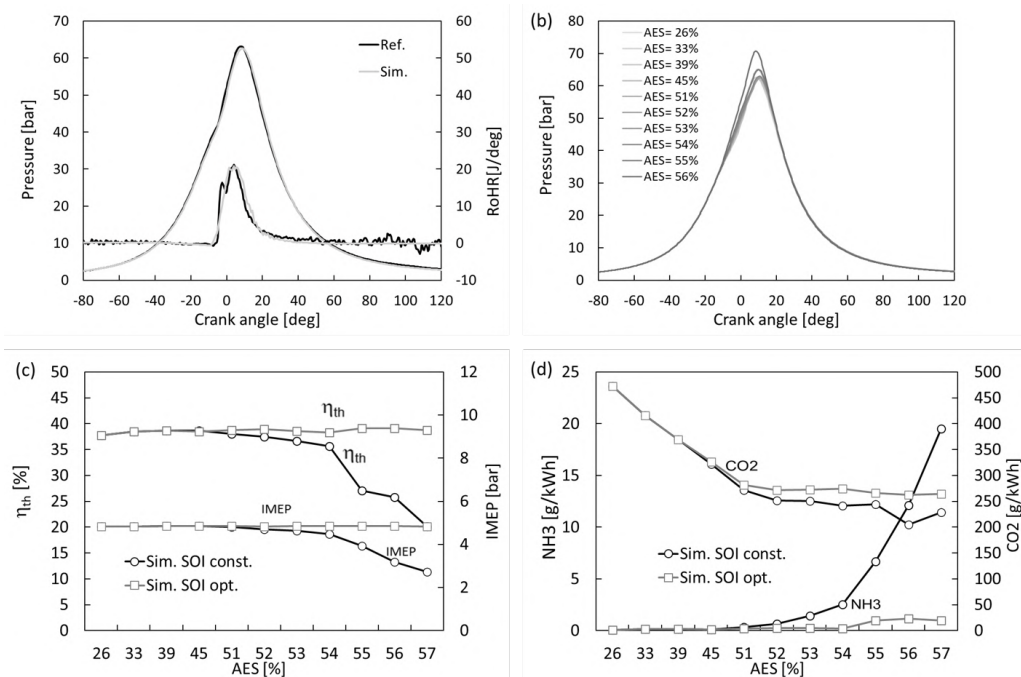


Figure 56: Prediction of selected engine performance parameters for varied ammonia energy share due to fuel injection; comparison between simulated and reference histories of in-cylinder pressure for the baseline operating point (a), effect of AES variation on in-cylinder pressure (b), thermal efficiency and IMEP (c), and engine out NH₃ and CO₂ (d).

The simulations indicate the possibility of operating the research engine considered here with an AES of about 70 %. However, this was associated with a dramatic increase in unburned ammonia. Even at an AES of 57%, the predicted maximum pressure peak (Figure 56b) exceeds the reference value that we assumed as the limit in the simulations. Thanks to the optimization of the SOI, the IMEP and thermal efficiency for AES 55% to 57% are comparable to the baseline value at AES 26%. However, at these values, a small increase in the NH₃ output of the engine is also observed (Figure 56ld). In contrast, both IMEP and thermal efficiency begin to decrease when an increase in AES is not accompanied by an increase of SOI. This highlights the importance of SOI optimization when increasing AES. With an optimized SOI and an AES between 51% and 57%, the combustion process is more efficient and reduces CO and unburned hydrocarbons, which in turn leads to higher CO₂ emission (Figure 56d). From the studies performed, an AES of 54% appears to be the maximum for efficient combustion without penalty in NH₃ emission for the engine and operating point studied. At an AES value of 54%, the SOI was advanced by 4 degrees. IMEP and thermal efficiency are comparable to the baseline operating point values. Engine NH₃ emissions increased by about 6% and CO₂ emission was reduced by about 40% compared to the baseline operating point.

Summary

The major achievements and results of this part of the work are summarized as follow.

- Ammonia energy share at varied engine load. For the considered fuel injection strategy, AES=50% is the last point for which the thermal efficiency is at a level that is comparable to the points with AES<50% and similar to the baseline point (AES=26%). Above AES=50% a decrease of ITE is observed that for AES=56% reaches almost 50% of that for the baseline point. The results indicate that AES=50% is a limit for this operating point for stable and efficient operation. For AES above 50%, the quality of combustion starts visibly decreasing.
- Ammonia energy share for fixed engine load and baseline fuel injection strategy. For AES=54% ITE is at a level that is comparable to the points with AES<54%. Thus AES=54% is considered as a limiting in this configuration. Then, the ITE starts decreasing, and for AES=57% it drops down by almost factor 2. For AES above 54% the ITE, MFB, IMEP decrease even though the energy input due to injected fuel remains unchanged. This further indicates on deteriorating impact of ammonia on combustion quality for AES above 54%.
- Ammonia energy share for fixed engine load and optimized fuel injection timing. By advancing the SOI of both ammonia and biodiesel the results obtained at fixed load (AES=54%) were further improved. Due to advancing SOI by 4 CAD the CA₅₀ has been moved to the earlier part of the cycle. In consequence IMEP has been improved too that matches the one from the baseline operating point with AES=26%. At such a configuration (AES=54%, and advanced SOI) when comparing to the baseline results with AES=26%, engine out NH₃ and CO, increased only by 6% and 2.5%, respectively. The ITE increased by 2.5%, and CO₂ was reduced by approximately 40%.

4.3 Aspects of mixture formation in 0D and 3D models

Due to 0D formulation, the SRM requires calibration against reference data to mimic the impact of turbulence on mixing process and consequently on local properties of the in cylinder mixture, such as temperature and equivalence ratio, that govern emissions formation. Once calibrated, the SRM can be used to simulate engine performance parameters over wide range of operating points and hence, be helpful in evaluating many designs and operating strategies in short time. In turn, 3CFD simulations have more predictive character and are more accurate than 0D in replicating the state of the in-cylinder mixture. However, these benefits are occupied by much higher computational cost. Owing their features, the 3D CFD and 0D SRM are not competing modelling methods, but may supplement each other.

As a part of the investigations we compare the results from SRM with CFD of local properties of the in-cylinder mixture expressed by local temperature and equivalence ratio.

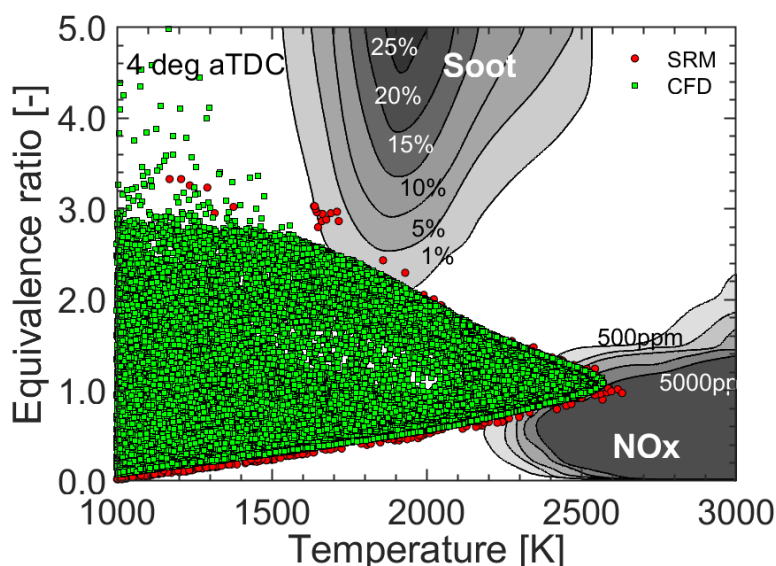


Figure 57: Temperature and equivalence ration map from 0D SRM and 3D CFD at 4 CAD aTDC for an engine operated at 1500 rpm with 27% of energy due to injected fuel coming from ammonia.

Overall, the results from 0D SRM match reasonable the counterparts from 3D CFD. More results (solution points) from the CFD model are due to much finer discretization of the computational domain. The "edge line" representing the transition from the unburned to burned state is similar for both models. The good agreement highlights the quality of 0D simulations. On the other hand, the CFD simulations can be used to verify how the in-cylinder mixture is captured by 0D simulations. Such as cross check provides an additional kind of authentication of 0D results when extrapolating the 0D model into operation where limited experimental data are available that may be the case at the early stage of retrofitting an existing engine into operation with ammonia. Overall, this can be understood as virtualization of engine development process.

4.4 Engine performance mapping

Scope of work

The focus of the work presented in this section was twofold. Firstly, we evaluated the possibility to map engine performance parameters and exhaust emissions over different engine speed and load conditions using the 0D SRM while having limited set of data for calibrating the model, and with having ammonia and biodiesel as fuel; extrapolating the application of the model to wider range of operating points is understood here as "engine performance mapping". Secondly, preliminary optimization of engine performance map was conducted to estimate the potential benefits of using ammonia for reducing engine out CO₂ without affecting engine output performance.

Method

Simulations were carried out using framework presented previously that relies on the 0D SRM and detailed chemistry integrated with modeFRONTIER®©. The SRM along with a detailed reaction mechanism for ammonia and biodiesel is embedded in the multi-objective optimization (MOO) platform. The same setup of the were carried out using the SRM from LOGEngine package that we used previously for the works in WP3.

Engine data and simulation setup

Simulations in this report refer to the same engine that we used previously for the works in WP3. This the engine from Silesian University of Technology (SUT) that is described in details in the reports by project partner from SUT who investigated it experimentally. The basic specification of the engine is given in Table 16.

Table 16: Engine basic specification.

Engine type	Compression ignition
Bore (mm)	86
Stroke (mm)	70
Compression ratio (-)	16.5:1
Number of valves (-)	4
Rated power (kW @3500rpm)	6.4

In total, 16 operating points were considered for the analysis. The points are characterized in Table 17, and Figure 58 shows in-cylinder pressure histories and IMEP corresponding to these points.

Table 17: Reference operating points for engine performance mapping.

No.	Speed [rev/min]	IMEP [rev/min]	NH3 [-]	MD [-]	Phi [-]	AES [-]	SOI NH3 [deg aTDC]	SOI MD [deg aTDC]
1	1000	1.96	0.5	0.5	0.21	0.34	-17	-21.1
2	1000	2.85	0.41	0.59	0.27	0.42	-15.1	-21.1
3	1000	3.64	0.41	0.59	0.3	0.42	-15	-15
4	1000	4.23	0.36	0.64	0.35	0.47	-5	-15
5	1000	6.68	0.43	0.57	0.66	0.40	-4.6	-10.1
6	2000	2.79	0.76	0.24	0.17	0.13	-7.3	-18
7	2000	3.95	0.69	0.31	0.25	0.18	-3.6	-17.1
8	2000	4.24	0.66	0.34	0.32	0.21	-4.3	-17.1
9	2000	4.97	0.6	0.4	0.38	0.25	-9.2	-18.5
10	2000	5.75	0.54	0.46	0.43	0.30	-15.9	-21
11	2000	7.34	0.49	0.51	0.57	0.34	-13.6	-20
12	2500	3.41	0.72	0.28	0.22	0.16	-7.4	-20
13	2500	4.02	0.8	0.2	0.3	0.11	-4.1	-19.7
14	2900	3.38	0.74	0.26	0.24	0.15	-7.5	-22
15	2900	4.03	0.74	0.26	0.3	0.15	-4.6	-22
16	2900	4.77	0.93	0.07	0.35	0.04	-4.6	-22

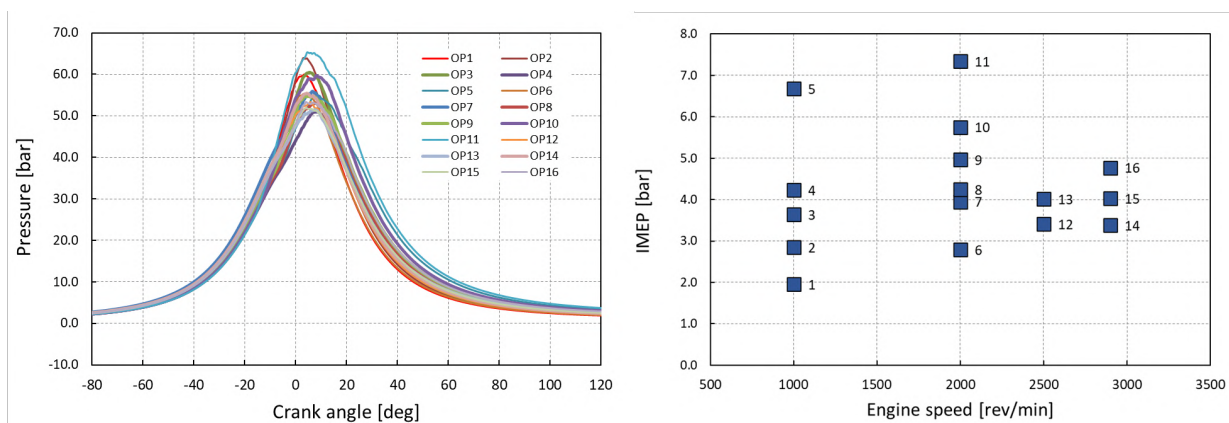


Figure 58: In-cylinder pressure histories and IMEP corresponding to operating points listed in Table 17.

Computational setup

Simulations were carried out using the SRM configured, in terms of number of particles, consecutive cycles and time step, as determined in previous investigation in the project. The parameters are summarized in Table 18.

Table 18: Setup of the SRM parameters.

Parameter	Value
Number of particles (-)	500
Number of cycles (-)	30
Time step (-)	0.5
Stochastic heat transfer coefficient (-)	15
Mixing model	Curl

Baseline model results

Calibration of the baseline SRM follows the procedure presented in the millstone and deliverable reports. For the present work, out of 16 points from Table 17, we selected 4 points for model calibration. These are OP3, OP6, OP12 and OP15. They represent different load and speed conditions.

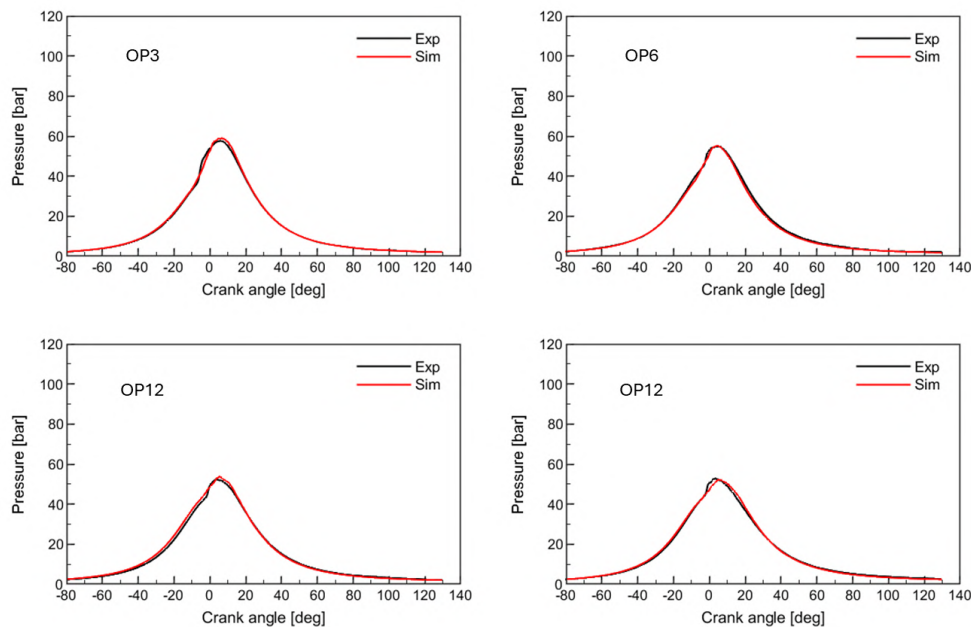


Figure 59: Comparison between the experimental and the simulated in-cylinder pressure histories for four operating points selected for training of the SRM.

Figure 59 compares the experimental and the simulated in-cylinder pressure histories for the selected four training operating points. The simulated histories follow reasonably well the experimental counterparts, though some mismatches are visible too. However, it needs to be pointed out that at the time of performing calculations we had information about injection timings, but there was no information about the injection rates for each fuel. These had to be presumed/calculated that introduced some in-accuracy into the modelling and obtained results. The lack of detailed rates data influences the modelling of vaporization process that is specifically important in predicting pollutants formation that are most sensitive parameters to simulate. Given these obstacles, here we limited the evaluation of the calibration quality to the in-cylinder pressure data (Figure 59), and we consider the obtained quality satisfactory.

SRM constants, that affect $k - \epsilon$ turbulence model, and hence the predicted combustion rates, and in consequence quality of the simulated in-cylinder pressure histories in Figure 59 were obtained through an automate calibration procedure using optimization algorithms. They are listed in Table 19, where $C_{\epsilon,1}$ and $C_{\epsilon,2}$ denote model parameters for in-cylinder flow and inflow/back squish flow, respectively. C_{inj} is the model parameter that influences the flow velocity due to fuel injection. C_τ is a general model parameter that enables scaling the history of mixing time.

Table 19: Constants of $k - \epsilon$ turbulence model in the calibrated SRM.

Parameter	$C_{\epsilon,1}$	$C_{\epsilon,2}$	C_{inj}	C_τ
Value	1.69	2.25	0.0089	9.22

Engine performance mapping

Having determined $k - \epsilon$ turbulence model (Table 19) the SRM was applied to simulate engine performance parameters for all 16 operating points listed in Table 17. The results obtained are presented in Figure 60 and Figure 61. Similarly as it was obtained for training operating points, here also reasonable agreement is observed between the simulated pressure histories and the experimental counter parts. The simulated pressure and RoHR histories and corresponding to them emissions are considered baseline results for the optimization task presented in the next paragraph.

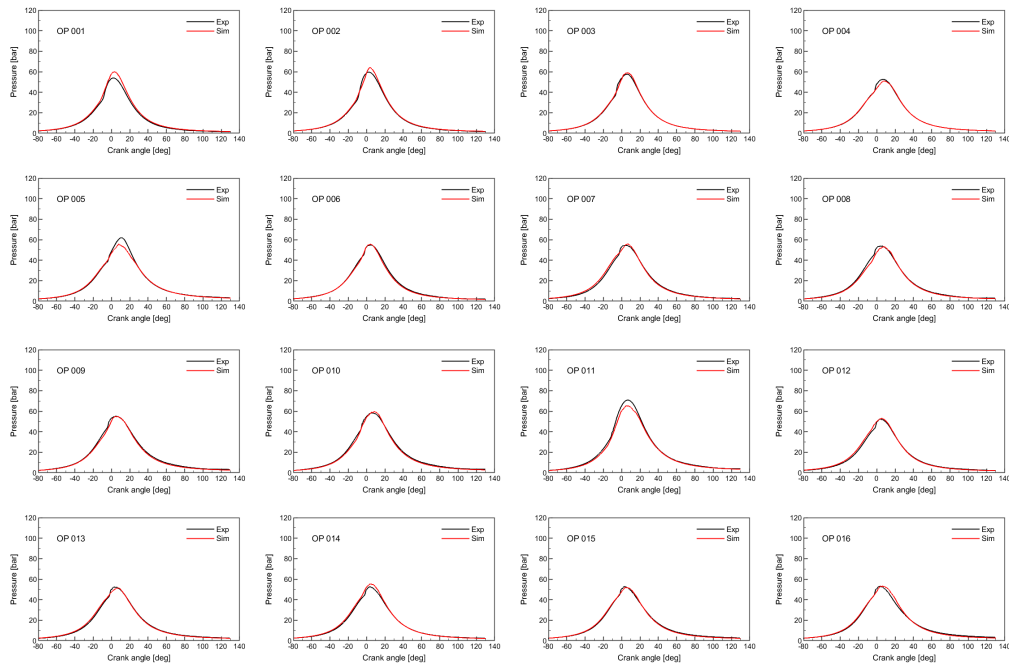


Figure 60: Comparison between the experimental and the simulated in-cylinder pressure histories for operating points listed in Table 17

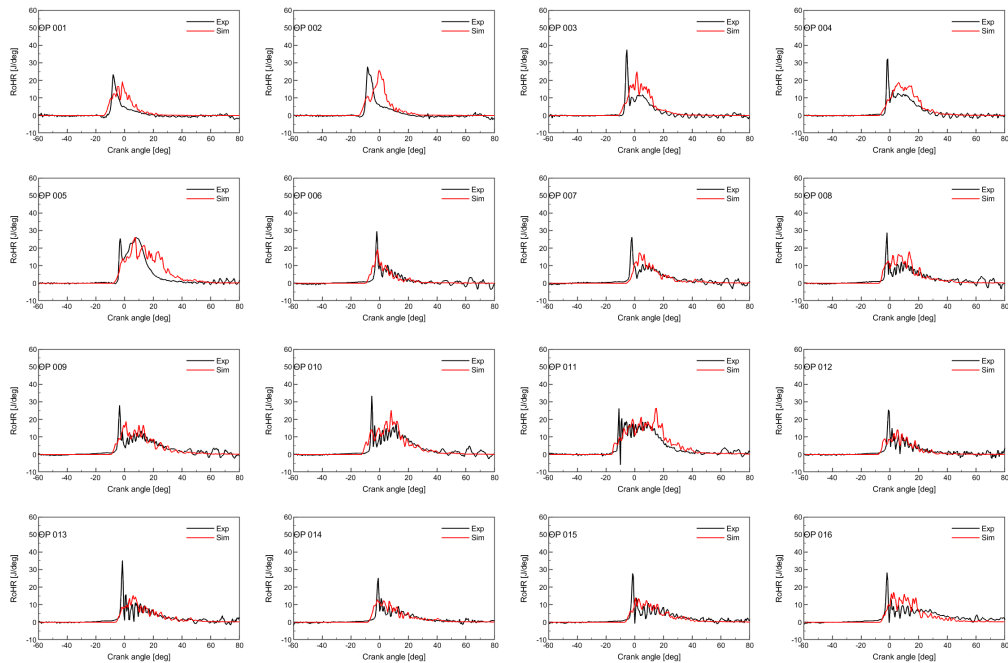


Figure 61: Comparison between the histories of RoHR from experimental pressure and the simulated RoHR for operating points listed in Table 17

Optimized engine performance map

Having verified the SRM in simulating in-cylinder performance parameters over sixteen operating points, the model can be applied to extrapolate engine performance parameters beyond the baseline conditions (see, previous section). Here, to demonstrate this capability, the modelling is applied for evaluating the possibility to reduce engine out CO₂ by changing fuel injection strategy and enabling an increase of ammonia share in the fuel. The optimization was conducted using the engine-fuel co-optimization framework introduced earlier in the report. The optimization strategy is outlined in Table 20.

Table 20: Overview of the optimization strategy.

No.	Name	Type	Range
1	dSOI	variable	$\pm 4[deg]$
2	dFF(NH ₃)	variable	$0 - 0.15[-]$
3	IMEP	constraint	$\pm 5\%$
4	CO ₂	target	reduction

In this table dSOI denotes the range within which the injection rates were varied from the reference value at each operating, dFF(NH₃) denotes the range of increase of fuel fraction (FF) of NH₃ from the reference value at each operating point. IMEP was constrained to $\pm 5\%$ accuracy window from the reference value at each operating point. On the other hand by having IMEP as a constraint being close to the baseline results, it is prevented that the optimizer may search for a solution far from the baseline data. This makes possible to evaluate the plausibility of the obtained results by their comparison to those existing baseline or experimental data. Such a possibility is an advantage at early application phase, and when there are no reference data available that would come from the same inputs as simulated/optimized ones. The results are presented in Figure 62 – Figure 65

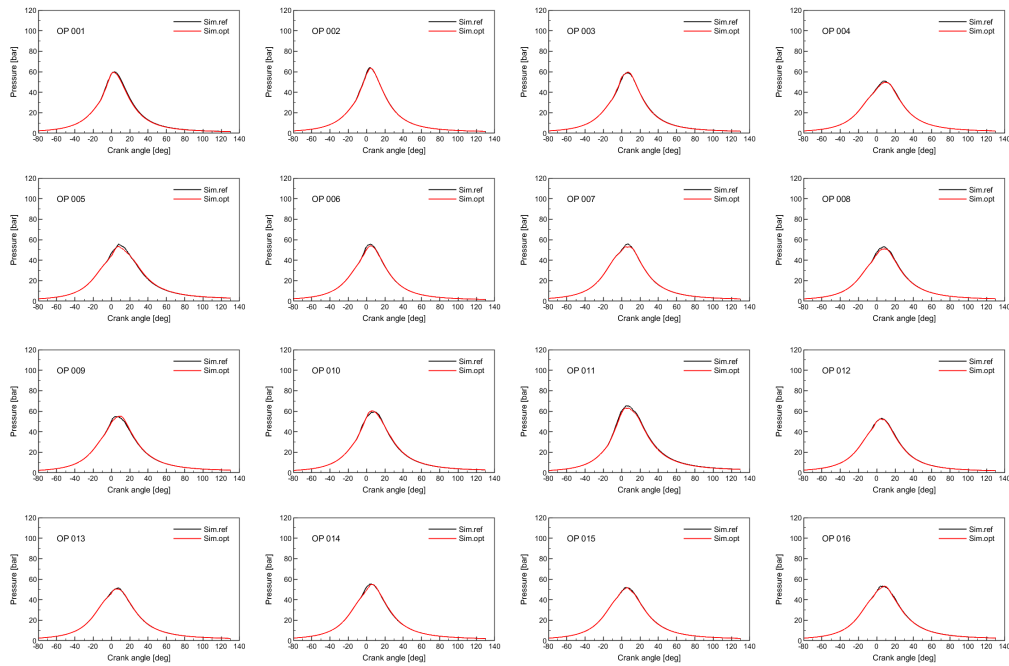


Figure 62: Comparison between the simulated baseline (ref.) and the simulated after optimization (opt.) in-cylinder pressure histories for operating points listed in Table 17

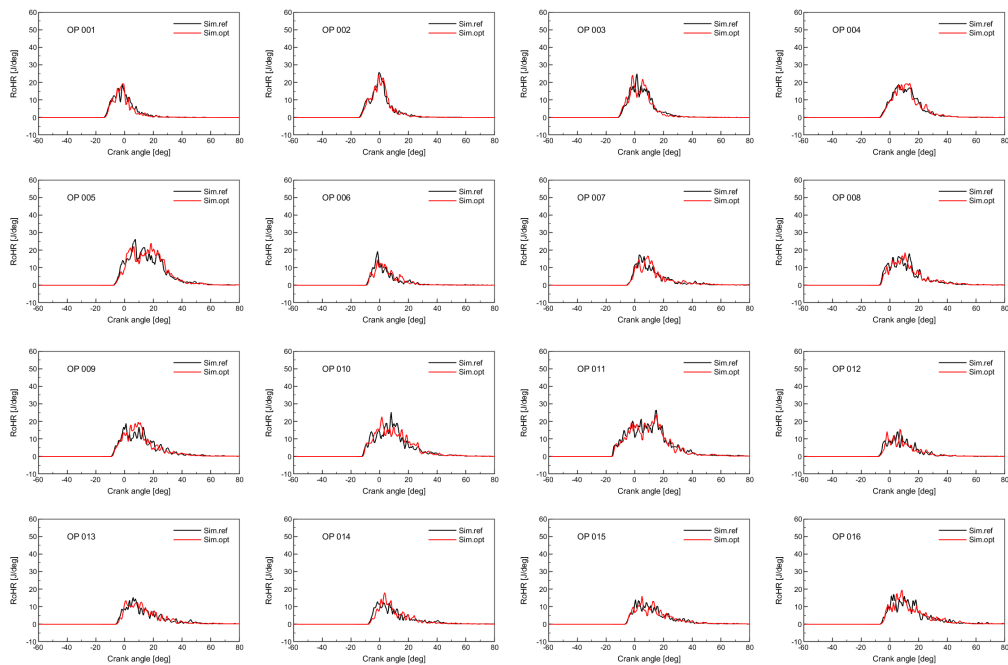


Figure 63: Comparison between the simulated baseline (ref.) and the simulated after optimization (opt.) RoHR histories for operating points listed in Table 17

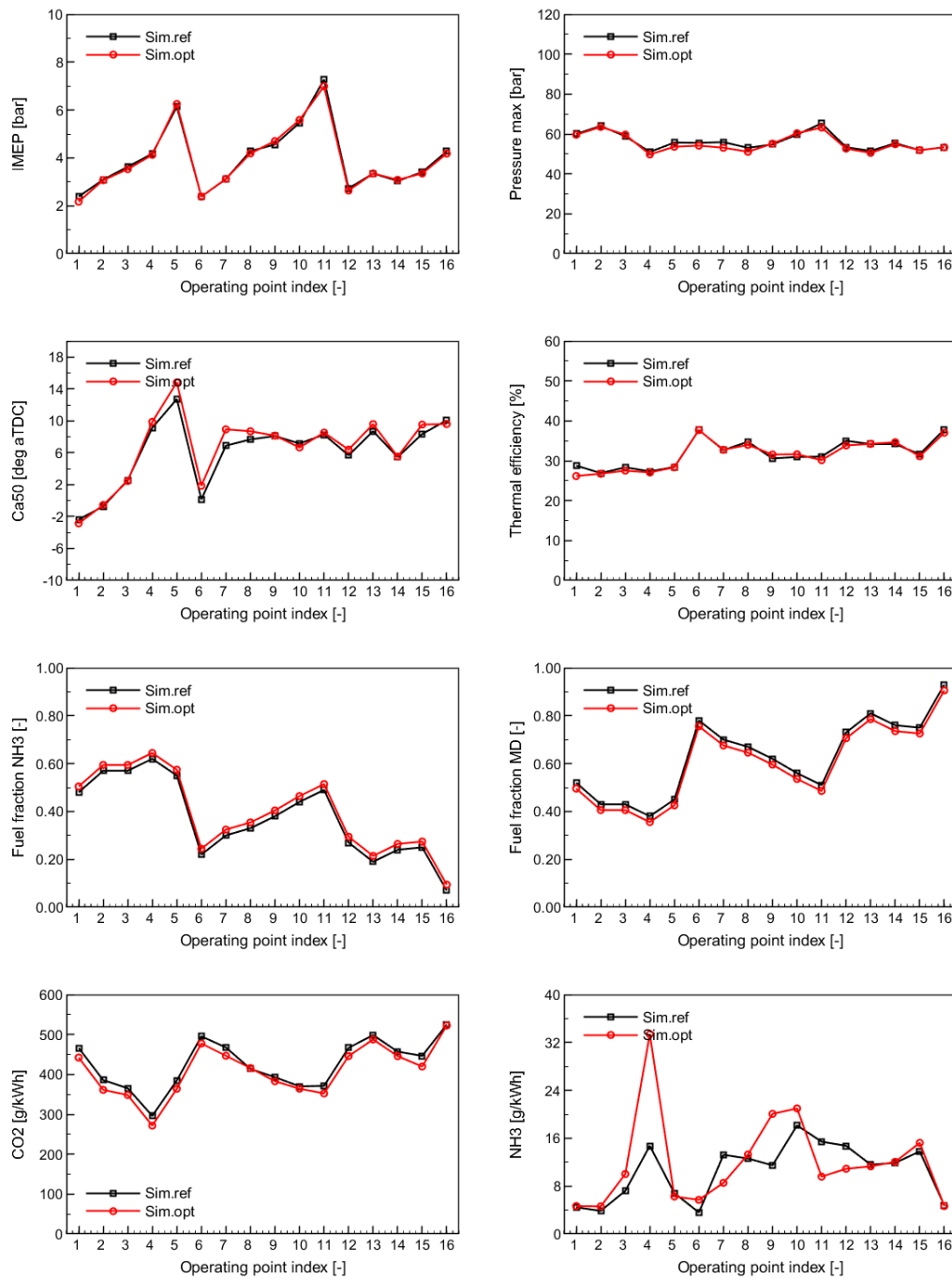


Figure 64: Comparison between the simulated baseline (ref.) and the simulated after optimization (opt.) for selected global engine performance parameters and exhaust emissions for operating points listed in Table 17

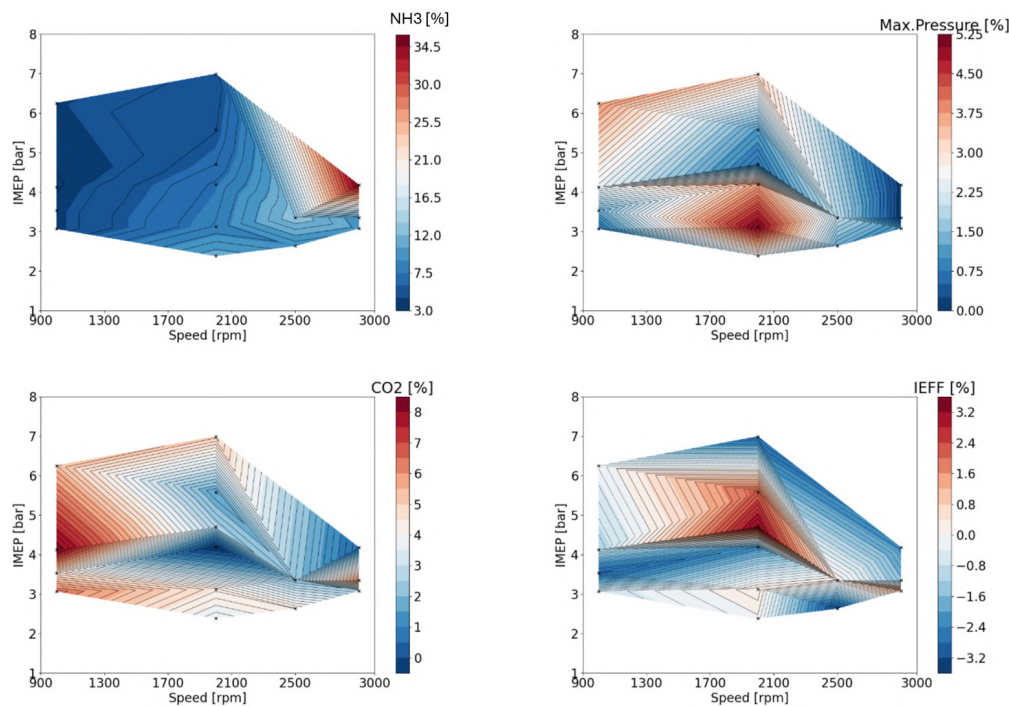


Figure 65: Difference maps (relative error %) between the simulated baseline (ref.) and the simulated after optimization (opt.) for selected global engine performance parameters and exhaust emissions for operating points listed in Table 17

Summary

A methodology has been presented for predicting engine performance parameters over wide range operating points based on a numerical model that was trained for a limited set of experimental data. The methodology is referred to as performance mapping and was applied to the engine with direct injection of ammonia and biodiesel. The methodology is of general purpose. It can be applied to differently formulated optimization tasks in the context of combustion engines and fuels used for their felling. Specifically in this report, the results obtained indicate on potential benefits of changing fuel injection timing and increasing ammonia share in the fuel for CO₂ reduction, and for a given load conditions. By optimizing only the start of fuel injection for both fuels, and without changing the the delay between them, does not help significantly in reducing engine out CO₂ (reduction between 1% – 7%) for a given load conditions. In this specific case the reference data that were available for numerical campaigns came from an engine that was already preliminary optimized on the test bench for the use of ammonia and biodiesel. This partly explains why no significantly better results were obtained. However, when analyzing the experimental results versus the simulated results from the trained/optimized model the later ones show expected trends and hence, the optimized results and the co-simulations methodology are considered plausible. Definitive judgment of the obtained results and the robustness of the co-simulation procedure will only be possible if the optimized results could be compared to the measured ones from an engine that was operated according to the configuration given by numerical findings.

5 Summary

Executive summary

The combination of the 0D SRM of engine in-cylinder processes with detailed reaction kinetics for methyldecanoate as biodiesel surrogate and ammonia along with optimization algorithms provides an effective simulation tool chain for the analysis and predicting of combustion and emissions formation from a compression ignition engine with direct injection of ammonia and biodiesel.

Detailed reaction kinetics modelling was applied to formulate surrogate fuel for NH₃ and biodiesel. As biodiesel methyl-decanoate was used. The new model was updated to match published experiments for ammonia and methyl-decanoate. The surrogate fuel model was developed in the standard form and subsequently converted into the combustion progress variable (CPV) form and by 0D engine simulations employing stochastic reactor model (SRM). SRM-based simulations provided information about maximum AES for a given injection strategy that engine can tolerate without penalty in efficiency and output performance. By employing multi-objective optimization framework, the study was extended to wider range of operating points and resulted in virtual and engine performance maps that indicate on the potential benefits of increasing AES. In turn, 3D CFD was used for space resolved analysis of ammonia injection and provided information about the impact of injector positioning, injection timing and spray angle on mixture formation.

The conducted investigations revealed that the positioning of injectors, spray angle and plume cone are among the most influential parameters governing the combustion process. Early injection of NH₃ (here -60 CAD aTDC) provides relatively homogeneous mixture and premixed combustion is expected. Late NH₃ injection that overlaps with diesel injection is expected to lead to more like non-premixed combustion as NH₃ still evaporates. AES, 54% approximately, seems to be reasonable limit below which engine can be operated without penalty in thermal efficiency and combustion stability. The predicted by the SRM local properties of the mixture such as temperature and equivalence ratio, exhibit similar behavior as these obtained in 3D CFD that further highlights the quality of the 0D SRM we applied to the present work. Combining the 0D SRM and reaction kinetics with the optimization framework, has further improved the predictive character of 0D modelling. It is not only possible to investigate and diagnose the existing engine configurations, but one can extrapolate the results to different operating points and fueling strategies. This feature enables evaluating possible advantages and disadvantages of different engine designs and configurations yet before going into usually time-consuming and costly production of prototypes and experiments.

Results dissemination

- Lewandowski, M. T., Emberson, D., Netzer, C., Løvås, T. and Pasternak, M., Simulations of Direct Injection of Liquid Ammonia Spray in CI Engine. Global CONVERGE User Conference September 27–30, 2021, Online (NTNU, LOGE)
- Pedersen, K. A., Lewandowski, M. T., Pasternak M., Netzer C., Løvås, Numerical investigation of favorable injection strategies in an ammonia-diesel dual-fuel CI engine,

1st Symposium on Ammonia Energy, Cardiff, United Kingdom, 01-02 Sept. 2022, (NTNU, LOGE).

- Lewandowski, M.T., Pasternak, M., Løvås, T., Simulations of ammonia spray evaporation, cooling and mixture formation in a direct injection compression ignition engine; 7th International Conference on Contemporary Problems of Thermal Engineering CPOTE 2022 — Hybrid event, Warsaw, 20-23 September 2022, (NTNU, LOGE).
- Pasternak, M., Lewandowski, M.T., Pedersen, K.A., Siddareddy, R.B., Simulation and optimization of ammonia-based combustion system for a compression ignition engine; 7th International Conference on Contemporary Problems of Thermal Engineering CPOTE 2022 — Hybrid event, Warsaw, 20-23 September 2022, (NTNU, LOGE).
- Pedersen, K.A., Lewandowski, M.T., Pasternak, M. and Løvås, T. Identification of N₂O formation in an ammonia/n-heptane dual-fuelled compression ignition engine using numerical simulations, Proceedings of the European Combustion Meeting, Rouen, April 26 and 28, 2023, (NTNU, LOGE).
- Lewandowski M.T., Pasternak, M., Haugsværa, M., Løvås, T., Simulations of ammonia spray evaporation, cooling, mixture formation and combustion in a direct injection compression ignition engine, International Journal of Hydrogen Energy, <https://doi.org/10.1016/j.ijhydene.2023.06.143>, (NTNU, LOGE).
- Pasternak, M., Przybyła G., Adamczyk W., Siddareddy R. and Mauss, F., Numerical study of combustion in a compression ignition engine with direct ammonia and biodiesel injection for agriculture applications, 2nd Symposium on Ammonia Energy, Orlean, France 11-13 July 2023, (NTNU, LOGE, SUT).
- Pedersen, K.A., Lewandowski, M.T., Schulze-Netzer, C., Pasternak, M. and Løvås, T., Ammonia in Dual-Fueled Internal Combustion Engines: Impact on NO_x, N₂O, and Soot Formation. Energy Fuels 2023, 37, 22, 17585–17604, <https://doi.org/10.1021/acs.energyfuels.3c02549>, (NTNU, LOGE).
- ACTIVATE Seminar 2021: Ammonia as carbon free fuel for internal combustion engine driven agricultural vehicle, 1 Dec. 2021, online (NTNU, LOGE, SUT).
- ACTIVATE Seminar 2022: Ammonia as carbon free fuel for internal combustion engine driven agricultural vehicle, 28 April 2022, online (NTNU, LOGE, SUT), 22 Sep. 2022.

References

- [1] Richards K. J., Senecal P. K., and Pomraning E. *CONVERGE 3.0, Convergent Science*. Madison, WI., 2020.
- [2] Loge AB. LOGEsoft. <http://www.loge.se>, 2020.
- [3] Matrisciano A., Pasternak M., Wang X., Antoshkiv O. Mauss F., and Berg P. On the performance of biodiesel blends-experimental data and simulations using a stochastic fuel test bench. *SAE Technical Paper*, 2014-01-1115, 2014.
- [4] Franken T., Sommerhoff A., Willvems W., Matrisciano A. Lehtiniemi H., Borg A., Netzer C., and Mauss F. Advanced predictive diesel combustion simulation using turbulence model and stochastic reactor model. *SAE Technical Paper*, 2017-01-0516, 2017.
- [5] Pasternak M., Mauss F., Perlman C., and Lehtiniemi H. Aspects of 0D and 3D Modeling of Soot Formation for Diesel Engines. *Combust. Sci. and Tech.*, pages 1517–1535, 2014.
- [6] Tunér M., Pasternak M., Mauss F., and H. Bensler. A PDF-Based Model for Full Cycle Simulations of Direct Injected Engines. *SAE Paper 2008-01-1606*, 2008.
- [7] Nett O., Pasternak M., Yang Q., Mauss F., Bargende M., Franken T., Grill M., and M. Diezemann. Modelling emissions of diesel engine combustion with variable valve timing. In *Proc. FVV Autumn Conference (21-25 September 2020)*, 2020.
- [8] Matrisciano A., Franken T., Perlman C., Borg A., and Mauss F. Development of a computationally efficient progress variable approach for a direct injection stochastic reactor model. *SAE Paper 2017-01-0512*, 2017.
- [9] Nett O., Pasternak M., Yang Q., Mauss F., Bargende M., Franken T., Grill M., and M. Diezemann. Modelling emissions of diesel engine combustion with variable valve timing. In *In: Spannungsfeld Fahrzeugantriebe – Gedenkschrift für Prof. Dr.-Ing. Roland Baar*, 2020.
- [10] L. Seidel. *Development and reduction of a multicomponent reference fuel for gasoline*. PhD thesis, Brandenburg University of Technology, 2019.
- [11] Krishna P Shrestha, Lars Seidel, Thomas Zeuch, and Fabian Mauss. Detailed Kinetic Mechanism for the Oxidation of Ammonia Including the Formation and Reduction of Nitrogen Oxides. *Energ. Fuels.*, 32(10):10202–10217, 2018.
- [12] Mauß F. *Entwicklung eines kinetischen Modells der Rußbildung mit schneller Polymerisation*. PhD thesis, RWTH Aachen, 1998.
- [13] Lewandowski M.T., Netzer C., Emberson D.R., and Løvås T. Numerical investigation of optimal flow conditions in an optically accessed compression ignition engine. *Transportation Engineering*, 2:100036, 2020.

- [14] Liu Z., Wijeyakulasuriya S., Mashayekh A., and Chai X. Investigation of reynolds stress model for complex flow using CONVERGE. *SAE Technical Paper*, 2020-01-1104, 2020.
- [15] Netzer C. Seidel L., Ravet F., and Mauss F. Impact of the surrogate formulation on 3D CFD engine knock prediction using detailed chemistry. *Fuel*, 254:115678, 2019.
- [16] Liu X., Wang H., and Yao M.. Investigation of the chemical kinetics process of diesel combustion in a compression ignition engine using the large eddy simulation approach. *Fuel*, 270:117544, 2020.
- [17] Duvvuria P.P., Sukumaranb S., Shrivastavac R.K., and Sreedharad S. Modeling soot particle size distribution in diesel engines. *Fuel*, 243:70–78, 2019.
- [18] Duvvuria P.P., Shrivastavac R.K., and Sreedharad S. Numerical optimization of a diesel combustion system to reduce soot mass and particle number density. *Fuel*, 266:117015, 2020.
- [19] Boldajia M.R., Gaineya B., O'Donnella P., Gohnb J., and Lawler B. Investigating the effect of spray included angle on thermally stratified compression ignition with wet ethanol using computational fluid dynamics. *Applied Thermal Engineering*, 170:114964, 2020.
- [20] Senecal P.K., Richards K.J., Pomraning E., Yang T., Dai M.Z., McDavid R.M., Patterson M.A., Hou S., and Shethaji T. A new parallel cut-cell cartesian CFD code for rapid grid generation applied to in-cylinder diesel engine simulations. *SAE Technical Paper*, 2007-01-0159, 2007.
- [21] Kim D., Martz J., and Violi A. Effects of fuel physical properties on direct injection spray and ignition behavior. *Fuel*, 180:481–496, 2016.
- [22] F Duronio, De Vita A., Allocca L., Montanaro A., Ranieri S., and Villante C. CFD numerical reconstruction of the flash boiling gasoline spray morphology. *SAE Technical Paper*, pages 2020–24–0010, 2020.
- [23] Schmidt D.P. and Rutland C.J. A new droplet collision algorithm. *Journal of Computational Physics*, 164:62–80, 2000.
- [24] Amsden A.A., O'Rourke P.J., and Butler T.D. KIVA-II: A computer program for chemically reactive flows with sprays. *Los Alamos National Laboratory Technical Report*, LA-11560-MS, 1989.
- [25] Senecal P. K. Pomraning E., Richards K.J., and Som S. Grid convergent spray models for internal combustion engines cfd simulations. In *Proceedings of the ASME 2012 Internal Combustion Engine Division Fall Technical Conference*, Vancouver, Canada, September 23-26 2012.
- [26] Xu M., Zhang Y., Zeng W., Zhang G., and Zhang M. Flash boiling: Easy and better way to generate ideal sprays than the high injection pressure. *SAE Int. J. Fuels Lub*, 6:2013–01–1614, 2013.

- [27] Xu L., Chang Y., Treacy M. and Zhou Y., and Jia M. and Bai X-S. A skeletal chemical kinetic mechanism for ammonia/n-heptane combustion. *Fuel*, 331:125830, 2023.
- [28] Xiaoxiao Wang. *Kinetic mechanism of surrogates for biodiesel*. doctoral thesis, BTU Cottbus - Senftenberg, 2018.
- [29] Krishna Prasad Shrestha, Lars Seidel, Thomas Zeuch, and Fabian Mauss. Kinetic Modeling of NO_x Formation and Consumption during Methanol and Ethanol Oxidation. *Combustion Science and Technology*, 191(9):1628–1660, sep 2019.
- [30] Krishna Prasad Shrestha, Nicolas Vin, Olivier Herbinet, Lars Seidel, Frédérique Battin-Leclerc, Thomas Zeuch, and Fabian Mauss. Insights into nitromethane combustion from detailed kinetic modeling – Pyrolysis experiments in jet-stirred and flow reactors. *Fuel*, 261:116349, feb 2020.
- [31] B. Shu, S.K. Vallabhuni, X. He, G. Issayev, K. Moshhammer, A. Farooq, and R.X. Fernandes. A shock tube and modeling study on the autoignition properties of ammonia at intermediate temperatures. *Proceedings of the Combustion Institute*, 37(1):205–211, 2019.
- [32] O. Mathieu, J. Goulier, F. Gournel, M. S. Mannan, N. Chaumeix, and E. L. Petersen. Experimental study of the effect of CF₃I addition on the ignition delay time and laminar flame speed of methane, ethylene, and propane. *Proc. Combust. Inst.*, 35(3):2731–2739, 2015.
- [33] Zhen Huang Zhenhua Li, Weijing Wang and Matthew A. Oehlschlaeger. The autoignition of methyl decanoate, a biodiesel surrogate, under high-pressure exhaust gas recirculation conditions. *Energy Fuels*, 26:4887–4895, 06 2013.
- [34] Weijung Wang and Matthew A. Oehlschlaeger. A shock tube study of methyl decanoate autoignition at elevated pressures. *Combustion and Flame*, 159:476–481, 2012.
- [35] Weijing Wang, Sandeep Gowdagiri, and Matthew A. Oehlschlaeger. Comparative study of the autoignition of methyl decanoates, unsaturated biodiesel fuel surrogates. *Energy and Fuels*, 27:5527–5532, 2013.
- [36] Pierre Alexandre Glaude, Olivier Herbinet, Sarah Bax, Joffrey Biet, Valérie Warth, and Frédérique Battin-Leclerc. Modeling of the oxidation of methyl esters—validation for methyl hexanoate, methyl heptanoate, and methyl decanoate in a jet-stirred reactor. *Combustion and Flame*, 157:2035–2050, 2010.
- [37] Xiaoyuan Zhang, Shamjad P. Moosakutty, Rajitha P. Rajan, Mourad Younes, and S. Mani Sarathy. Combustion chemistry of ammonia/hydrogen mixtures: Jet-stirred reactor measurements and comprehensive kinetic modeling. *Combustion and Flame*, 234:111653, 2021.
- [38] Gaucherand J. Determination of internal geometry of a gasoline direct injector with the use of silicone methodology. *Internal NTNU report*, pages 1–4, 2021.

- [39] *ECN Engine Combustion Network*, 2021.
- [40] Pelé R., Mounaïm-Rousselle Ch., Bréquigny P., Hespel C., and Bellettre J. First study on ammonia spray characteristics with a current GDI engine injector. *Fuels*, 2:253–271, 2021.
- [41] Mojtabi M., Chadwick, Wigley G., and Helie J. The effect of flash boiling on break up and atomization in GDI sprays. In *22nd European Conference on Liquid Atomization and Spray Systems- ILASS 2008*, Como Lake, Italy, Sep. 8-10, 2008.
- [42] Price C., Hamzehloo A., Aleiferis P., and Richardson D. Aspects of numerical modelling of flash-boiling fuel sprays. *SAE Technical Paper*, pages 2015–24–2463, 2015.
- [43] Okafor E.D., Yamashita H., Hayakawa A., Kunkuma K.D., Somarathne A., Kudo T., Tsujimura T., Uchida M., Ito S., and Kobayashi H. Flame stability and emissions characteristics of liquid ammonia spray co-fired with methane in a single stage swirl combustor. *Fuel*, 287:119433, 2021.
- [44] Faeth G.M. Current status of droplet and liquid combustion. *Progress in Energy and Combustion Sciences*, 3:191–224, 1977.
- [45] Chiang C.H., Raju M.S., and Sirignano W.A. Numerical analysis of convecting, vaporizing fuel droplet with variable properties. *International Journal of Heat and Mass Transfer*, 35:1307–1324, 1992.
- [46] Reiter A.J. and Kong S-C. Combustion and emissions characteristics of compression-ignition engine using dual ammonia-diesel fuel. *Fuel*, 90:87–97, 2011.
- [47] Lesmana H., Zhang Z., Li X., Zhu M., Xu W., and Zhang D. NH_3 as a transport fuel in internal combustion engines: A technical review. *Journal of Energy Resources Technology*, 141:JERT–18–1595, 2019.
- [48] He X., Shu B., Nascimento D., Moshhammer K., Costa M., and Fernandes R.X. Auto-ignition kinetics of ammonia and ammonia/hydrogen mixtures at intermediate temperatures and high pressures. *Combustion and Flame*, 206:189–200, 2019.

Definitions/Abbreviations

AES - Ammonia energy share
PM - Particulate matter
PSD - Particle size distribution
CFD - Computational fluid dynamics
SRM - Stochastic reactor model
PDF - Probability density function
IEM - Exchange with the mean
EMST -Euclidean Minimum Spanning Tree
CN - Cetane number
LHV - Lower heating value
EGR - Exhaust gas recirculation
TDC - Top dead center
ATDC - After top dead center
CAD - Crank angle degree
SOI - Start of injection
EVO - Exhaust valve opening